THESIS FOR THE DEGREE OF LICENTIATE OF ENGINEERING

Nanofluidic Scattering Microscopy for Single Particle Catalysis

BJÖRN ALTENBURGER

CHALMERS
UNIVERSITY OF TECHNOLOGY

Department of Physics

CHALMERS UNIVERSITY OF TECHNOLOGY

Gothenburg, Sweden 2022

Nanofluidic Scattering Microscopy for Single Particle Catalysis

BJÖRN ALTENBURGER

Department of Physics
Chalmers University of Technology
SE-412 96 Gothenburg
Sweden
Telephone + 46 (0)31-772 1000

Cover:
Artistic rendering of a nanochannel containing a trapped colloidal nanoparticle in front of a constriction. A catalytic reaction causes the formation of smaller bubbles that combine into a large bubble that fills the channel opposite the particle.

Printed at Chalmers Reproservice

Gothenburg, Sweden 2022

Nanofluidic Scattering Microscopy for Single Particle Catalysis

Björn Altenburger
Department of Physics
Chalmers University of Technology

Abstract

Heterogeneous catalysis concerns material formulations – catalysts – that can assist a chemical reaction by improving its rate or selectivity, by lowering activation barriers and altering the energy landscape. The core of catalysts are often tiny metal particles that provide a large reaction surface at a small volume, as well as low coordination sites whose type and abundance depends on particle size and shape. Hence, such nanoparticles come in a broad spectrum of sizes and shapes when studied in a so-called ensemble comprised of millions of particles. Ensemble experimental techniques therefore often disregard the structural heterogeneity of nanoparticles as the measurements of such samples provide information on the averaged response of the heterogeneous ensemble. Consequently, "superparticles" with exceptional performance may be overlooked, or erroneous structure-function correlations may be established.

To overcome the ensemble averaging problem, various techniques for single particle catalysis have been developed. The approaches include methods like fluorescence microscopy, X-ray diffraction and scattering, electron microscopy and plasmonic sensing. These methods have in common that they detect electrons or photons that report either on the reactant molecules consumed, the product molecules formed, changes to the catalyst particle itself, or temperature changes that the reaction evokes in the particle surrounding. However, none of the experimental methods provide direct single particle activity information without either using plasmonic enhancement effects that may also impact the studied reaction itself and limit the range of catalyst materials that can be studied or using fluorescence that limits reaction conditions to ultralow concentrations and to a narrow range of reactions.

The overarching goal of the work presented in this thesis has been to develop an optical microscopy technique that can quantitatively measure catalytic activity, and in the longer term even selectivity, of a single nanoparticle without the limitations of existing single particle methods. At the core of this method that we call Nanofluidic Scattering Microscopy are nanofluidic channels that can accurately control the transport of reagents to and from a single catalytically active particle localized inside the channels. As a second key trait, the unique light scattering properties of nanochannels render them highly sensitive to refractive index changes of the fluid inside them. Hence, when a catalytic reaction alters the molecular composition of the fluid in the channel, its light scattering characteristics change and reveal in this way the catalytic performance of the nanoparticle.

In this thesis, I describe my winding journey towards the first successful implementation of Nanofluidic Scattering Microscopy, where I characterize the catalytic activity in terms of turnover frequency of single colloidal Pt nanoparticles trapped inside nanofluidic channels during the H_2O_2 decomposition reaction. The experiments reveal that ligands covering the particle surface distinctly impact the activity.

List of appended papers

This thesis is the basis for the work presented in the following papers:

Paper I

Nanofluidic Scattering Microscopy of Single Colloidal Platinum Nanoparticle H_2O_2 Decomposition Catalysis

Björn Altenburger, Carl Andersson, Sune Levin, Fredrik Westerlund, Joachim Fritzsche, and Christoph Langhammer

In Manuscript

Table of contents

1 Introduction

The challenge I have targeted in this thesis is to study catalytic reactions on nanoparticles in realistic conditions without the use of fluorescence or nanoplasmonic techniques. Is this an important task? In heterogeneous catalysis, the best catalyst for a specific chemical reaction is found when the highest reactivity or most advantageous selectivity is obtained with the least amount of catalyst used. To this end, since heterogeneous catalytic reactions take place on the surface of a catalyst in the solid state, the ratio of surface versus volume of that catalyst is maximized when using small nanoparticles in the sub-10 nm size range that extends all the way down to so-called clusters comprised of tens of atoms or even single atoms, as the most extreme case. However, it is not only size but also particle shape that matters, since certain reactions, for example, prefer corner or edge sites on the particles[1], while some prefer certain crystalline planes[2] and for some reactions, it is the very specific interplay between different types of sites[3] that is key. However, when nanoparticles are produced, they usually exhibit a significant variety in terms of their shape and size, as well as composition if alloys are considered. Hence, if one would like to experimentally correlate catalyst reactivity with particle size, shape and composition, to not average out potentially relevant structural effects, it is beneficial to investigate catalyst nanoparticles individually. This, however, is a significant experimental challenge due to their tiny size and due to the tiny amount of product molecules produced on their surface.

The challenge to study catalytic reactions over single particles has inspired many scientists over the years and the various experimental approaches are a result of a long tradition in heterogeneous catalysis where one tries to reveal the details of a surface reaction while the catalyst is working in real reaction conditions[4–9]. The term “in situ” is used in this context to describe methods that can characterize catalysts in controlled environments, although such conditions may not represent the environments the catalyst will experience under operation conditions. The term “operando” goes one step further and is used for approaches that monitor the catalyst while it is converting reactants. As the relevant length scales in catalysis are in the micro and nanometer regime, the experimental techniques used to study catalysts have also entered this realm. The entry point to this nanoscopic environment is for many approaches synchrotron radiation as the short wavelength can resolve very small structures[10] (10 nm to 5 nm) while the generated photons can penetrate the reactor atmosphere and the catalyst. Examples of widely used synchrotron-based techniques are scanning-transmission X-ray microscopy (STXM) and quick scan X-ray absorption fine structure (QXAFS)[11,12]. Being based on highly transmissive X-rays, using these methods the inner structure of catalysts can be revealed with nanometer spatial resolution tiny pores and the metal nanoparticle distribution inside can be resolved[12]. The drawback with synchrotron methods is the extensive infrastructure that is needed to generate the radiation and that they reveal only the structure of the catalyst but often not their activity at the same time. Another noteworthy example of an experimental method for single particle catalysis is using the fluorescence emission of (single) molecules[13] to reveal chemical reactions on the surface of single nanoparticles, sometimes even

with sub-particle spatial resolution[6,14–16]. This approach is relatively new to chemistry but has been used in biology for decades[13] to study the processes within cells and organelles and earned Stefan Hell the Nobel prize in 2014. While the experimental setup required is relatively simple compared to a synchrotron experiment, the main limiting factors for (super resolution) fluorescence microscopy in single particle catalysis are that one is limited to a very small number specific reactions that either form a fluorescent product or during which fluorescence is extinct. Furthermore, one has to work at a from a practical perspective unrealistically low reactant concentration to ensure single molecular resolution in the super resolution version of fluorescence microscopy.

Another family of single particle catalysis experimental techniques focuses on the nanoparticles themselves. To this end, when talking about nanoparticles in heterogeneous catalysis, they are usually only regarded as the catalytically active part and therefore the entities of interest to be investigated. However, it turns out that they also - at the same time - can play the part of the observer of a catalytic process that takes place on their surface[17]. This is enabled by an optical phenomenon called localized surface plasmon resonance (LSPR)[17–19], a coherent collective oscillation of the electrons of the particle that has its resonance frequency in the UV-vis-NIR spectral range, depending on the size, shape and composition of the particle, as well as the particles' intimate surroundings. As the resonance frequency of the LSPR therefore is sensitive to, for example, the oxidation state of a metal nanoparticle, it can be used to monitor the surface state of single catalyst nanoparticles in situ[18,20–22] by tracking shifts in resonance frequency with high precision[23] at the level of single nanoparticles using dark-field scattering microscopy[17,24]. However, this plasmonic nanospectroscopy and imaging concept falls short on being able to also provide information about the activity of the catalyst particle. In an attempt to alleviate this problem, earlier work in our group has combined LSPR with quadrupole mass spectrometry from particles localized in tiny nanofluidic reactors[18,20,21]. However, the QMS readout is limited to a few hundred nanoparticles since it does not provide the sensitivity to address individual ones, thereby still leaving the "holy grail" of an activity measurement from a single nanoparticle in operando at technically relevant conditions an unreached dream.

The plasmon oscillation of metal nanoparticles can also be used to enhance the Raman absorption of molecules in their close vicinity, as it is done in, so-called, plasmon or tip enhanced Raman spectroscopy (PERS and TERS, respectively)[25,26] that has been used to investigate the photocatalytic processes of nitrothiophenol on gold surfaces[27]. One of the main drawbacks and limitations of PERS and TERS is that the enhancing plasmonic particle or tip also must serve as the catalyst, which limits the catalyst materials available severely since essentially only Ag and Au would provide a strong enough Raman-enhancing effect. To overcome this limitation, a solution was developed where the Raman-enhancing (Au) nanoparticle is isolated by a passive shell, in analogy to indirect nanoplasmonic sensing[22,28], in what has come to be known as Shell-Isolated Nanoparticle-Enhanced Raman Spectroscopy (SHINERS)[11]. This method has for example been successfully used for the investigation of the oxygen reduction reaction on high-index Pt where evidence of OH and OOH intermediates was found[29]. Despite this significant advance SHINERS has provided to Raman-based single particle catalysis, it is still limited by the fact that a passive and bulky (compared to the catalyst particles) observer nanoparticle must be used, which may quite significantly impact the catalyst formulation and thus potentially the catalytic properties. Furthermore, SHINERS-type

"antenna-reactor complexes", where a plasmonic antenna is placed close to catalyst nanoparticles, are widely explored in plasmon-mediated catalysis to enhance and steer catalytic reactions by light[30–33]. This highlights a further risk of plasmon enhanced Raman spectroscopy methods, that is, that the plasmonic effect used to probe the catalytic reaction at the same time also might (dramatically) impact it and therefore lead to wrong conclusions.

Another class of experimental methods widely used to investigate catalysis at the single nanoparticle level are electron microscopy approaches[7,10,34,35]. These methods focus on elucidating the (dynamics of) catalyst particle structure and (oxidation) state and offer atomic resolution under certain conditions. At the early stages, scanning electron microscopy (SEM) and transmission electron microscopy (TEM) was used to study catalyst ex-situ, that is, before and after reaction. The development of differentially pumped microscopes, sample cells and specialized holders have enabled the operando investigation of single particles at high pressures[36–38] and even in the liquid phase[39,40]. They have, for example, revealed the oscillating behavior of Pt[41] or Pd[42] nanoparticles during reaction and monitored the dynamics of single atoms[43]. However, as the key limitations, electron microscopy methods can only investigate one particle at a time, and they do not provide information about (single particle) catalyst activity or selectivity.

This plethora of single particle catalysis characterization techniques that has been developed to date is evidence enough that we are dealing with both an interesting and highly relevant topic in heterogeneous catalysis that has sparked the interest of many research groups.

I present in this thesis my approach to address the above outlined challenges in single particle catalysis towards realizing its ultimate goal. The concept that I introduce in my work is on one hand based on the fact that the refractive index (RI) of any fluid will change if its molecular composition is changed[44], for example by a chemical reaction between constituents of the fluid. On the other hand, the concept is based on nanofluidic systems and our expertise to use them to both manipulate and control fluids and single nanoparticles at the nanoscale in the context of single particle catalysis[20,21,45–48]. Finally, it builds on our recent discovery of the unique optical properties of nanofluidic systems that enabled the label-free size and mass determination of single biomolecules using what we call Nanofluidic Scattering Microscopy[47] (NSM).

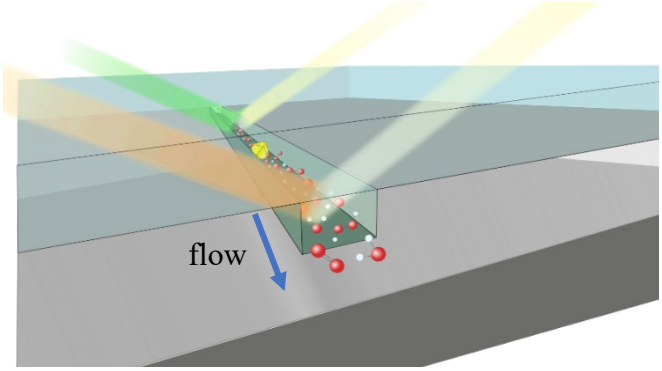

***Figure 1**. Artist's rendition of nanofluidic scattering microscopy for the monitoring of catalytic activity of a single nanoparticle localized inside a nanofluidic channel. Due to a reaction-induced refractive index difference in the liquid in the channel up- and downstream of the catalyst particle, the light scattering intensity from the channel is different in these regions and thereby enables measurements of conversion and thus particle activity.*

To this end, the method that I have developed uses the NSM principle not to detect single molecules but to track the changes in the fluid that is residing in the channel that are induced by a catalytic reaction over a surface of a single nanoparticle localized inside the channel (**Figure 1**).

Some of the key features of NSM that I will discuss in detail in the subsequent chapters are that the used nanochannels´ geometrical cross section is smaller than any wavelength of the visible light spectral range and that these channels nevertheless scatter visible light very efficiently in the Mie-regime. The scattering is owing to the RI contrast between the solid material that hosts the channels and their interior which is either a gas or a liquid. As the second key feature, I will make use of the fact that the scattering intensity of a nanochannel is strongly modulated by the RI difference between channel walls and channel interior. As the hypothesis I set out to explore is that if reactants are flushed into a nanochannel and react on a catalytically active particle localized inside the channel, the molecular structure of a sizable fraction of the molecules in the channel will be changed due to the reaction. Hence, since this molecular structure change alters the molecular polarizability and thus the RI of the liquid in the channel, the catalytic reaction is expected to induce a measurable change of the nanochannels' light scattering both in intensity and spectrum. Therefore, this will make it possible to monitor the catalytic reaction and determine its rate.

Since the NSM approach, in principle, is compatible with a wide range of reactant types and concentrations, as well as reaction pressures, it promises to enable single particle catalysis studies in technically relevant reaction conditions in operando. Furthermore, there are no boundary conditions on the reaction itself, that is, it neither needs to be fluorescent nor have a "color" and there are no plasmonic enhancement effects necessary which should dramatically lower potential artefacts induced by the used probes and enable experiments with an almost unlimited number of catalytic reactions and catalyst materials.

A second aspect is that the benefit of the nanochannels is not limited to their optical properties that enable light scattering based optical microscopy. In fact, they also provide us with unprecedented control of the reaction parameters. For one, we can isolate single particles in their respective nanochannel, such that we avoid any crosstalk between particles, e.g., via reactant concentration gradients or spill-over effects. Secondly, having arrangements of many parallel nanochannels on a chip and in the field of view of the microscope allows to study many single nanoparticles at the same time, while they all are isolated in their own nanochannel. Thirdly, the fluidic system allows us to also accurately control the flow of reactants and with that the mass transport to and from single nanoparticles. In this way, the nanochannels also function as "model pores" that mimic widely used meso- and nanoporous catalyst support materials. Finally, due to the tiny dimensions of the nanochannels, they efficiently prevent extensive dilution of (the small number of) product molecules formed on single catalyst nanoparticles and therefore see to maximizing the RI contrast induced by the reaction. This, in turn, maximizes the chance that the conversion over a single nanoparticle can be experimentally measured.

This thesis is structured in the following way: I will start by introducing the underlying physical principle of NSM for single particle catalysis applications in the beginning of the second chapter and explain the different options we have from a fundamental governing physical perspective. These theoretical predictions will subsequently be corroborated with experimental

data from first measurements in the following section, also explaining our motivation to further develop this technique. The section thereafter is then dedicated to the various ideas I have implemented and explored to both deeper understand and improve the performance of our experimental setup, including advanced nanofluidic chip designs, modifications of the darkfield microscope itself and automated data acquisition and evaluation.

The last section of the second chapter is dedicated to a summary and discussion of the challenges I have encountered during the development of NSM for single particle catalysis. I feel that it is important to discuss in detail those (sometimes still unresolved) challenges in this thesis because it is tackling and trying to resolve them that has led us to the stage we are today, and it is also what forms the basis for our understanding of what needs further improvement and what probably the ultimate limits of our technique are.

Chapter 3 therefore starts out with an analysis of what has been achieved so far and the corresponding key insights gained. On this basis, I subsequently introduce a new nanofluidic chip design and motivate the step from using nanofabricated catalyst particles to instead using colloidal nanocrystals synthesized in solution and trapped inside a nanofluidic channel at a predefined position for my experiments. The insight gained in the previous chapters is here combined with new results such that a foundation of basic understanding is established. The key point here is the emergence of gas bubbles in the nanochannels that have their origin in the catalytic reaction on the surface of a single particle. On the basis of measuring the growth rate of these bubbles in the nanochannels, I will lay out how I finally arrived at a position in the development of this technique that justified the writing of a first publication on this topic.

2 Nanofluidic Scattering Microscopy

2.1 The original idea

Scattering of electromagnetic waves from small objects is an extensive field in physics. It is often separated into the different theories that describe scattering according to the size of the scattering object. At the level of the smallest objects, it is Rayleigh-theory that is used to describe the interaction of light with atoms and molecules, both being much smaller than the wavelength of the incident light. Since this type of scattering shows a distinctive dependency on the wavelength, it leads to common phenomena, such as the blue sky and colorful red and orange sunrises. Interestingly, we also find another type of scattering occurring in the sky above us, since clouds have a distinctive white-grey color. In contrast to the rest of the atmosphere, clouds are comprised of water droplets or ice crystals with sizes comparable to the wavelengths of sunlight. In this case, it is therefore Mie-scattering that describes best the scattering of electromagnetic waves from the water particles that form clouds. Mie-theory indeed predicts a nearly equal scattering intensity for all wavelengths, which thus explains the white-grey color of clouds, as well as of milk and smoke.

In my work, I use nanofluidic channels to study catalysis on single nanoparticles since they (i) offer a unique means to isolate single nanoparticles to avoid crosstalk between them, (ii) enable nanoscale control of reactant transport to and reaction product from single nanoparticles and (iii) prevent the excessive dilution of reaction product. As an important additional point here, I note that these channels have geometrical cross sections on the same order of magnitude as the wavelengths of visible light (light is visible for the human eye between 310 nm and 1100 nm[49]) since the typical width of nanochannels I have worked with is between 100 nm and 200. Hence, they interact strongly with visible light and this interaction is the basis for the NSM concept I have used to study catalytic reactions on single nanoparticles inside nanochannels. To fundamentally understand the light scattering properties of these nanochannels, I present below a short derivation of the most important formulas based on Mie-theory that are required for this purpose. The derivation is based on the assumption that the fluid that fills the nanochannels can be described by a bulk material whose optical properties are defined by its complex dielectric function.

2.1.1 Basics of Mie-Scattering

In this section, I will describe a single nanochannel as a scattering entity when visible light is incident on it. To describe the nanochannels with rectangular cross section used in my experiments in the Mie-framework we can approximate them as infinitely long cylinders. By doing so, we can then follow the derivation of equations that describe the scattering of light from such an object provided by Bohren and Huffman[50].

At the very start, there is the description of the incoming light as an electromagnetic wave.

$$\nabla^2\psi + k^2\psi = 0 \qquad \textit{Equation 1}$$

Here, ψ is the amplitude of the wave and the wavenumber $k = \frac{\omega}{c} = \omega\sqrt{\varepsilon\mu}$. Since the channel is approximated as being cylindrical, it is useful to use cylindrical coordinates, as shown in Equation 2.

$$\frac{1}{r}\frac{\partial}{\partial r}\left(r\frac{\partial\psi}{\partial r}\right) + \frac{1}{r^2}\frac{\partial^2\psi}{\partial\phi^2} + \frac{\partial^2\psi}{\partial z^2} + k^2\psi = 0 \qquad \textit{Equation 2}$$

To solve the wave equation, a solution is required that can be separated into a radial, angular, and vertical part. The form of such a solution is given by Equation 3[50], where we define $\rho = r\sqrt{k^2 - h^2}$ and h is the separation constant.

$$\psi_n(r, \phi, z) = Z_n(\rho)e^{in\phi}e^{ihz} \quad (n = 0, \pm 1, \dots) \qquad \textit{Equation 3}$$

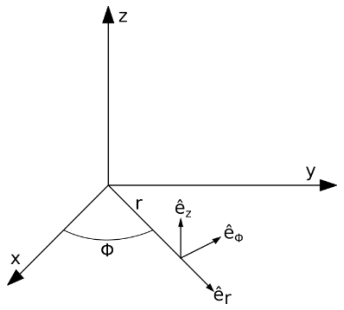

***Figure 2**. The cylindrical coordinate system used for the derivations in this chapter*

The linearly independent solutions to Z_n are the Bessel functions of the first and second kind, J_n and Y_n respectively, where n denotes their integral order. The harmonic functions for the cylinder that can be generated from Equation 3 are given as[50]

$$M_n = \nabla \times (\hat{e}_z\psi_n), \qquad N_n = \frac{\nabla \times M_n}{k} \qquad \textit{Equation 4}$$

when we take the unit vector that is parallel to the cylinder axis, $\hat{e}_z$, as pilot vector. These harmonics are then orthogonal to each other. If we now consider the interaction of a plane wave $E_i = E_0 e^{ik\hat{e}_i x}$ that is incident onto a cylinder of radius a in the direction of $\hat{e}_i = -\sin\zeta\hat{e}_x - \cos\zeta\hat{e}_z$, with ζ being the angle between cylinder axis and the incident wave, we need to express this electromagnetic wave in the cylinder harmonics that we defined above. We also need to investigate two different cases; one where electric field is parallel to the xz-plane and one where it is orthogonal to it.

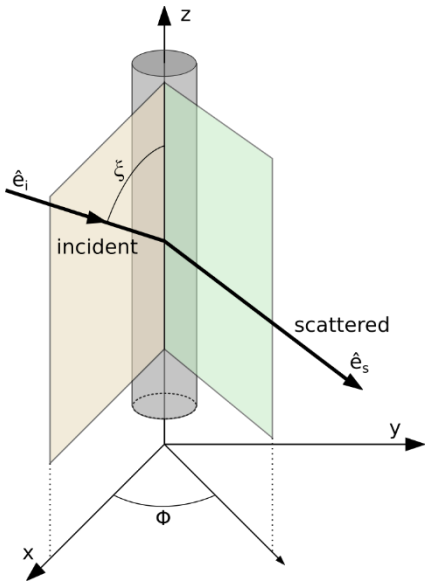

***Figure 3**. Section of the infinite cylinder used to approximate a nanofluidic channel with the Poynting vector of the incident and scattered light.*

For the first case when the electric field is parallel to the xz-plane,

$$E_i = E_0(\sin\zeta\hat{e}_z - \cos\zeta\hat{e}_x)e^{-ik(r\sin\zeta\cos\phi + z\cos\zeta)} \qquad \textit{Equation 5}$$

the expansion of this field in cylinder harmonics is given as

$$E_i = \sum_{n=-\infty}^{\infty} [A_n M_n^1 + B_n N_n^1]. \qquad \textit{Equation 6}$$

It was stated above that the Bessel functions of the second kind, Y_n, are solutions to the wave equations as well. However, at this point we must exclude them since the electric field at $r = 0$ cannot be infinite. Hence only the Bessel functions of the first kind, J_n, remain as eligible solutions. When we compare Equation 5 with Equation 3, it is also clear that the separation constant h should be $-k\cos\zeta$. Having so defined the function that generates the cylinder harmonics, $J_n(kr\sin\zeta)e^{in\phi}e^{-ikz\cos\zeta}$, we can continue following the steps in the book by Bohren and Huffman[50] to arrive at the following expressions for the coefficients A_n and B_n.

$$A_n = 0, \qquad B_n = \frac{E_0(-i)^n}{k\ \sin\zeta} \qquad \textit{Equation 7}$$

If we then define $E_n = E_0\,(-i)^n/k\sin\zeta$, the incident electromagnetic field in cylinder harmonics can now be written as

$$E_i = \sum_{n=-\infty}^{\infty} E_n N_n^1, \qquad H_i = \frac{-ik}{\omega\mu}\sum_{n=-\infty}^{\infty} E_n M_n^1. \qquad \textit{Equation 8}$$

The internal field of the cylinder in question has a similar generating function for the cylinder harmonics as the incident field, since this function is also using the Bessel functions of the first kind and needs to satisfy continuity at the boundary of the cylinder, such that $h = -k\cos\zeta$.

Here, it is now important to introduce a relation that connects to the materials inside and outside of the nanochannel. Specifically, we introduce here m, the ratio between the RI of the material that fills the cylinder ($n_{cylinder}$; in the experiments later that corresponds to a liquid or a gas) and the material the cylinder is embedded in ($n_{surrounding}$; in the experiments this will be SiO_2),

$$m = \frac{n_{cylinder}}{n_{surrounding}}. \qquad \textit{Equation 9}$$

Using this definition, the function that generates the internal field in the nanochannel is $J_n\left(kr\sqrt{m^2 - \cos^2\zeta}\right)e^{in\phi}e^{-ikz\cos\zeta}$, which is leads to the following expansions of the internal electromagnetic field

$$E_I = \sum_{n=-\infty}^{\infty} E_n[g_n M_n^1 + f_n N_n^1], \qquad H_I = \frac{-ik}{\omega\mu}\sum_{n=-\infty}^{\infty} E_n[g_n N_n^1 + f_n M_n^1]. \qquad \textit{Equation 10}$$

The scattered field assumes subsequently a similar form

$$E_s = \sum_{n=-\infty}^{\infty} E_n[b_{n1} N_n^3 + i a_{n1} M_n^3], \qquad H_s = \frac{ik}{\omega\mu}\sum_{n=-\infty}^{\infty} E_n[b_{n1} M_n^3 + i f a_{n1} N_n^3], \qquad \textit{Equation 11}$$

where the generating function $H_n(kr\sin\zeta)e^{in\phi}e^{-ikz\cos\zeta}$ is used, including the Hankel function of the first kind $H_n = J_n + iY_n$. The Bessel function of the second kind can be included here since we consider the scattered field to be an outgoing wave at large distances from the cylinder ($|\rho| \gg n^2$). Looking at the boundary conditions at $r = a$, Bohren and Huffman[50] offer the following relations for the coefficients a_n and b_n

$$a_{-n1} = -a_{n1}, \qquad b_{-n1} = -b, \qquad a_{01} = 0$$

Assuming now the common case that the incident light is normal to the cylinder axis ($\zeta = 90°$), a_{n1} vanishes and we are left with the coefficient b_n for the case of the electric field of the incident light being parallel to the xz-plane, where $x = ka$.

$$b_{n1}(\zeta = 90°) = b_n = \frac{J_n(mx)J_n'(x) - mJ_n'(mx)J_n(x)}{J_n(mx)H_n'(x) - mJ_n'(mx)H_n(mx)} \qquad \textit{Equation 12}$$

For the second case, where the incident electrical field is perpendicular to the xz-plane, the derivation for the coefficients that was laid out in Bohren and Huffman's book follows similar steps, finally arriving at an expression for a_n under the condition of normal incidence.

$$a_{n2}(\zeta = 90°) = a_n = \frac{mJ_n'(x)J_n(mx) - J_n(x)J_n'(mx)}{mJ_n(mx)H_n'(x) - J_n'(mx)H_n(x)} \qquad \textit{Equation 13}$$

We can now describe the incident, internal and scattered electromagnetic wave in terms of cylinder harmonics and have the necessary coefficients a_n and b_n available when considering the scattering from a normally incident wave of either polarization. We can therefore now calculate the scattering cross sections of our nanochannel under the approximation that it is cylinder of infinite length.

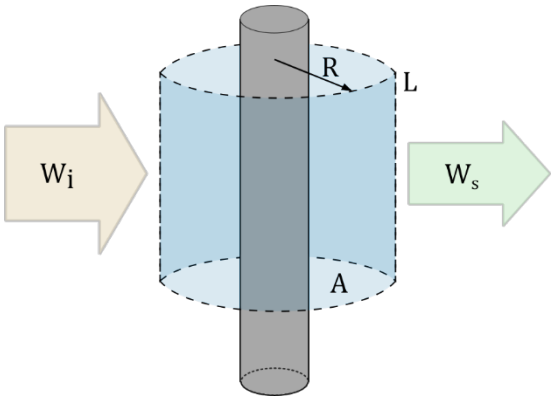

***Figure 4**. Incident light W_i and its scattered part W_s, together with the integration surface around the cylinder.*

As any infinite object would have an infinite cross section, it is advised to define the cross section with regards to a certain unit length. For this purpose, we construct a closed concentric surface around the cylindrical particle that has length L (in the direction of the z-axis) and radius R, together with a mantle surface A. This allows us to consider rates at which the incoming light is absorbed and scattered.

$$W_a = -\int_A \boldsymbol{S}\cdot\hat{\boldsymbol{n}}\, dA = W_{ext} - W_s = RL\int_0^{2\pi}(\boldsymbol{S}_{ext})_r\, d\phi - RL\int_0^{2\pi}(\boldsymbol{S}_s)_r\, d\phi \qquad \textit{Equation 14}$$

The radial components of the Poynting vector $\boldsymbol{S}$ are used above, following the definition as the cross product of the electric and magnetic field.

$$S_s = \frac{1}{2}\,\mathrm{Re}(\boldsymbol{E}_s \times \boldsymbol{H}_s^*), \qquad S_s = \frac{1}{2}\,\mathrm{Re}(\boldsymbol{E}_i \times \boldsymbol{H}_s^* + \boldsymbol{E}_s \times \boldsymbol{H}$$

Starting now with the first case that we discussed above, the incident electric field being parallel to the xz-plane, we insert the corresponding series expansions (Equation 8 and Equation 11) into the formulas above and execute the integration. This results in an expression that relates the coefficients a_n and b_n to a scattering efficiency Q_{sca}. This scattering efficiency compares the scattered radiation to the actual geometric dimension the nanochannel

$$Q_{sca,p} = \frac{W_s}{2aLI_i} = \frac{2}{x}[|b_0|^2 + 2\sum_{n=1}^{\infty}(|b_n|^2 + |a_n|^2)]. \qquad \textit{Equation 15}$$

For the second case, i.e., the electric field being orthogonal to the xz-plane, the derivation is similar and leads to the following scattering efficiency

$$Q_{sca,o} = \frac{2}{x}[|a_0|^2 + 2\sum_{n=1}^{\infty}(|a_n|^2 + |b_n|^2)]. \qquad \textit{Equation 16}$$

If the incident light is unpolarized, which is commonly the case in experiments where continuous wave light sources are used (like in my experiments), the scattering efficiency can be written as

$$Q_{sca} = \frac{1}{2}\left(Q_{sca,p} + Q_{sca,o}\right).$$

Another important simplification that we can do at this point is the assumption that we are dealing with an object that is much smaller than the wavelength of light. Specifically, if we look at x, which is defined as $x = ka = 2\pi a/\lambda$, we see that it become very small since the radius a of nanochannel I typically use in my experiments is at around 70 nm and the visible light spectrum is centered around 550 nm. This enables us to use relatively simple forms[50] of the Bessel functions needed for the coefficients a_n and b_n, that is

$$J_0(z) = 1 - \frac{z^2}{4}, \quad J_1(z) = \frac{z}{2} - \frac{z^3}{16}, \quad Y_0(z) = \frac{2}{\pi}\ln\left(\frac{z}{2}\right), \quad Y_1(z) = -\frac{2}{\pi z} \quad .$$

Inserting those expressions in Equation 11 and Equation 12 then yields the necessary coefficients for the scattering efficiencies, provided that only the terms with the smallest degree in x are considered.

$$a_o = \frac{-i\pi x^4(m^2-1)}{32}, \qquad b_o = \frac{-i\pi x^2(m^2-1)}{4}$$
$$a_1 = \frac{-i\pi x^2}{4}\left(\frac{m^2-1}{m^2+1}\right), \qquad b_1 = \frac{-i\pi x^4(m^2-1)}{32} \qquad \textit{Equation 17}$$

From here, we can go back to Equation 15 and Equation 16. Using only the terms with the highest contribution, we arrive at the following expressions for the scattering efficiencies for parallel and orthogonal incident light.

$$Q_{sca,p} = \frac{\pi^2 x^3}{8}(m^2-1)^2 = \frac{\pi^2 k^3 a^3}{8}(m^2-1)^2 \qquad \textit{Equation 18}$$

$$Q_{sca,o} = \frac{\pi^2 x^3}{4}\left(\frac{m^2-1}{m^2+1}\right)^2 = \frac{\pi^2 k^3 a^3}{4}\left(\frac{m^2-1}{m^2+1}\right)^2 \qquad \textit{Equation 19}$$

These efficiencies are given with respect to the projected surface $2aL$ that normally incident light "sees" when approaching the cylindrical nanochannel. To finally be able to write down the equations that define the nanochannel scattering cross sections, the above equations need to be multiplied by this projected surface. While doing so, the geometric nanochannel cross section, $A_\emptyset = \pi a^2$, emerges and the scattering cross sections for parallel and orthogonal polarization can be written as

$$\sigma_{sca,p} = \frac{A_\emptyset^2 k^3 L}{4}(m^2-1)^2 \qquad \textit{Equation 20}$$

$$\sigma_{sca,o} = \frac{A_\emptyset^2 k^3 L}{2}\left(\frac{m^2-1}{m^2+1}\right)^2 \qquad \textit{Equation 21}$$

If we finally assume unpolarized light irradiation, as in my experiments, we average both scattering cross section and arrive at Equation 22, which is the fundamental formula for nanochannel scattering microscopy.

$$\sigma_{sca,u} = \frac{A_\emptyset^2 k^3 L}{4}(m^2-1)^2\left(\frac{1}{2} + \frac{1}{(m^2+1)^2}\right) \qquad \textit{Equation 22}$$

Its importance is given by the fact that it combines the measured scattering intensity (through the scattering cross section) via the geometry of the fluidic system (channel dimensions) to the

properties of the medium inside the channel. We can see from this formula that a short wavelength and a large channel would in principle be beneficial for an improved scattering signal. On the other hand, in the context of measuring reaction product formed on a single catalyst nanoparticle, a large channel would lead to a more diluted product concentration in the and thus a reduced RI contrast, which consequently would reduce the sensitivity in that way. The ideal channel for NSM when used for single particle catalysis is therefore large enough to be a good scatterer but also small enough to keep the reaction products from one single nanoparticle concentrated. On a side note, it is interesting to see that if we assume a RI ratio of $m = 0.9$, the cross section for the parallel incident light contributes around 63% to the combined cross section, indicating thereby another way how the sensitivity could possibly be enhanced, i.e., by using polarized rather than unpolarized light.

2.1.2 The Kramers-Kronig relation

In the preceding section, I laid out how the scattering of light from a nanochannel depends on the difference in RI between the material inside the channel (in my case a fluid) and the material that surrounds it, and how changes in this difference induced by a catalytic rection occurring inside a channel can be detected by monitoring correspondingly induced changes in scattering intensity. However, a further interesting aspect is here that the RI in general is wave-length dependent. To this end, while liquids like pure water or transparent solids like SiO_2 exhibit refractive indices that are fairly constant across the visible spectral range, there are fluids that exhibit distinctly wavelength-dependent refractive indices, and thus also exhibit a sizable light absorption. These fluids are in most cases (aqueous) solutions of dyes, such as Pyranine, Quinoline or Coumarin, but can in principle be any compound that absorbs specific wavelengths of the visible spectrum as for example metal complexes. These absorption features lead to strongly spectrally modulated light scattering properties of a nanochannel filled with such a fluid, which in turn can be used to quantitatively analyze changes in the fluid in a spectrally resolved way.

The key to understand this effect is to understand the Kramers-Kronig relation. In a mathematical sense, this relation connects the real and imaginary part of a complex function that is analytic in the upper half plane and vanishes sufficiently fast for large arguments[51]. This complex function is the refractive index $\boldsymbol{n}(\omega) = n(\omega) + i\kappa(\omega)$, since it contains in its real part the index for diffraction and in its imaginary part the extinction coefficient. With this information at hand, we can write the Kramers-Kronig relation as[52]

$$n(\omega) - 1 = \frac{2}{\pi}\mathcal{P}\int_0^{-\infty} \frac{\omega'\kappa(\omega')}{\omega'^2 - \omega^2}\, d\omega' \qquad \textit{Equation 23}$$

where $\mathcal{P}$ denotes the Cauchy principal value of the integral. We now rewrite this equation with the use of the optical wavelength $\lambda = 2\pi c/\omega$, such that

$$\Delta n(\lambda) = n(\omega) - 1 = \frac{2}{\pi}\mathcal{P}\int_0^{-\infty} \frac{\kappa(\lambda')}{\lambda'\left(1 - \left(\frac{\lambda'}{\lambda}\right)^2\right)} d\lambda' \qquad \textit{Equation 24}$$

The relation between κ and the experimentally measurable absorption coefficient α is given by

$$\kappa(\lambda) = \frac{\alpha\,\lambda}{4\pi} \qquad \textit{Equation 25}$$

With this relation at hand, we can relate an experimentally determined absorption coefficient to the real part of the RI, as demonstrated by Sai et al[51]. In addition, and of key importance for my work, the above means that we can measure changes in the absorption coefficient of a fluid inside a nanofluidic channel in a spectrally resolved way by measuring the wavelength-dependent scattering from the nanochannel. This, in turn, opens the possibility to identify chemical compounds inside a nanofluidic channel based on their distinct spectral "fingerprint" derived from the light scattering signature of the channel. Below, in Chapter 2.3.2, I will demonstrate this concept on the example of the dye Brilliant Blue and for Allura Red in Chapter 2.4.2.

2.2 Nanofabrication of fluidic chips

Nanofluidic systems offer unique opportunities to manipulate and control fluids, both liquid and gas, at the nanoscale. Modern micro- and nanofabrication methods allow almost limitless possibilities to realize the most diverse nanofluidic designs tailored for different purposes - at least when it comes to two-dimensional architectures I used in my work. To this end, all nanofluidic systems I have used were fabricated using the facilities of the MC2 Nanofabrication Laboratory at Chalmers, which offers all the tools needed to fabricate high-end nanofluidic systems. However, while it is a true "luxury" to be able to design and nanofabricate nanofluidic devices with intricate functionalities, as I have learnt and will further outline below, it also constitutes a significant risk in terms of overengineered complexity. In fact, the most important results I have obtained used the simplest chip designs I have worked with. That said, the lessons learnt from exploring different and more complex chip designs that I discuss below have proven instrumental for both the development of NSM for single particle catalysis and the fundamental understanding of its (practical) limitations. Below, I will now provide a short summary of the key micro- and nanofabrication steps used to make such nanofluidic chips.

As a common denominator, all fluidic systems used and built for my work featured two microfluidic systems that constitute the chip in- and outlet system, which is connected to the outside world on one end and to a set of straight and parallel nanochannels on the other end (**Figure 4**). In this design, the microchannels are used to transport fluids to and from the nanochannels on the in- and outlet side, respectively. On both the inlet and outlet side, they are connected to circular reservoirs that are used for filling the fluidic system with the desired liquid. Note that in this way two different liquids can be applied on either side of the nanochannels.

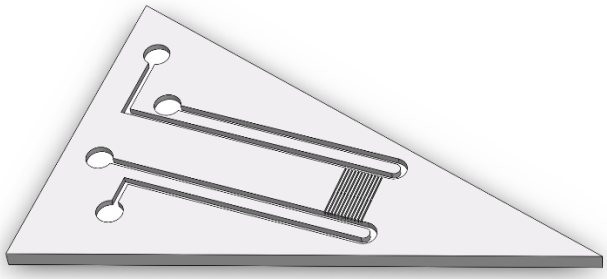

Figure 5. Rendition of a basic nanofluidic chip. Here, four inlet areas are connected via microchannels to a set of parallel straight nanochannels located at the tip of the triangular chip comprised of a thermally oxidized silicon wafer.

The micro- and nanofabrication approach used for all fluidic systems I have designed is based on so-called top-down processing into thermally oxidized silicon substrates (circular 4-inch wafers), followed by the sealing of the fluidic structures by thermally bonding glass wafers (Borofloat 33, 4 inches) onto the structured substrate. This provides both a hermetic seal and optical access to the fluidic systems from the side of the lid, which is critical for optical microscopy.

The micro- and nanofabrication process consists of the following steps:

1. Silicon wafers with (100) orientation were cleaned with a standard process. For this purpose, the wafers were first treated in SC1 (5:1:1 H_2O:NH_3OH:H_2O_2, 80°C) for 10 minutes, rinsed in deionized water, native oxide removed with 2% HF (10 seconds), rinsed again in deionized water, then treated in SC2 (5:1:1 H_2O:HCL:H_2O_2, 80°C) for 10 minutes, rinsed a final time in deionized water and then spun dry.

2. The cleaned wafers were thermally oxidized in an oxidation furnace in a water atmosphere at 1050°C. Depending on the planned application, oxide layers with a thickness of 200 nm or 2000 nm were produced. The thinner oxide layers were used when the nanochannels processed in the next step, with a typical depth of 150 nm, should have little oxide between them and the underlying silicon substrate. Accordingly, the thicker oxide layers served for cases where the distance between the nanochannels and silicon should be as large as possible.

3. In the next step, nanochannels were etched into the thermally grown oxide using reactive ion etching (RIE). For this, a 20 nm thick structured Cr layer was used as a hard mask due to its high etch resistance against the plasma used for etching the nanochannels into the oxide layer. To structure the Cr layer, a 200nm thick layer of electron beam resist (ARP6200) was prepared on top of it and the pattern of the nanochannels was defined inside that polymer layer with electron beam lithography (development in o-xylene). The pattern

created in the polymer layer was then transferred into the Cr- layer (the hard mask) with RIE using chlorine (Cl2), and the pattern in the hard mask was finally transferred into the oxide with RIE using fluorine (NF3). In the case of creating channels with vertical constrictions, the RIE of the thermal oxide was divided into two steps: (i) etching of all structures to the depth of the constrictions, and (ii) etching of all structures except the constrictions to the full depth of the nanochannels. To achieve the selective etching of the second step, protective 1 µm wide lines of photoresist (AZ5214E) were fabricated with direct laser lithography on top of the hard mask at the positions of the constrictions between the two etch steps.

4. All larger microfluidic structures were etched into the surface using RIE. For this purpose, an etching mask made of photoresist was used, which was typically structured using direct laser lithography (**Figure 6**).

5. Finally, to connect the fluidic system that now is hermetically sealed by the lid to the outer world to make it accessible for experiments, we etched holes through the silicon wafer substrate using reactive ion etching (DRIE) to provide access from the back side of the chip. In cases where a connection to the fluidic systems was used from the front side, i.e., through the glass lid, we sandblasted holes through the glass at appropriate locations.

6. For nanofluidic chips with lithographically placed nanoparticles inside the nanochannels, an additional processing step was included at this stage of the process. The nanoparticles were defined as holes with electron beam lithography (**Figure 7**) in a double layer of resist (copolymer and PMMA) spun onto the structured substrate, and the material of choice for the nanoparticles was deposited with electron beam evaporation through the holes in the resist mask. Finally, the resist mask was dissolved in acetone leaving only the nanoparticles at the defined positions on the substrate.

7. In a final processing step, the substrates were thoroughly cleaned by treating them in SC1 (5:1:1 H_2O:NH_3OH:H_2O_2, 80°C) for 10min followed by a rinsing step in DI water and blow drying with N_2. Glass wafers of 175 µm thickness were cleaned in the same manner, O_2-plasma treated (50W RF power, 250 mTorr) together with the processed substrates and thermally bonded to the substrates at 550°C for 5hrs prior to dicing them into individual fluidic chips used for the catalysis experiments.

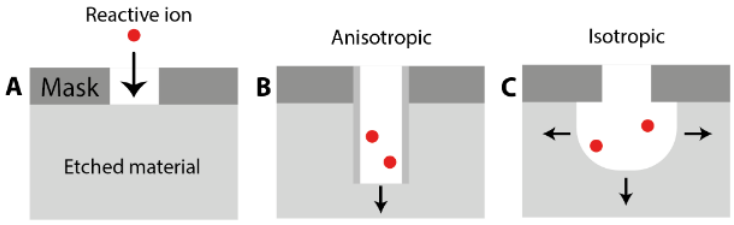

***Figure 6**. Reactive ion etching (RIE). a) A reactive ion (fluorine for SiO_2 etching, oxygen for polymers) is accelerated in an electric field towards the substrate, knocking out atoms from the surface and/or chemically reacting and forming volatile compounds that then detach from the surface. Thereby RIE removes material from areas where the substrate is not protected by the mask. b) Anisotropic etching can be achieved by tuning the ratio of physical and chemical etching or by protecting the side walls with a polymer in cycled steps between the etching. c) Isotropic etching of the substrate is achieved by leaving the side walls unprotected and tuning the etching parameters. Adapted work*[53].

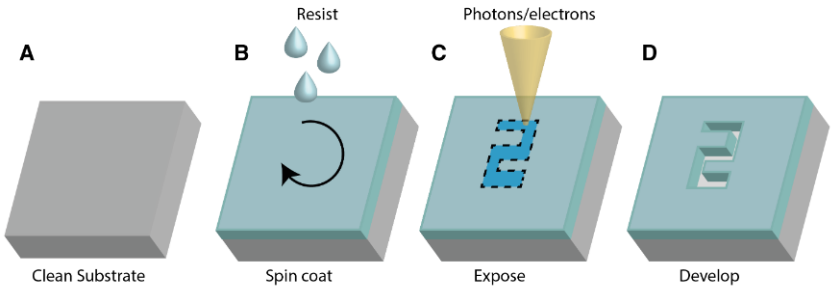

***Figure 7.** Nanolithography. A clean substrate (a) is spin coated with a polymer-based resist that is sensitive to exposure to electrons or photons (b). c) Exposing the resist to light or electrons alters its structure, e.g., through cross-linking or splitting of polymer chains, such that it becomes (in)soluble in specific solvents and can be removed in the exposed areas during the development step (c). Adapted work*[53].

2.3 The microscope setup and first results

2.3.1 The setup

For my experiments, I used dark-field scattering microscopy where the name stems from the illumination scheme. In contrast to bright-field microscopy, where the light that is transmitted through the sample or reflected from it, we monitor here only light that is scattered from the sample. For this, a special objective with high numerical aperture is needed that illuminates the sample surface at a shallow angle and at the same time only collects scattered light (**Figure 8**).

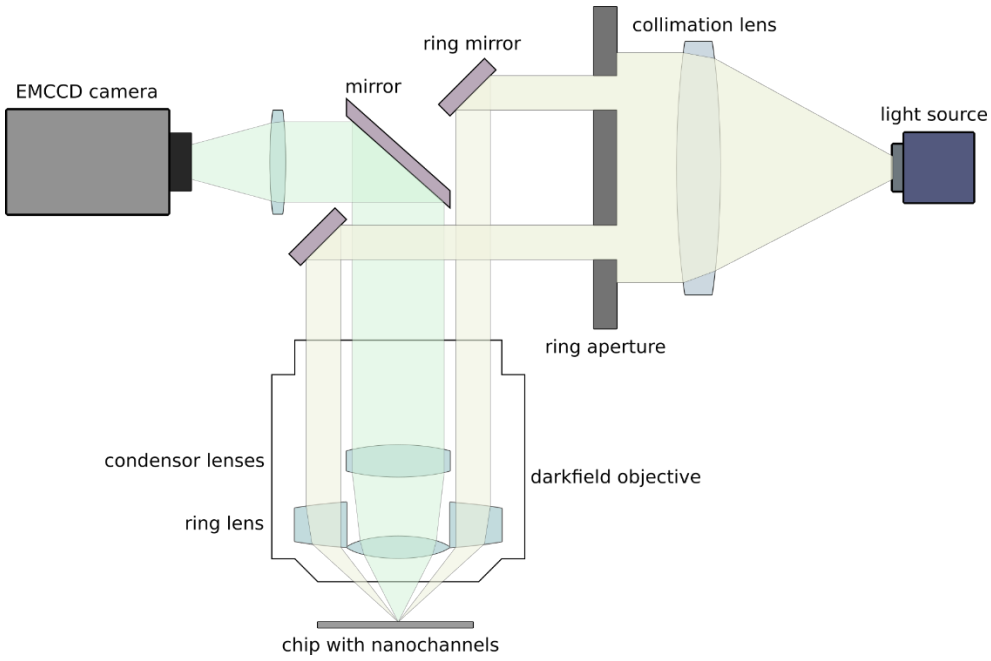

***Figure 8**. Schematic of the darkfield microscopy setup used for the nanofluidic scattering microscopy experiments.*

For the work presented in this thesis, I used three different microscopes with different characteristics, light sources and cameras. However, their principle of operation was the same in the sense that they all were operated in dark field scattering mode. Below, I will describe the setup I used in the early phase of my project, together with correspondingly obtained results.

This first setup was comprised of an upright Nikon Eclipse LV 1000 microscope equipped with a Nikon TU Plan ELWD 50x/0.60B darkfield objective and a Märzhäuser Wetzlar Tango 3 Desktop electronic microscope stage. For illumination, I used a Nikon LV-LH50PC halogen lamp, which produces a relatively even spectrum across the visible regime (**Figure 10**). The scattered light collected by the darkfield objective was directed into a Andor Shamrock SR-303i-B spectrometer before being recorded by a Andor Newton DU920P-BR-DD CCD camera. If not used in spectroscopic mode, that is to measure scattering intensity as a function of wavelength, the 150 l/mm grating of the spectrometer can be adjusted such that the 0^{th} maximum reproduces the microscope image onto the CCD camera, thereby enabling operation of the setup in imaging, rather than spectroscopy, mode. This enables the imaging of a large number of nanochannels in parallel (as I did later in this thesis, see **Figure 28**). In contrast, when operated in spectroscopy mode, only a single channel can be analyzed since the image of the channel has to be aligned with the entrance slit of the spectrometer.

To start an experiment, I introduced the necessary liquid(s) to the system by filling reservoirs in the chuck that host the fluidic chip and that connect to the reservoirs in the chip at the end of the microfluidic systems of (**Figure 9**). Once filled with liquid, by applying pressure (typically 2 bar) to these reservoirs via a system of pressure pipes, I then control the direction of liquid flow through the chip, as well as the flow rate. To exchange the liquid(s) in the system, the chuck was opened, the present liquid extracted from the reservoirs with a syringe and the new liquid was filled in.

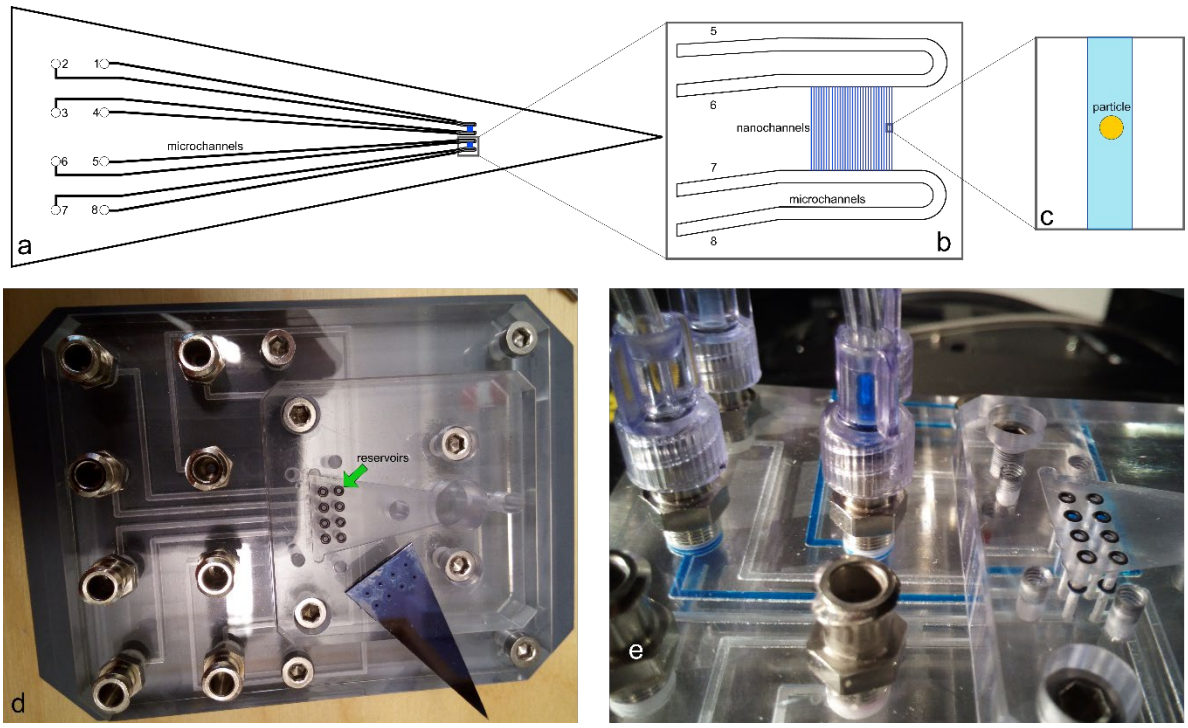

***Figure 9**. a)-c) Schematic of the fluidic design of my first chips with the microchannels in black, the nanochannels in blue and the position of a single nanoparticle in yellow. d) The chip holder, also referred to as chuck, with the fluidic chip mounted on top. The chip is shown from its inlet (holes) side. c) Detail of the chuck, where two inlet channels have been filled with Brilliant Blue solution for highlighting the pathway of the liquid into the chip. The attached pipes lead to the pressure source used to control the flow through the chip.*

2.3.2 Wavelength-resolved scattering intensity measurements of transparent liquids

As laid out in chapter 2.1.1, the light scattering properties of a nanochannel are defined by its geometry and by the ratio of the refractive indices of the material surrounding the channel (SiO_2) and the liquid inside the channel. To verify the corresponding theory I have presented above in a first experiment using transparent liquids with different RI, I measured the spectrally resolved scattering intensity of light from a single nanochannel filled with pure Milli-Q water and of the same channel filled with a 30 % aqueous H_2O_2 solution (**Figure 10**). The procedure for these first measurements was as follows: All 4 reservoirs for one side of the chip in the upper transparent part of the chuck were filled with water, and the chip screwed on top with the inlet holes pointing down. 2 bar pressure was applied to two of the reservoirs so that the water was pressed in via the holes into the microchannels and established a flow through them. After several minutes in this state, the pressure from one of the inlet holes was lifted, such that one microchannel now had an overpressure of 1 bar at the entrance to the nanochannels with respect to the microchannel at the other side of the nanochannels. This pressure difference across the nanochannels then initiated a flow through them and enabled their complete filing with water after several minutes. While the chip was being flushed with water in this way, the

chuck was placed under the microscope, with the nanochannel area positioned in the center of the field of view of the camera. From the 340 µm overall length of the nanochannels, 170 µm fit the field of view. Notably, it is important to not include the connection of the nanofluidic system to the microchannels in the field of view to avoid background scattering form the microchannel walls. To measure scattering spectra from a single nanochannel, I closed the entrance slit of the spectrometer such that only the scattering signal from a single nanochannel is recorded. By then setting the center wavelength of the grating to 641 nm, spectrally resolved scattering intensity can be measured along the nanochannel aligned with the slit of the spectrometer. Typically, for such a measurement I accumulated 10 frames with 0.5 s exposure time per frame and took the average. To further reduce readout noise and minimize the amount of data, the whole spectrum was binned along the nanochannel in the camera if no spatially resolved spectroscopic measurement was required.

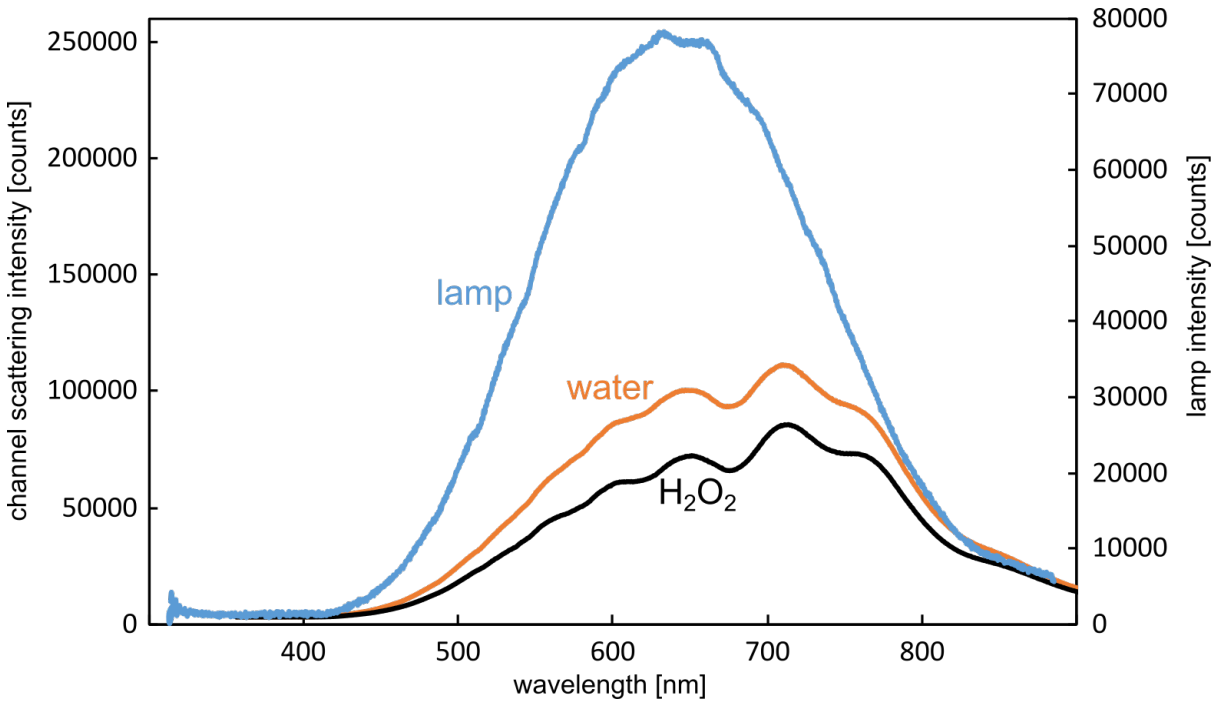

Figure 10. *Emission spectrum of the halogen lamp (blue) used for sample illumination obtained by measuring the light scattered from a reflectance standard, together with the spectrally resolved raw and unreferenced light scattering intensities from a single water-filled nanochannel (orange) and the same channel subsequently filled with a 30 % aqueous H_2O_2 solution (black). The lamp spectrum is drawn on the secondary y-axis as the acquisition settings were different.*

Analyzing the correspondingly obtained scattering spectra in **Figure 10** reveals a Gaussian intensity distribution for the lamp spectrum, with small features at the peak, which is expected for a halogen lamp[54]. In comparison, both scattering spectra from the nanochannels still show an intensity distribution that is close to a bell shape, but they are also clearly deformed and show additional features. The origin of these changes is not found in the optical path between chip and camera, as the lamp spectrum was recorded the same way, but it lies within the

scattering properties of the fluidic chip itself. Water[55] and H_2O_2[56] show significant absorption only above 700 nm and below 300 nm, which means that they can be regarded as fully transparent in the wavelength range we discuss here. Hence, the most remarkable observation that we make in this experiment is the overall scattering intensity difference measured for the channel filled with water and 30 % aqueous H_2O_2 solution, respectively. The explanation for this observation is indeed the RI difference between the two liquids, as outlined in detail below.

The key result of the theoretical derivation in chapter 2.1.1 was Equation 22, which connected the scattering cross section of a nanochannel to the RI difference between the medium inside and outside of the channel. I will now use this equation to plot the theoretical scattering cross section for a 140 nm x 140 nm nanochannel of 170 µm length that is illuminated by 550 nm light (**Figure 11**.). To show the general behavior of this function, the RI range for the medium inside the channel is varied from 0.8 refractive index units (RIU) to 2.4 RIU.

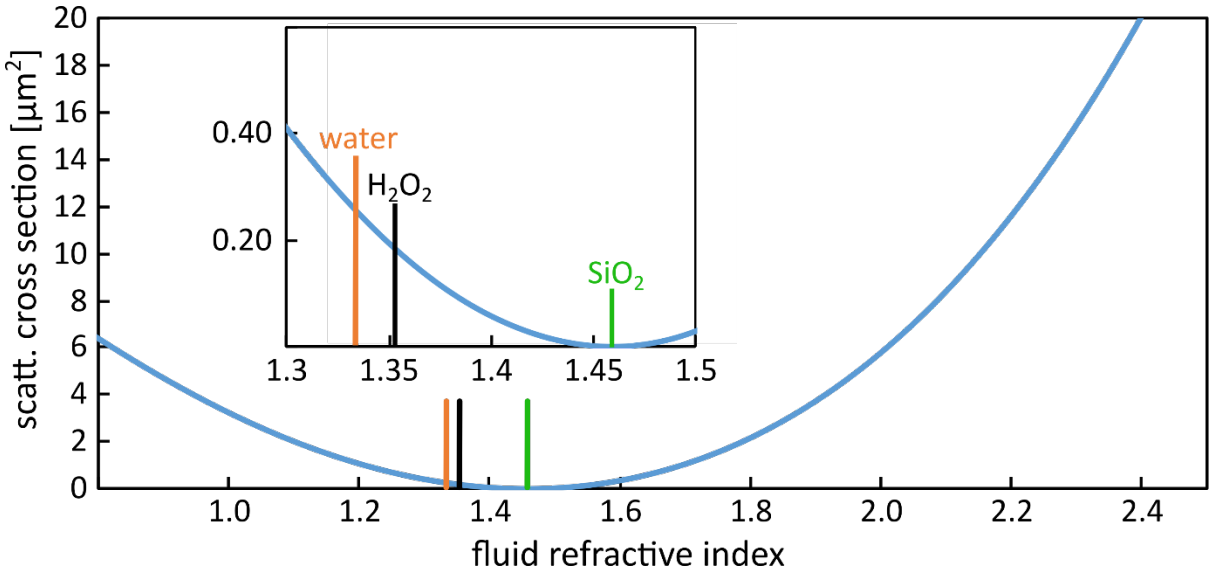

***Figure 12**. Theoretical scattering cross section (blue) of a 140 nm x 140 nm nanochannel of 170 µm length calculated using equation 22 and plotted over a wide range of refractive indexes for the medium inside the channel. The markers indicate the refractive indexes for SiO_2 (1.4585 RIU), water (1.3333 RIU) and a 30% aqueous H_2O_2 solution (1.3529 RIU).*

The RI dependence of the calculated nanochannel scattering cross section exhibits a minimum at exactly the RI value of SiO_2 (1.4585 RIU)[57]. The explanation can be found by analyzing Equation 22 or by considering that a channel filled with SiO_2 while being also embedded in SiO_2 would be optically invisible since no light could scatter from it. Hence, its scattering cross section (SCS) is zero. When the channel is filled with water (1.3333 RIU)[58], however, we see that the SCS of the channel is now approx. 0.28 µm^2. This means that the channel will now scatter light efficiently and will become visible in an experiment such as the one summarized in Figure 10. Exchanging now the liquid in the channel from pure water to an aqueous 30% H_2O_2 solution, we also change the RI to 1.3529 RIU[59] which according to equation 22 yields a SCS of 0.19 µm^2, which is significantly lower that for the water filled channel (see also inset in **Figure 13**.). This is the explanation for the result that we see in the measurement shown in **Figure 10**, where indeed the scattering intensity of the water filled nanochannel is higher than for the H_2O_2 filled one.

2.3.3 NSS of a Brilliant Blue solution

Having experimentally corroborated the theoretical background of NSM introduced in chapter 2.1.1 for measuring RI induced changes in light scattering intensity of a single nanochannel filled with different *transparent* liquids in chapter 2.3.1, it is now interesting to perform similar experiments with a liquid that *absorbs light* in the visible range to show the connection between experiment and the theoretical prediction by the Kramers-Kronig relation (Equation 24).

Specifically, I used for this test the (former) food dye Brilliant Blue, due to its non-toxicity and strong absorption in the visible, and a nanofluidic system comprised of nanochannels with the same dimensions as for the test with the transparent H_2O_2. The experimental procedure is identical to the one described above, with the exception that now I filled one reservoir of the inlet microchannel with water while the other reservoir of the same microchannel was filled with the Brilliant Blue dye solution. By doing so, I could now exchange the liquid in front of the nanochannels by switching the pressure from one reservoir to the other, without having to remove the fluidic chip from the microscope. The solution that I used had a concentration of 50 mM Brilliant Blue in water and was prepared by dissolving solid dye powder in ultrapure MilliQ water.

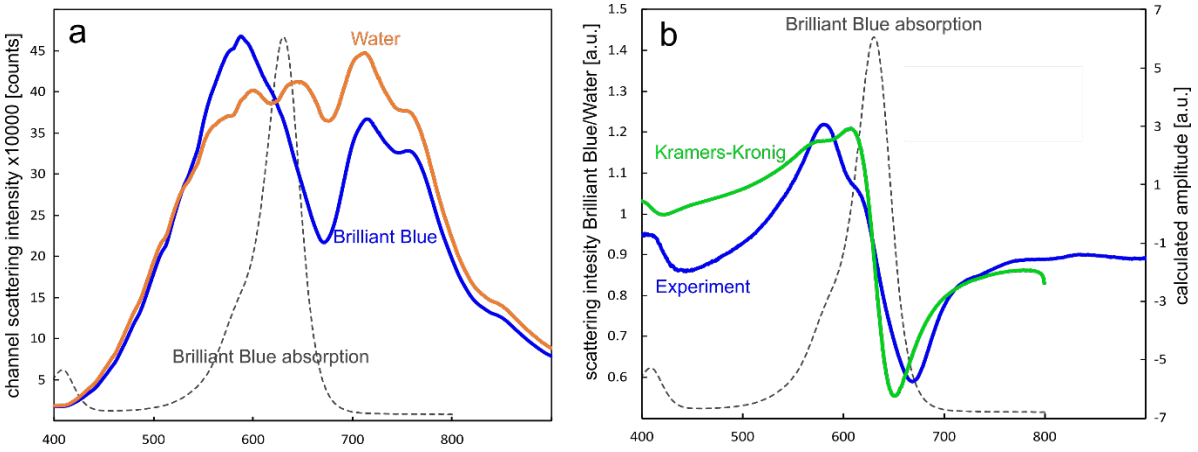

***Figure 14**. a) Experimentally measured scattering spectra of a single nanochannel filled with pure water (orange line) that was subsequently replaced by a 50 mM Brilliant blue solution (blue line). Also shown is the absorption spectrum of Brilliant Blue[60] (dashed black line). b) Dividing the spectrum of the dye-filled channel filled by the spectrum of the water filled channel yields the referenced experimental scattering spectrum for the Brilliant Blue dye (blue line). It is plotted together with the RI spectrum (green line) calculated using the Kramers-Kronig relation (Equation 24) with the absorption spectrum (black dashed line) as input.*

The impact of the dye solution on the scattering intensity spectrum of a single nanochannel is clearly visible already in the raw spectrum (**Figure 14a**). Specifically, we see a drastic reduction of the scattering around 670 nm, while the scattering is enhanced around 587 nm when comparing to a water-filled channel. This is, at first, a somewhat puzzling result since if it only were light absorption of the dye that is seen in the spectrum, we would only expect a reduction of the scattering intensity and not an increase as we see around 587 nm. It is also curios that these distinct peaks appear in wavelength ranges where the absorption of the dye increases or decreases, respectively.

To understand this, we remind ourselves that the origin of the measured scattering intensity spectrum is to be found in Equation 22, where that SCS depends on the refractive index of the medium inside the channel. Knowing the Kramers-Kronig relation (**Equation 24**), we know that the refractive index of a medium can be wavelength dependent and is connected to its absorption spectrum. When we now want to know how the refractive index changes with the wavelength, we need to insert the absorption spectrum of our dye Brilliant Blue (shown in **Figure 14**) into the Kramers-Kronig relation and perform a numerical integration. The resulting refractive index spectrum is shown in **Figure 14b**. Also plotted is the scattering spectrum of the nanochannel with the Brilliant Blue solution, which has been divided by the scattering spectrum of the water filled channel to show only the features that stem from the dye itself.

It is evident that the theoretical spectrum calculated using the Kramers-Kronig relation, and the experimentally measured spectrum have a very similar shape. More specifically, the peaks at 586 nm are very similar in both curves and the shoulder seen at 612 nm in the experimental curve corresponds to the peak in the theoretical spectrum at the same position. Similarly, the (negative) peaks at 660 nm are close for both curves, even though their position differs slightly. In summary, from this analysis it becomes clear that those distinct peaks appear in the refractive index spectrum at positions where the absorption spectrum changes rapidly. This opens the door to using NSM to specifically identify chemical compounds (formed) inside a nanochannel during a catalytic reaction via the scattering spectrum. Hence, it essentially establishes widely used optical absorption spectroscopy inside nanofluidic channels on tiny liquid volumes, which constitutes a significant step beyond the state of the art.

Concluding these first two experiments with both a transparent and light absorbing liquid in a single nanochannel, I want to highlight that wavelength resolved NSM, which we from here on forward call Nanofluidic Scattering Spectroscopy (NSS), indeed enables the characterization of a liquid inside a single nanofluidic channel based on its RI, in good agreement with the corresponding theoretical predictions. On the other hand, if a solution that is transparent in the visible regime is to be investigated, monitoring a scattering intensity change is most convenient and proportional to the RI of the liquid in the channel (Equation 22). For liquids that have an absorption band in the wavelength range of interest, in addition to monitoring scattering intensity changes proportional to concentration in NSM, we can use the spectral resolution provided by NSS to quantitatively extract absorption spectra of the liquid inside a single nanochannel using the Kramer-Kronig relations. Thereby it becomes possible to obtain a spectral fingerprint of the composition of the liquid inside the channel and potentially monitor changes in this composition in a quantitative way.

2.4 Setup and nanofluidic chip refinement towards single particle catalysis

2.4.1 First stage of refinements

This first stage in the refinement of NSM and NSS towards single particle catalysis applications included several changes and improvements of the microscope setup itself, the chuck holding the chips, the nanofluidic chip design and data treatment and evaluation.

On the microscope side, I started to use a Nikon Eclipse LV1500N upright microscope equipped with a Nikon TU Plan ELWD 50x/0.60B darkfield objective and a Prior H101P2NLV/A electronic microscope stage. As the key difference, this setup features an Andor Newton DU920P-BEX2-DD CCD camera with higher sensitivity towards shorter wavelengths of the visible spectrum. The second main difference is to be found in the Andor Shamrock SR-193I-A-SiL spectrometer onto which the camera is mounted, since it is in addition to the 150 l/mm diffraction grating also is equipped with a mirror that enables efficient imaging of nanofluidic samples since it ensures a higher photon throughput to the camera. Finally, since the scattered light intensity measured is proportional to the incident light intensity, I also exchanged the halogen lamp used for sample illumination in my first experiments to a Thorlabs Solis 3C LED lamp with a 4 W power output. This, in turn roughly doubled the scattering intensity from a single channel and enabled a higher time resolution in my experiments, as the exposure time to saturate the camera can be shortened. Furthermore, it features a very short stabilization time and essentially zero intensity drift over time, such that the output power can be regulated without waiting time and all frames of a time series are comparable to each other.

A further significant hardware improvement was a Fluidgent MFCS-EX-5C multichannel pressure controller that allows the accurate electronic control of the pressure applied to up to 8 separate channels in the range from 2 mbar to 7 bar. In this way, it enables the very accurate control of the liquid flow through my chips across a wide range and in a more reproducible way than the manual pressure controller I used for the first series of experiments. An additional key aspect of this device is that it enabled me to control electronically all key components of the experimental setup, i.e., the microscope stage, the spectrometer, the camera, and the flow control system. Consequently, it became possible to fully automatize my measurements, as I describe in detail further below in chapter 2.4.2.2. This constitutes an important advance because we aimed to measure more channels simultaneously in a consistent manner and because it enables more effective use of working time.

To improve the flexibility of my experiments in terms of using more sophisticated and intricate nanofluidic chip designs, such as the inclusion of reference nanochannels I will discuss in detail below, we also designed a new chuck that is able to host an entire 4-inch wafer (rather than just a triangular slice of it as shown in **Figure 1** and **Figure 9**). It therefore provides more space on the chip for complex fluidic designs (**Figure 15**). This chuck featured 8 liquid inlet connections equipped with glass tubes for compatibility both with organic solvents and other chemically harsh liquids (the glass tubes can be seen in **Figure 20a** in the transparent perimeter of the chuck.

Concerning the new chip design, it included the following key points:

(i) The addition of different arrangements of Au catalyst nanoparticles inside the nanofluidic channels at a predefined position using electron beam lithography (**Figure 7**). These nanoparticles all had a thickness of 20 nm, a diameter of 50 nm and were placed in parallel nanochannels in different numbers, that is, 1, 5, 10, 100 and 200 particles per channel. In addition, we also decorated nanochannels with nanoparticles with 100 nm diameter and in the same numbers as the 50 nm particles.

(ii) The implementation of colinear empty (i.e., without particles) reference nanochannels with dead ends placed above and below to the reaction channels with the particles (**Figure 15b/c**). These reference channels serve the purpose to remain filled with a reference liquid (water for the work presented in this thesis) during the entire experiment while in the particle-filled channels the liquid/reactants are exchanged. In this way, simultaneously measuring the optical response from the reference channels and the channels in which the catalytic reaction occurs, enables the continuous optical referencing of the reaction channels (**Figure 15c**). This is expected to eliminate intensity fluctuations and drifts from the light source, as well as effects from slow microscope defocusing and background scattering from the measured signal.

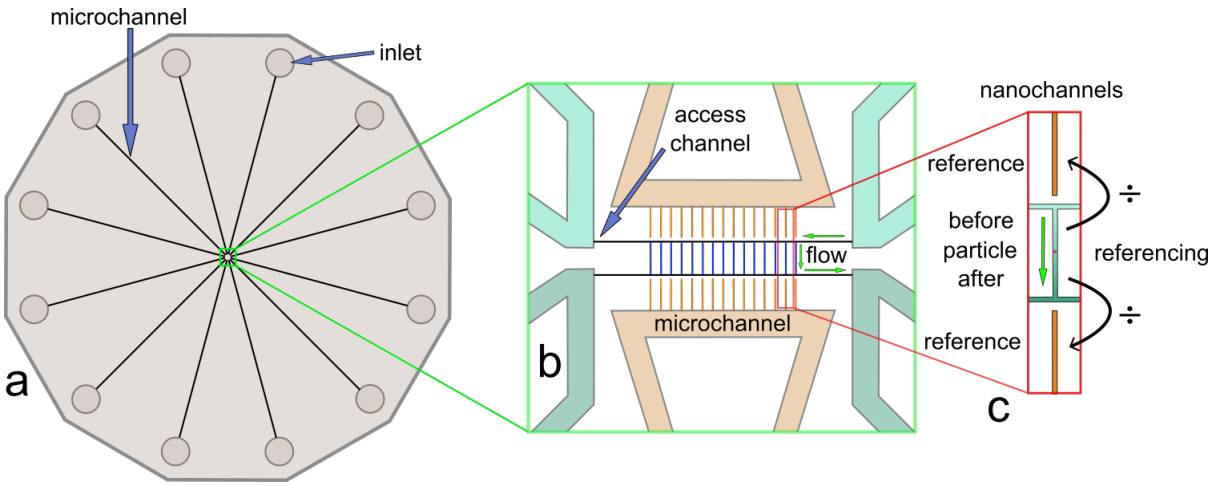

***Figure 15**. Schematics of the new fluidic chip design. a) The fluidic chip was fabricated from a 4-inch silicon wafer. Inlets are positioned on the outer border of the wafer with microchannels connecting them to the nanochannels in the middle. b) Nanochannel area, showing the nanochannels containing the particles in the middle (blue) and the isolated reference channels (orange). Flow of reagents into the nanochannels is established via the access channels that are connected to the microchannels leading to the inlet reservoirs. c) Enlarged nanochannel arrangement showing the isolated reference channels that are colinear with the nanochannel containing the particle(s) and localized both above and below the reaction nanochannels. In this way, the reaction channels and the reference channels could be placed in the slit of the spectrometer and recorded spectrally at the same time.*

At the global level, even with these new features, the basic fluidic system design used was retained and featured microfluidic in- and outlet systems as before that connected to the nanofluidic system comprised of parallel nanochannels that this time either are empty (dead end reference channels) or decorated with a specific number of nanoparticles (reaction

channels). As the main difference, the inlet reservoirs are now arranged in a circular fashion around the entire wafer (see also **Figure 20a**) and the chip features two separate fluidic systems that can be filled and controlled independently: (i) the reaction system with parallel nanochannels featuring the Au particle arrangements and (ii) the reference system with the empty nanochannels (**Figure 15**).

To then prepare an NSS measurement of a reaction in a single nanochannel, the entire fluidic system of the chip, that is, both reference and reaction systems, were filled with water to measure a scattering spectrum of all channels and channel regions of interest: (i) the upper reference channel, (ii) the section of the reaction channel upstream of the particle, (iii) the section of the reaction channel downstream of the particle, (iv) the lower reference channel. When subsequently comparing the scattering spectrum taken from the reaction channel upstream of the particle with the upper reference channel spectrum (and likewise for the downstream fraction of the reaction channel and the lower reference channel) as shown in **Figure 15c**, we obtain the intrinsic difference in light scattered from the selected fraction of the reaction channel and the corresponding reference channel. In this way, during a catalysis experiment in the reaction channel, we can subtract all non-reaction related contributions to the measured scattering spectra by subtracting the simultaneously measured scattering response from the scattering channels adjacent to the up- and downstream fractions of the reaction channel, thereby hopefully increasing the resolution of our system.

With this upgraded microscope setup and the new chip design at hand, I took the step to for the first time attempting the study of a catalytic reaction on the Au nanoparticle arrangements inside my nanochannels. As the model reaction, I used the catalytic degradation of the azo-dye Allura Red with the strong reductant sodium borohydride ($NaBH_4$). Allura Red has a distinct absorption band in the 500 nm wavelength region (**Figure 16a**), such that I expect a broad peak in the scattering spectrum between 500 nm and 600 nm when flushing the solution in the nanochannels[60].

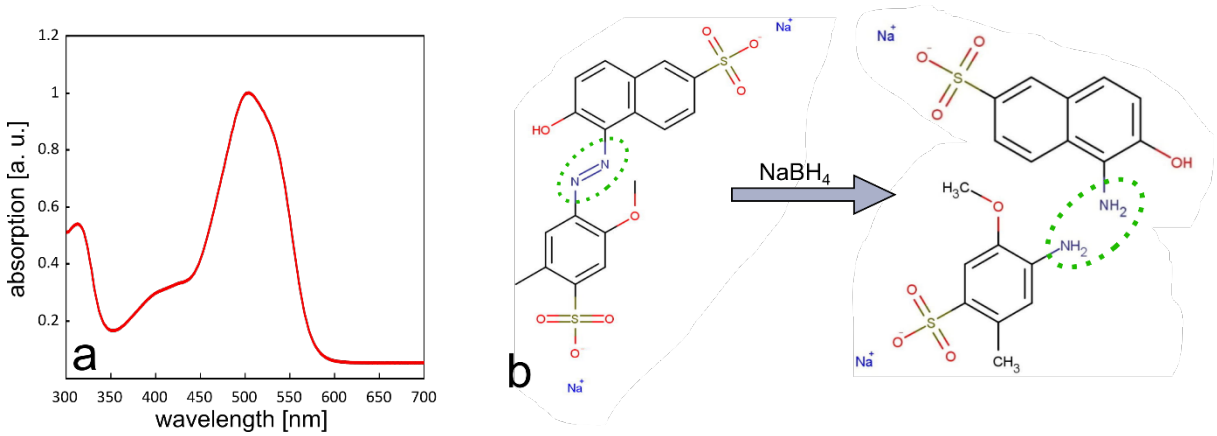

***Figure 16**. a) Normalized optical absorption spectrum of the Allura Red dye. b) Catalytic decomposition of Allura Red with $NaBH_4$ into 2-methoxy-5-methyl-aniline-4-sulfonic acid and 1-amino-2-naphthol-6-sulfonic acid on an Au catalyst[61] (structures adapted from same source).*

Allura Red decomposition is a reaction that, for example, has been investigated for sewage treatment purposes since dyes of the azo group are known to be toxic and carcinogenic in large quantities and persist for a long time in the environment[61–66]. Mechanistically, the

decomposition of Allura Red can be done via oxidation[62,64] or by reduction[61]. In both cases, it is the name-giving nitrogen double bond (French *azote* = nitrogen) in the center of the molecule that is broken during the reaction according to the following mechanism. The reaction pathway mediated by $NaBH_4$ on Au (**Figure 16b**), starts with the organic dye that is adsorbed onto the gold surface, as it known for other organic dyes such as nitrophenol[63,66,67]. Simultaneously, also the borohydride molecules adsorb on the Au surface and dissociate into hydrogen and hydroborate that goes back into solution[66]. As described for similar reactants[61], the hydrogen from the borohydride will activate the nitrogen double bond in the dye and form NH_2 groups. In this way the double bond is broken and the dye molecule breaks into two organic acids that are colorless an desorb from the Au surface back into in solution[61].

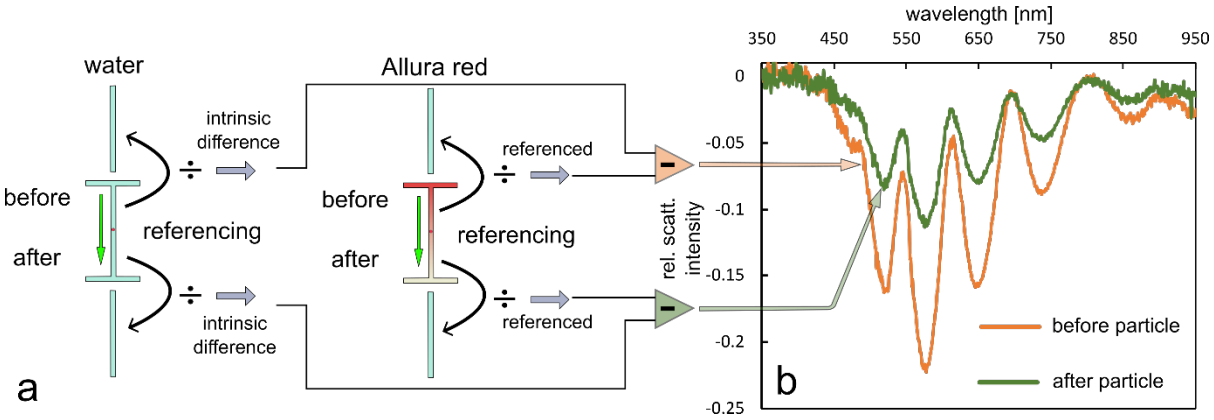

***Figure 17**. a) Evaluation scheme for fluidic systems with reference channels during catalytic Allura red decomposition on Au nanoparticles inside the nanochannels. b) Nanochannel scattering spectra obtained according to the scheme in a) for the decomposition of a 100 mM Allura Red solution by 200 mM $NaBH_4$ on a 100 nm wide and 200 nm long gold nanoparticle inside a single nanochannel. The spectra were measured upstream of the particle (orange) and downstream of it (green). The pressure applied at the inlets with Allura Red was 2 bar. Note the distinct difference between the two spectra, as well as the interference-type modulation of the signal in both of them.*

In view of this reaction mechanism and the colorless product molecules formed, it is clear that this reaction creates a distinct optical contrast and is therefore a perfect test system for the NSS concept in a scenario where this optical contrast is produced within the nanochannel, at the position of the catalyst nanoparticle by the decomposition reaction. Specifically, to define and measure this optical contrast induced by Allura Red decomposition on the Au nanoparticles inside the nanofluidic chip introduced in **Figure 15**, I used the evaluation scheme depicted in **Figure 17a** based on the on-chip referencing scheme introduced above.

As the main result, we observe a distinct difference in the referenced scattering spectra measured up- and downstream of the particle (**Figure 17b**), with the overall intensity difference (compared to water) decreasing (less negative) after the particle. This is in good agreement with a significant fraction of the dye molecules having been decomposed, therefore rendering the solution more transparent and water-like. On one hand, this was a very encouraging result in the sense that it (i) nicely corroborated my key intentions with this fluidic system, that is, a very stable baseline owing to the continuous referencing with the water-filled reference channels, and (ii) proved that the catalytic reaction is measurable via a change in the scattering spectrum of the nanochannel. On the other hand, it also was disappointing because the spectra

shown in **Figure 17b** are heavily modulated by what appears to be an interference pattern. This masks any distinctive features of the RI spectrum of Allura Red and thus renders any more quantitative analysis of the obtained spectra and their evolution over time essentially impossible. I will discuss the interference problem in more detail in chapter 2.4.2.1.

Despite these interference issues, as a further proof of concept, I executed a second set of experiments using the same fluidic system and the dye Brilliant Blue to further investigate the performance of the on-chip referencing scheme (**Figure 18b**). Note, however, that no catalytic reaction takes place in this case. Instead, to create different optical contrast in the channel, I prepared a series of aqueous Brilliant Blue solutions with 100 mM, 75 mM, 50 mM, 25 mM and 10 mM concentrations, respectively, and flushed them subsequently through the channels to systematically monitor the nanochannel scattering response as a function of dye concentration.

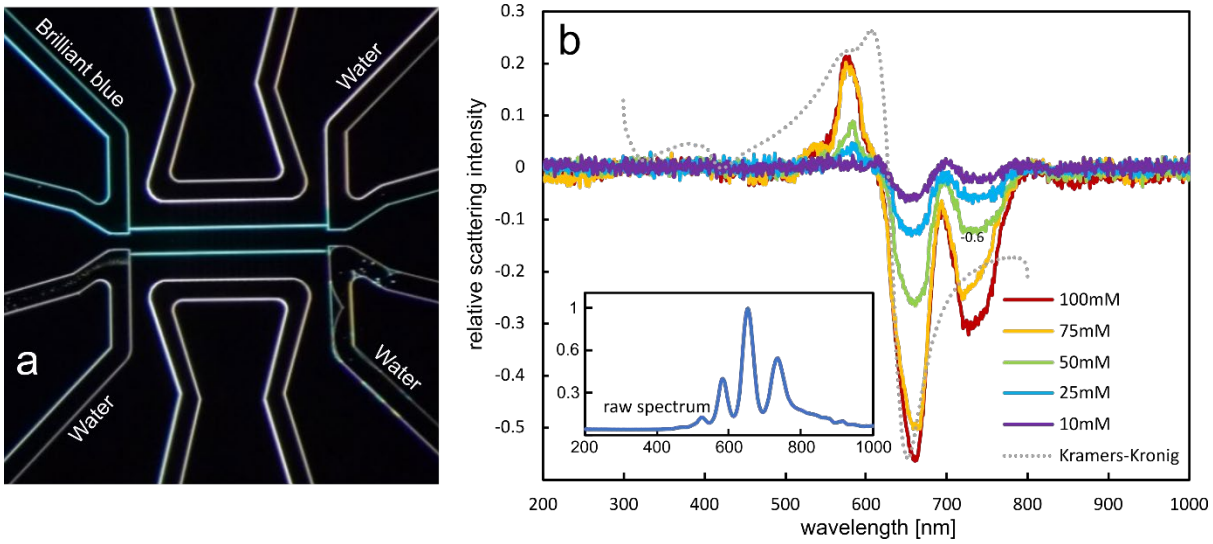

***Figure 18**. a) Dark-field micrograph of the central nanochannel section, where Brilliant Blue is flushed in from the upper left microchannel. A slight blue hue can be seen from the walls of the microchannel as well as from the access channels leading to the nanochannels, which are too dark to see in this picture. d) Referenced scattering spectra of one nanochannel for a concentration series of Brilliant Blue, together with the theoretical RI spectrum as shown in **Figure 14b**. The inset shows the unreferenced raw scattering spectrum from one of the nanochannel sections adjacent to the nanoparticles.*

Looking at **Figure 18b** that depicts referenced scattering spectra for different Brilliant Blue concentrations, the positive effect of the referencing to the water filled reference channels manifests itself in the very flat baseline that shows no offset for any of the measurements. This again corroborates that the reference channels function as intended and significantly improve the obtained scattering spectra from the dye-filled nanochannel. The dependency of the scattering spectrum intensity on the concentration of Brilliant Blue in the solution is also clearly visible as the distinct features diminish with lower concentrations and already here hints at the linear dependence of the scattering intensity on the RI (and thus concentration) of the liquid in the channel that we in detail investigated in the manuscript appended to this thesis.

When comparing the Brilliant Blue scattering spectra that I measured from the nanochannel with the theoretical RI spectrum calculated before, using the Kramers-Kronig relation (**Figure 18b**), we see that the overall similarity is still there, together with some key features. However,

also here the spectra are heavily modulated by interference. This becomes even more apparent when considering how a raw spectrum, prior to referencing, looks like (see inset in **Figure 18b**). At the same time, even if some of the modulation remains, it again demonstrates the value of the on-chip referencing concept since the modulation is substantially reduced. The main reason why it is not eliminated completely is that interference is extremely sensitive to local variations on the chip and varies therefore across different locations on the chip. I will address the origin of this problem in detail below in chapter 2.4.2.1.

2.4.2 Second Stage of refinements

The results that I have obtained so far from the improved experimental setup were encouraging and proved that the made modifications contributed greatly to the overall performance of the NSM and NSS approach. In addition, I was able to show that we indeed can monitor a catalytic reaction on a single particle with a nonfluorescent compound. Unfortunately, however, the interference modulation of the spectra made further quantification of the obtained results impossible and also preclude further use the nanofluidic chips. Accordingly, to resolve the problem in a second stage of refinements, I start out by investigating the origin of the interference patterns in the scattering spectra.

2.4.2.1 Eliminating interference

Looking at the spectra shown in **Figure 17b and Figure 18b**, the fringe pattern appears quite regular and the width of the interference peaks increased slightly for longer wavelengths. This sparked the idea that I was dealing with a basic physical phenomenon. After some investigation, it became apparent that this indeed was the case since the fringe pattern visible in the scattering spectra is the result of thin film interference. More specifically, the interference is generated when the incident light is reflected not only from the surface of the oxide into which the nanochannels are fabricated, but also from the surface of the silicon under the oxide, as depicted in **Figure 19b**. To corroborate this hypothesis, I calculated this interference following Gungor et. al.[68], using 3.88 as the RI of silicon[69] and neglecting its extinction. The result can be seen in **Figure 19c**, where I used 2 µm as the nominal thickness of the oxide that is on the silicon wafer and in which the nanofluidic system is embedded. This theoretically obtained fringe pattern matches quite well with the experimental data, even though the peaks match not exactly since the actual oxide thickness on my sample might be slightly different from the targeted 2 µm. That the calculation yields the same number of interference peaks within the spectral range of the light source and that the peak width increases for longer wavelengths further corroborates my assumption that thin film interference distorts the scattering spectra of the nanochannels in the current chip design, due to the unfortunate choice of a 2 µm thick oxide layer on the silicon wafers used for the fabrication of the chip.

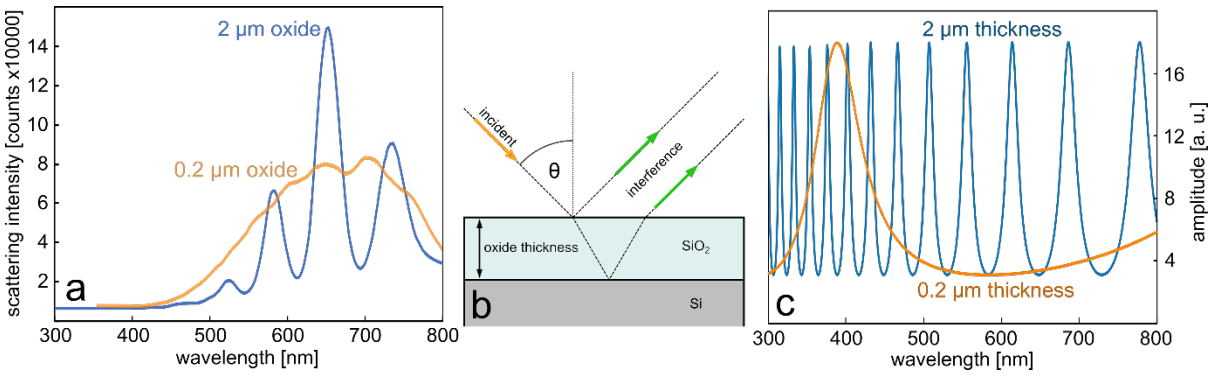

***Figure 19**. a) Nanochannel scattering spectra for a water-filled nanochannel etched into 2 µm thick SiO_2 (blue line) and etched into 0.2 µm SiO_2 (orange line). In both cases the typical interference fringe pattern can be seen. However, it is dramatically reduced when 0.2 µm SiO_2 is used to host the nanochannel. b) Schematic depiction of the principle of thin film interference. c) Calculated fringe patterns for SiO_2 layers of 2 µm and 200 nm thickness.*

To amend this interference problem, it is now apparent that yet a new generation of nanofluidic chips need to be produced, using a silicon wafer with a thinner oxide layer as the substrate. Specifically, based on the calculations depicted in **Figure 19**, we opted for 200 nm oxide thickness, since this would minimize interference while at the same time leaving enough material to etch the 150 nm deep nanochannels. This new generation of nanofluidic chips also had additional features that I will explain in detail in chapter 2.4.2.2.

2.4.2.2 Upgrading the chip design to mitigate nanochannel clogging

While obviously being disappointing, I saw the necessity of fabricating a new generation of chips to mitigate the interference issue also as an opportunity to further modify and improve the fluidic design and add features that could be helpful when a chip is to be used for a longer time across many measurements and liquid exchanges. To motivate the added features I describe below, it is important to first discuss the main reason that a chip needs to be decommissioned and cannot be used for further experiments. This reason is that the nanochannels eventually get clogged by small debris particles that I have observed to be flushed into the system while handling the chip, the chuck, the pressure system and the syringes that I used to exchange the liquids. In fact, this "debris particle problem" can already be seen in the overview dark-field image in **Figure 18a**, where particles have accumulated in certain positions of the microchannels.

Since the exact origin(s) of these particles was unclear (and since they likely stem from different sources) we decided that instead of trying to avoid them completely, we would attempt to build a smart fluidic system that would prevent the particles from being flushed into the nanochannels. Specifically, I had discovered interesting solutions to similar challenges that are used within biological sciences[70–76]. Specifically, microfluidics systems used in this field often are equipped with solutions for different kinds of bacteria, cells or other biological particles that need to be sorted or separated. Since a high throughput is desired in these operations, they typically comprise microfabricated mechanical filters with pillar-like structures[72] or exploit the principle of hydrodynamic focusing. A detailed account of this principle would exceed the scope of this thesis but, in short, it is based on the behavior of particles in curved flows in confined fluidics. Depending on various parameters, such as fluid viscosity, flow speed and

particle size, the particles tend to accumulate at certain positions in the microchannel and can thereby be filtered out.

Inspired by one relatively simple system for hydrodynamic focusing that was presented by Gou et. al. I designed a meandering structure (**see Figure 20b**) in the inlet microchannels of my new chip that served the purpose of concentrating any larger particles in the middle of the liquid stream through the channel. Since a specifically designed and optimized microfluidic system for hydrodynamic focusing would have required in-depth knowledge of the fluid dynamics of the system and, most importantly (and impossible to get), details about the particles to be filtered, I estimated a "reasonable" geometry for the meandering structure where I made sure that it would mean no harm to the rest of the fluidic system if the hydrodynamic focusing would not work. Furthermore, I found it interesting and relevant to implement into the new design as proof of concept that highlights the fantastic opportunities provide by micro- and nanofluidics.

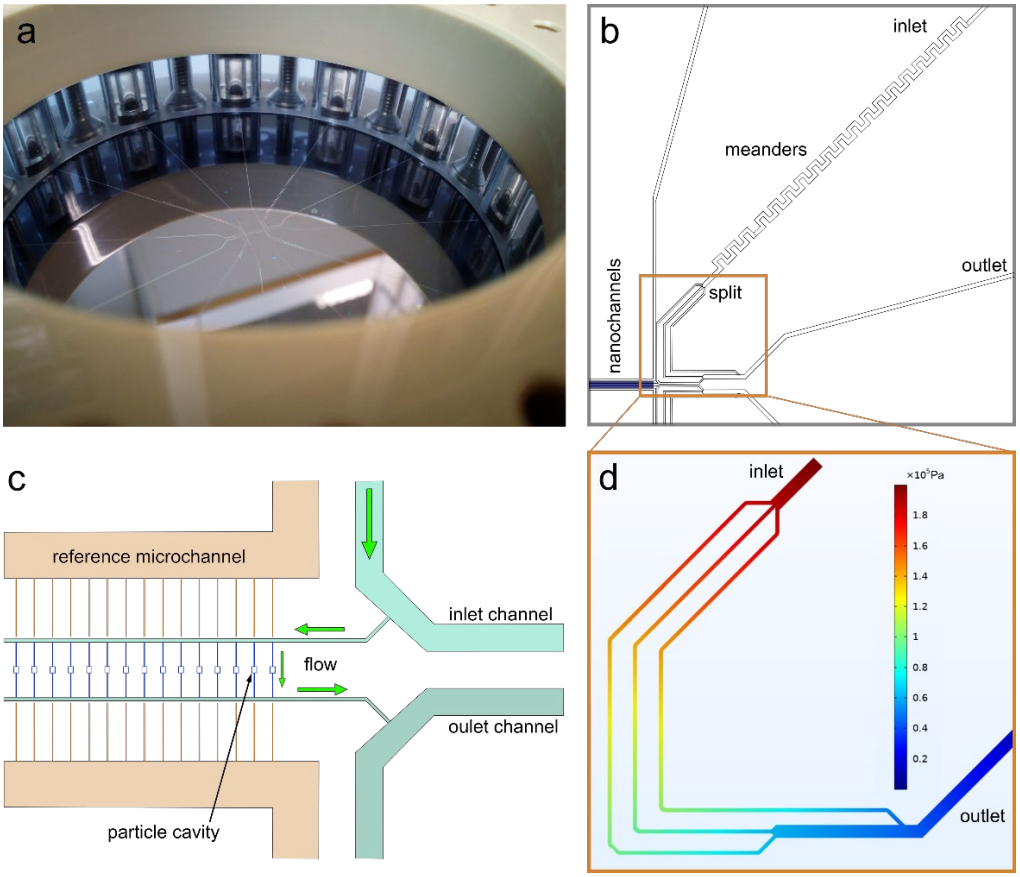

Figure 20. *a) Photograph of a nanofluidic wafer mounted in the chuck. The microchannel system is visible as brighter lines, leading from the reservoirs to the nanochannel area. The glass tubes connecting to the reservoirs are visible in the transparent perimeter of the chuck. b) Schematic overview of the redesigned microfluidic system of the new chip design. The rectangular meanders in the inlet channel are to focus the small "debris" particles in the liquid to the center of the flow, such that they are transported into the middle channel of the three-way split after the meander, and thereby are removed from the rest of the liquid further flowing towards the nanofluidic system. Accordingly, the access channels to the nanochannels are connected to the smaller left microchannel (labeled as inlet channel in c) of the three-way-split, where no particles should be present.*

*c) Drawing of the reaction nanochannel system, together with the reference nanochannels and in- and outlet microchannels adopted from the previous chip design (**cf.Figure 15**). The only difference is that the areas of the nanofluidic system that host Au nanoparticles have been extended and that there is now a total of 135 nanochannels in the system (see text for details). d) Comsol simulation of the split microchannel area that connects to the meanders that reveals the pressure gradient in the branched channels when the inlet is pressurized with 2 bar. As the key point, we see that it is very similar in all three split channels, which should guarantee a similar flow speed in the split channels and therefore an undisturbed separation of the particles from the rest of the liquid.*

The main idea behind my design is that the particles will stay closer to the inner radius of every curve of the meander when flowing around a corner according to a similar design by Gou et. al.[75] When exiting the meander-structure the particles would thereby be focused in the middle of the microchannel. Hence, if they at this point encounter a three-way junction that splits the microchannel, the center channel at the split would capture the particles and thus separate them from the liquid that is flushed towards the nanofluidic system via one of the other microchannels at the split. Corresponding Comsol Multiphysics simulations of the flow and pressure drop across the three microchannels after the split are depicted in **Figure 20d.** As the key point, they show that the pressure drop in all three split channels is identical, so that the flow speed is so as well, thereby enabling an undisturbed splitting and separation of the debris particles.

In addition to the meander system to mitigate clogging by dirt particles, the new chip generation also featured 135 nanochannels, where each channel was equipped with different particle constellations of Au and as a second metal also Pd. The particle(s) in sets of 1, 10 or 100 were placed in small cavities which were all 5.6 µm long and had three different widths of 0.4 µm, 0.7µm and 4 µm. The cavities served the purpose of prolonging the residence time of reactants close to the particle to increase conversion and thereby – hopefully – scattering contrast. In addition to the channels filled with particles the chip also features 45 empty nanochannels that would serve as negative controls.

2.4.2.3 Automatization of data acquisition

The large number of differently decorated nanochannels in terms of number and type of nanoparticles on my new chip design and my ambition to monitor up to 135 nanochannels in a single experiment made it clear that manual switching of pressures applied to the fluidic systems to redirect flow and of spectrometer settings would be challenging. Hence, I decided to write a LabView program that would carry out the measurements automatically. Furthermore, remote control enables more precise control of applied pressure and chip position on the microscope via the motorized stage and therefore creates more reproducible conditions between measurements.

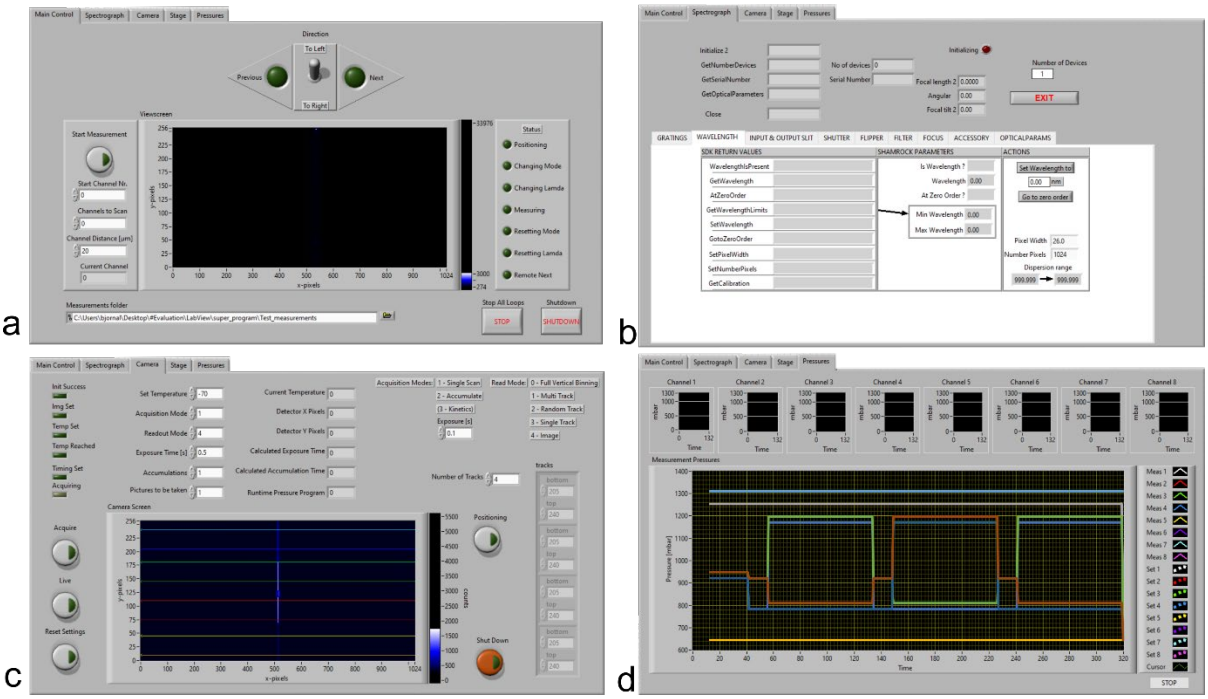

***Figure 21**. User interfaces for the LabView program that was written for the automatization of NSS measurements on a large number of parallel nanochannels. a) Main control interface, with settings for the number of channels to be measured, the distance between the channels and a control panel that shows the current step in the measurement, together with a screen showing the current camera image. b) Spectrometer interface, with settings for the grating/mirror. c) Camera interface with acquisition settings and the areas for recording the upper reference channel, the up- and downstream section of the reaction channel hosting the particle(s). d) Pressure control window, which would display the current applied pressure levels for each of the eight inlets.*

The program itself is structured into four parts, each being responsible for one connected instrument and each having its own user interface: (i) spectrograph, (ii) camera, (iii) pressure control, and (iv) microscope stage (**Figure 21**). To illustrate which steps were needed to record one complete data set from one nanochannel, I will give a short description in chronological order.

0. Setting up the microscope, connecting all required parts on the hardware and software level, filling the reservoirs with the respective solutions, and moving the first channel into position and focus, checking the camera acquisition settings and then starting the measurement in the software.

1. The program will first correct the position of the nanochannel in the field of view of the camera and regarding the slit of the spectrograph by detecting its vertical ends and the horizontal position of the center of the nanochannel image.

2. The spectrograph changes from the mirror to the grating with 150 l/mm, setting a predetermined center wavelength which was typically 642 nm.

3. Water is flushed through the nanochannels by applying pressure at the inlet of the microchannels that are connected the water-filled reservoir via the Fluidgent device.

Thereafter, the scattering intensity spectra of all four channel sections (upper and lower reference channel, Up- and downstream sections of the reaction channel) will be recorded and binned, such that each section has one scattering spectrum recorded. The spectra obtained at this stage, where all channels are filled with water, are needed to calibrate the reference for the later evaluation.

4. Now the reactants (Allura Red with $NaBH_4$ in water or H_2O_2 in water) were flushed in by applying a pressure of 2 bar to the inlet that contained the corresponding solution via the Fluidgent device, while the recording of the spectra continued. Depending on which flow situation was desired in the micro and nanofluidic system, all inlet and outlet pressures could be varied between 10 mbar and 7 bar.
5. The pressures were switched again, such that water was again flushed through the nanochannels from the water inlet via the respective microchannel. This step is included to clean the channels from reactants and to provide a comparison to step 3, as the situation should now be identical to the start.
6. Having completed one set of measurements for one channel, the grating in the spectrograph is replaced by the mirror, so that the image of the channel becomes visible again.
7. The stage is moved by the distance between channels, such that the next channel can be automatically positioned, and the process starts again at step 1 to acquire data from the next channel in the exact same manner.

Even tough designed for spectrally resolved NSS measurements from single nanochannels, given the accurate control over the setup the program provides, it can easily be modified to omit the spectral information and only record scattering intensity. The use and implementation of this automatization software did not only make all measurements comparable since the pressures and time steps were the same, but it also made the recording of larger and more diverse datasets possible, as it was the intention with the new chip design with 135 nanochannels of different configurations.

2.4.2.4 Nanoparticle catalysis – Allura Red and H_2O_2 on Au and Pd

As the first experiment with the latest generation of chips and the automated setup, I aimed at reproducing my previous results on degradation of Allura Red on Au nanoparticles (**cf. Figure 17**). For this purpose, I again prepared a 100 mM solution of the dye and mixed it with a 200 mM solution of $NaBH_4$. This mixed solution was subsequently pipetted into one reservoir connected to a microchannel inlet. Monitoring the scattering spectrum of a nanochannel with a 5.6 x 4 µm cavity and an arrangement of 100 gold particles with 50 nm diameter localized in the cavity produced the result shown in **Figure 22a** for three subsequent measurements, where the procedure described above was repeated for three times for the same channel.

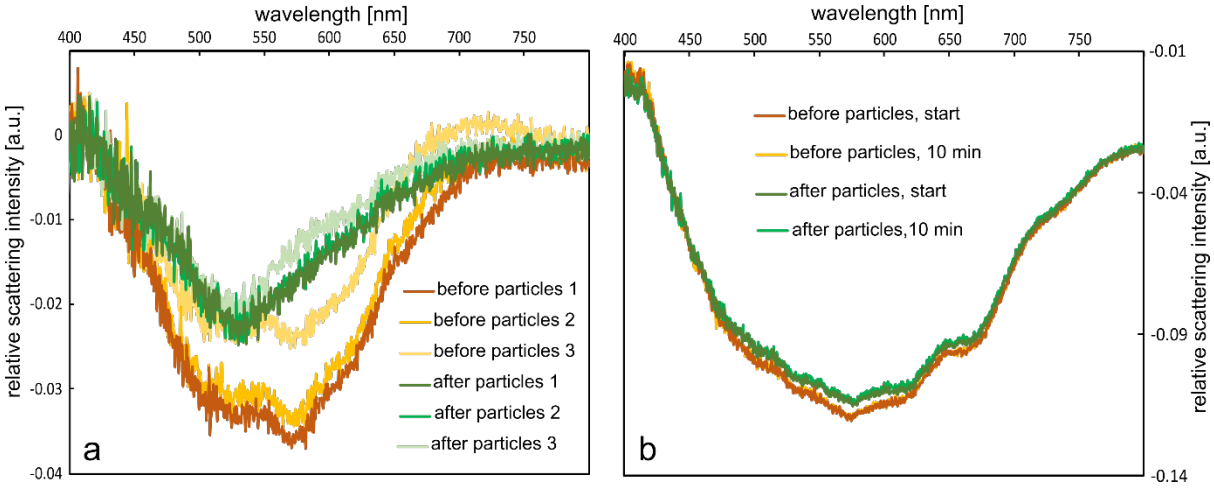

***Figure 22**. Referenced scattering intensity difference spectra for three subsequent measurements of catalytic decomposition of a 100 mM Allura Red solution by 200 mM $NaBH_4$ over hundred 50 nm Au nanoparticles in a nanofluidic channel. b) Referenced scattering intensity difference spectra acquired during the catalytic decomposition of 15 % H_2O_2 in water over hundred 50 nm Pd nanoparticles inside a nanofluidic channel.*

The improvement regarding the interference fringe pattern is evident, since it is essentially not noticeable in the spectra anymore. Consequently, the shape of the spectrum now also resembles more clearly the RI spectrum of Allura Red[60] with the broad double peak between 500 nm and 600 nm that is connected to the decrease of the absorption in this range (**see Figure 16a**). The reduced referenced scattering intensity difference downstream of the catalyst is again also clearly visible and indicates that the catalyst is decomposing the dye. The most prominent spectral feature that can be seen is that the peak at 575 nm has vanished in the downstream spectra. However, the downstream spectra still exhibit a distinctive peak at 530 nm, which could be indicative of an incomplete decomposition or that other products than those shown in **Figure 16b** have formed[77]. Finally, it is also interesting to see that the upstream scattering spectrum decreases over time during the three consecutive measurements, which could indicate that the dye degradation also takes place directly in solution, however at a much lower rate than on the Au catalyst. Therefore, as an intermediate summary, I was able to reproduce my previous results with Allura Red but this time without fringes, which significantly increased the level of detail that can be seen in the spectra.

Since in this latest chip design, I had decorated 50 % of the nanofluidic system with Pd particles to have a second catalyst at hand to also investigate a color-less reaction, I prepared a new

experiment using the catalytic decomposition of H_2O_2 on Pd as the model reaction. This reaction is quite well investigated[1,2,78–82] for various catalysts, and water and molecular oxygen are the products of the decomposition reaction. The correspondingly obtained result when flushing a 15% aqueous H_2O_2 solution over 100 Palladium particles with 50 nm diameter and in a cavity of the nanochannel that had the same size as for the Allura Red experiment discussed above is summarized in **Figure 22b**. As the key result, we see more or less featureless referenced scattering intensity difference spectra, in agreement with the lack of absorption bands of the reactants. As the second key observation I notice that, compared to the Allura Red case, the difference between up- and downstream spectra is very small. This either means that the sensitivity towards reaction induced RI changes in a colorless reaction is very small (which we from theory know is not the case) or that the catalytic activity of the Pd nanoparticles in the nanochannels is very low. To ensure that the small observed difference between the up- and downstream particles was not simply an artefact, we can compare the first measured spectrum with a spectrum obtained after running the reaction for 10 min. Clearly, we see that we essentially obtain the same result. This not only indicates that the measured difference likely is caused by the reaction but also highlights the excellent long-term stability of the setup thanks to all the made improvements and the on-chip referencing.

Before further investigating the – surprisingly – low activity of the Pd nanoparticles nanofabricated into the nanofluidic channels in chapter 2.6 below, I need to again comment on the clogging problem imposed by debris particles. Unfortunately, it turned out that despite the taken countermeasures with the meandering microchannels not all debris particles are captured and removed from the liquid stream that reaches the nanochannels. Therefore, also this latest chip generation clogged up after very few measurements only, which means that no repeated measurements necessary for generating statistically relevant data are possible. As a consequence, I also completely abandoned this type of fluidic chips and samples (for now), despite the highly promising preliminary results obtained, and the significant amount of time invested. The main reason for this decision is the fact that upon a detailed investigation of the origin of the debris particles summarized in chapter 2.5 below, it became obvious that a radically different design was necessary to resolve the problem.

2.5 Fluidic system clogging by debris particles

The problem of debris particles has been present already in the very first chips with water reference channels that I have used. For example, small amounts of these particles can be seen in the corners of the microfluidic channels in **Figure 18a**. As a key characteristic of this problem, the amount of debris in a fluidic system could vary over time from single small particles being flushed through the microchannels up to massive amounts that reminded of a snow storm, as shown in **Figure 23**. The origin of those particles was unclear for a long time, since I was dedicated to keep all solutions clean and used only Milli-Q water in the experiments. At the same time, any actively taken countermeasures, such as filters in front of the syringes, exchange of O-rings in the chuck from NBR to more chemically resistant FFKM or hydrodynamic focusing in the last generation of chips proved ineffective in the end. Furthermore, it also turned out to be impossible to completely remove particles from clogged channels by reversed long term flushing. In other words, the fluidic systems became unusable rather rapidly and irreversibly.

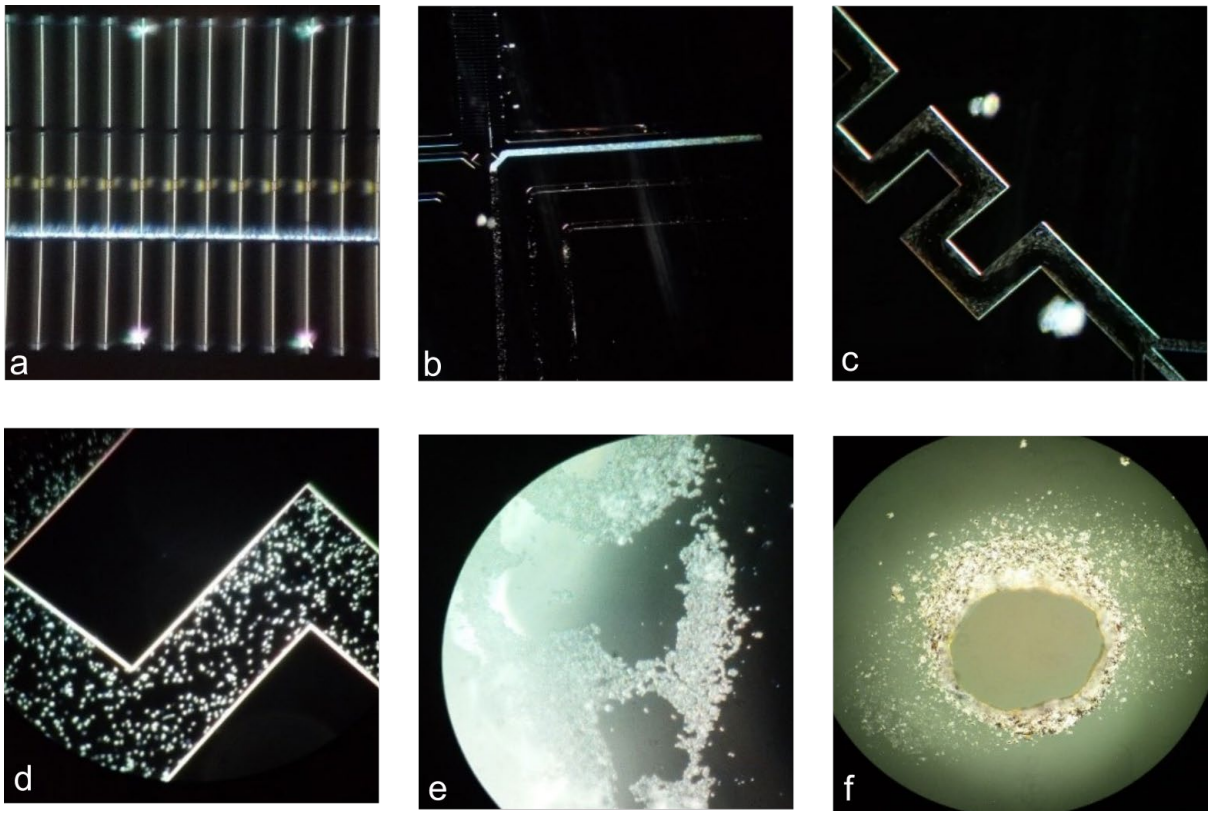

***Figure 23**. Debris particles as observed at various positions within the fluidic system in optical microscopy images. a) Debris particles in an access microchannel connecting to the array of reaction nanochannels. b) Debris particles in a microchannel. c) Debris particles in a meander channel under flow and d) at stagnant conditions. e) Debris particles accumulated at the bottom of the inlet hole. e) Bright-field optical microscope image of the sandblasted inlet hole in the glass lid that reveals its rough and cracked surface.*

Ultimately, after a detailed and systematic search for the origin of the debris particles, what remained were the sandblasted inlet holes in the glass lid that connect the reservoirs on the chip to the inlet system of the chuck. Corresponding SEM images I took from the hole area revealed that the walls of the cylindrical hole had a very rough structure (**Figure 24f and Figure 24a**). Furthermore SEM images of debris particles extracted from a chip revealed a structure reminiscent of shattered amorphous material (**Figure 24b,c**) with various shapes and sizes, where the smallest particles were in the size range of 100 nm to 200 nm (**Figure 24c**). Furthermore, I had observed that the largest number of particles occurred after a chip had not been used for a while, indicating that the debris had accumulated over time in the inlet holes.

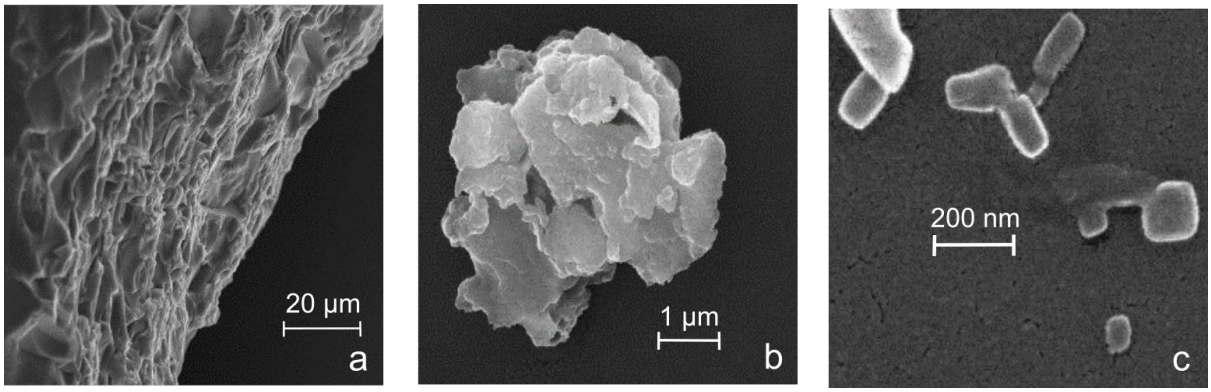

***Figure 24**. a) SEM image of the side wall of an inlet hole that was sandblasted through the Borofloat 33 cover glass used to seal the chip. b) and c) are SEM images of examples of particles found in the inlet holes.*

As a last aspect of relevance, I want to note that the behavior of the particles in the meanders was not of the kind expected for freely floating particles since they tended to accumulate where the flow speed was lowest rather than being focused in the center of the flow (**see Figure 23c**). This thus also hints at that these particles are heavy and in general behaved like "grit" in their tendency to accumulate in regions of low flow speed.

All this collected evidence thus leads to the conclusion that the origin of the debris particles most likely is the inlet holes in glass lid bonded onto the chip. This becomes particularly probable by the fact that this problem did not occur in my very first measurements, where I use the triangular chips (**Figure 9d**), in which the access holes were chemically etched though the silicon on the back side of the chip, rather than sandblasted through the glass. Since sandblasting is the only method we have at hand to drill small holes into glass, the only way to avoid the debris problem is to abandon the sophisticated chip design I have developed and return to simpler designs that enable access to the fluidic system from the silicon side of the wafer. This is what I have done in the part of my work that is described in detail in the appended manuscript and briefly summarized in chapter 3 below.

2.6 Investigating low Pd nanoparticle catalytic activity

Pd is a generally widely established catalyst for the decomposition of H_2O_2[1,80,81,83]. The more surprising was the apparently low activity of our nanofabricated Pd nanoparticles. To further investigate this issue, we nanofabricated arrays of Pd nanoparticles with sizes ranging from 10 nm to 100 nm on an open oxidized Si wafer surface using the same electron-beam nanofabrication recipe as used for the nanofluidic chips. In a first step, I cleaned the sample in a reducing 200 mM $NaBH_4$ solution to remove possible oxide. Subsequently, I immersed the sample in a 15% H_2O_2 solution by adding a drop on the surface (**Figure 25a**). After 5 minutes the formation of O_2 bubbles could be observed (**Figure 25b**). However, a more detailed analysis using dark-field scattering microscopy revealed that the bubbles were not forming at the positions of the Pd nanoparticle arrays but instead at the Pd number labels nanofabricated next to the nanoparticle arrays for their identification (**Figure 25d**).

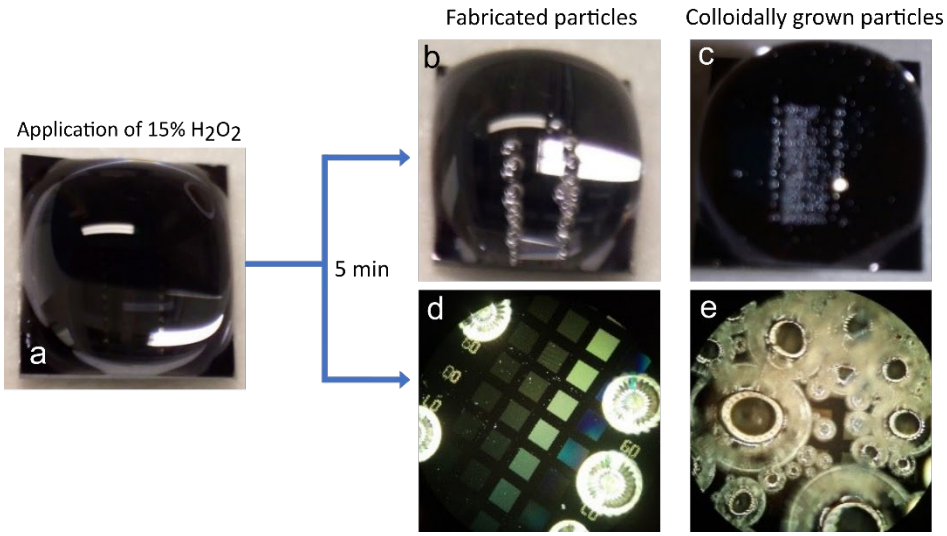

***Figure 25**. H_2O_2 decomposition reactivity tests of nanofabricated vs. colloidally grown Pd nanoparticles. a) A drop of 15% aqueous H_2O_2 solution is applied to an oxidized silicon wafer surface decorated with electron beam lithography nanofabricated arrays of Pd particles with different size. b) After 5 min incubation, the formation of O_2 bubbles is seen on a few areas of the sample. c) For a similar sample where the particles were grown in colloidal solution, a much more intense and evenly distributed O_2 bubble development is apparent. d) Dark-field microscopy reveals that bubble formation on the nanofabricated sample only occurs at the numbers labelling the arrays, not at the particle arrays themselves, whereas the colloidally grown particles in e) are highly active and induce intense bubble formation on the entire sample surface.*

This is a very puzzling result, which was further corroborated by repeating the same experiment but on a Si surface decorated with colloidally grown Pd nanoparticles, which indeed exhibited the expected high activity, as manifested in extensive formation of O_2 bubbles when exposed to the 15% H_2O_2 solution (**Figure 25c,e**). At this point, we do not understand the reason for the low activity of the nanofabricated Pd nanoparticles. We can only speculate that it, for example, may have to do with their structure. For example, it is known that (100) and (111) surfaces are important for high activity[1], which means that the low activity of our nanofabricated particles could be related to a lack of such surfaces. An alternative explanation is that residues from

nanofabrication, such as polymers used as evaporation masks, contaminate and deactivate the nanoparticle surface. As a consequence, in the last stage of my work that is described in the manuscript appended to this thesis and briefly summarized below, I have worked with colloidal Pt nanoparticles to overcome the unresolved activity problem of nanofabricated particles in the H_2O_2 decomposition reaction.

3 A new start

After the successful proofs of principle and systematic improvements together with the frustrating setbacks with my initial chip designs, it became clear that, to overcome the unresolved problems, I needed a fresh start with differently designed and fabricated fluidic chips and different nanoparticles. For this new start, I decided to focus on the H_2O_2 decomposition reaction due to its relevance in the current discussions about using it as fuel[84,85] and for H_2O_2 fuel cells[86,87]. Furthermore, from the method development perspective, it is the more interesting case since being able to monitor color- and fluorescence-free reactions is the "holy grail" in my field. That said, the demonstrated ability of spectrally resolved nanochannel scattering measurements that offer the potential to determine molecular fingerprints of molecules that exhibit absorption bands in the visible spectral range, is still highly interesting and I intend to pursue it at a later stage (see outlook). Secondly, due to experienced activity issues with nanofabricated particles, I decided to adopt the concept of trapping colloidal nanoparticles inside nanochannels that the group had developed recently[46].

3.1 A simplified chip design optimized for colloidal particle trapping

Inspired by the work of Levin et al.[46] and my encountered challenges with complex chips, we opted for a simplistic chip design only featuring two microchannels with a single set of nanochannels in between (**Figure 26**). This had the further key advantage that the connection to the inlet reservoirs was possible to etch chemically from the silicon side, thereby eliminating the debris particle problem. The dimensions of the nanochannels were chosen as before i.e., 150 nm x 150 nm cross section and a total length of 340 µm, whereof 170 µm would be visible in the field of view of the camera. As the key new feature that distinguishes them from all other designs presented in this thesis, they had a nanofabricated constriction in the center of each nanochannel (**Figure 27**). This constriction is designed to function as a physical trap for colloidal nanoparticles flushed through the nanochannel and corresponds to a 1 µm long section of the nanochannel along which the free height is reduced to 30 nm. Hence, any object larger than 30 nm cannot pass and will get trapped, while liquid flow through the nanochannel still is possible.

To work with these chips, since they featured the inlet holes on their backside, I had to use an inverted microscope to avoid the gravitation-induced leaking of liquid out of the chip. Specifically, I used a Zeiss Axio Observer Z1 inverted microscope, equipped with the same Thorlabs Solis 3C LED lamp that I had used before. The camera on this setup was a Andor iXon Ultra 888 EMCCD, which had the option to increase the sensitivity by activating an electron multiplier (EM) in front of the CCD chip. The chuck used for mounting the samples was similar to the one I used during my very first experiments (cf. **Figure 9d**) but had the additional feature that all four reservoirs could be accessed while the chip was mounted in the

chuck. This improved the workflow immensely since I did not have to unmount the chip for each exchange or refill of liquid.

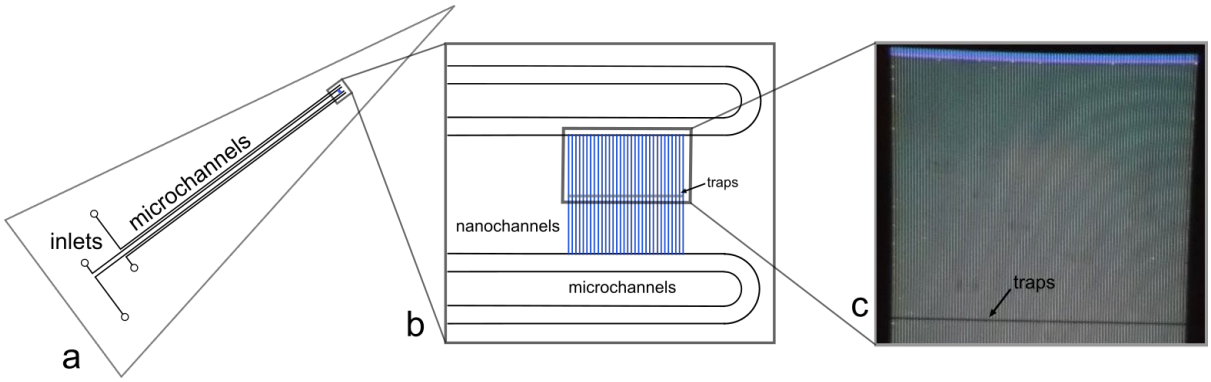

***Figure 26**. a) Schematic of the microfluidic in- and outlet system on the chip, designed for the trapping of colloidal particles. It is comprised of a parallel in- and outlet channel that connects to the set of nanofluidic channels on one end and to the inlet reservoirs on the other. The sketch is drawn with correct proportions. b) Schematic of the nanochannel region with the constriction traps in the middle of the nanochannels and the connections to the microchannels. c) Dark field scattering microscope image of the nanochannel set with 84 parallel channels in the field of view at 50 x magnification. Note the trap regions' darker appearance due to its reduced scattering intensity caused by the smaller channel dimensions at the constriction.*

3.2 Trapping colloidal Pt nanoparticles in nanochannels

As catalyst particles, I chose spherical Pt colloids with a nominal diameter of 70 nm comprised of small crystallites in the few nm size range (nanoComposix, PTCB70-10M, BioPure Platinum Nanoparticles – Bare (Citrate), 70 nm; **Figure 27c**). Pt is reported as an excellent catalyst for H_2O_2 decomposition, in par with or even exceeding Pd in terms of activity[81]. **Figure 27b,d** show SEM images of a single and multiple such Pt nanoparticle(s) captured by a nanochannel trap. These images were obtained from a special type of chip developed by Levin et al.[46], where the lid is reversibly attached using polysilsesquioxane (PSQ) to enable its reopening after particle trapping to enable the verification of trapped particles by electron microscopy.

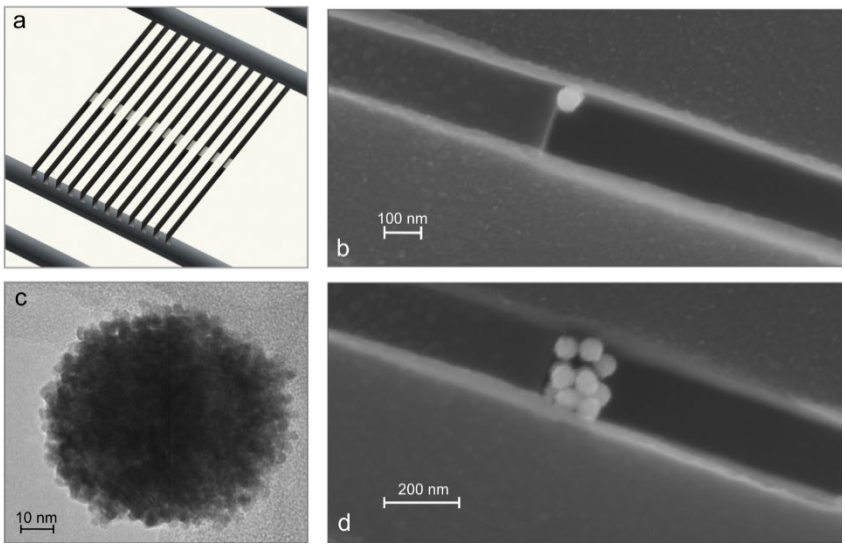

Figure 27. a) Artist's rendition of nanochannels with vertical constrictions in the center that serve as traps for colloidal nanoparticles flushed through the channels. b) SEM image of a constriction with a single trapped colloidal Pt particle. The image was enabled by using polysilsesquioxane (PSQ) to reversibly bond the lid to the chip, which enabled the reopening of the chip after particle trapping and thus imaging of the trap region. d) TEM image of a Pt particle. Note the very structured surface due to the particle being comprised of small crystallites in the few nm size range. d) SEM image of a trap at which 8-9 Pt particles have accumulated.

Since the re-openable chips with PSQ-bonded lids cannot be used for catalysis experiments due to leaking between nanochannels, I had to find an alternative way to verify and count Pt particle(s) trapped in each channel. This is of particular importance since we (i) aim at true single particle experiments and (ii) need to know the number of particles in each channel to be able to ultimately derive accurate reaction turnover frequencies. A particular complicating factor in this respect is that Pt nanoparticles are very weak scatterers, which, compared to Au, makes it impossible to directly see them in a dark field scattering image[88]. Interestingly, however, as discussed in detail in the appended manuscript, localizing the optically dark Pt nanoparticles inside nanofluidic channels makes them distinctly visible as dark spots with appropriate image post-processing (**Figure 28a-c**).

The first method that I have developed to see "dark" particles in the channels is by taking a reference picture of the empty channel system and subtracting it from the subsequent series of pictures in the trapping experiment. (**Figure 28a,b**). This method is straightforward, but it requires a very stable setup such that the reference picture remains valid for the entire experiment. The second method that does not require an empty channel reference is based on the fact that the nanochannels form a regular periodic pattern. Hence, by using a fast Fourier transform (FFT) bandpass filter and thereby eliminating the frequency belonging to the channel pattern from the picture, the particles appear as distinct dark spots since they do not periodically occur in the scattering images (**Figure 28c**). The drawback with the FFT approach is the relatively slow and computationally costly Fourier transformation. Hence, I have used the referencing method in my experiments.

With a method at hand to resolve single Pt nanoparticles inside my nanochannels, the next step was to find a way to quantitatively count them to know how many of them that would be

captured by each trap and thereby being able to optimize the trapping procedure towards as many single nanoparticles in each nanochannel as possible. In principle, there are two possibilities to do this. The first one relies on the fact that the particles are subject to Brownian motion, which means they will move randomly in front of the trap, provided no convective flow presses them against the trap. By simply monitoring the motion of the particles over time, I can count the number of particle peaks in the scattering trace along the nanochannel (**Figure 28d**). While in principle straightforward, this method requires that no particle gets stuck at the trap because it otherwise will not be counted. The alternative way to count trapped particles is to monitor the scattering intensity at the trap area of the channel since any Pt particle arriving there will reduce the scattering intensity in a stepwise manner (**Figure 28e**).

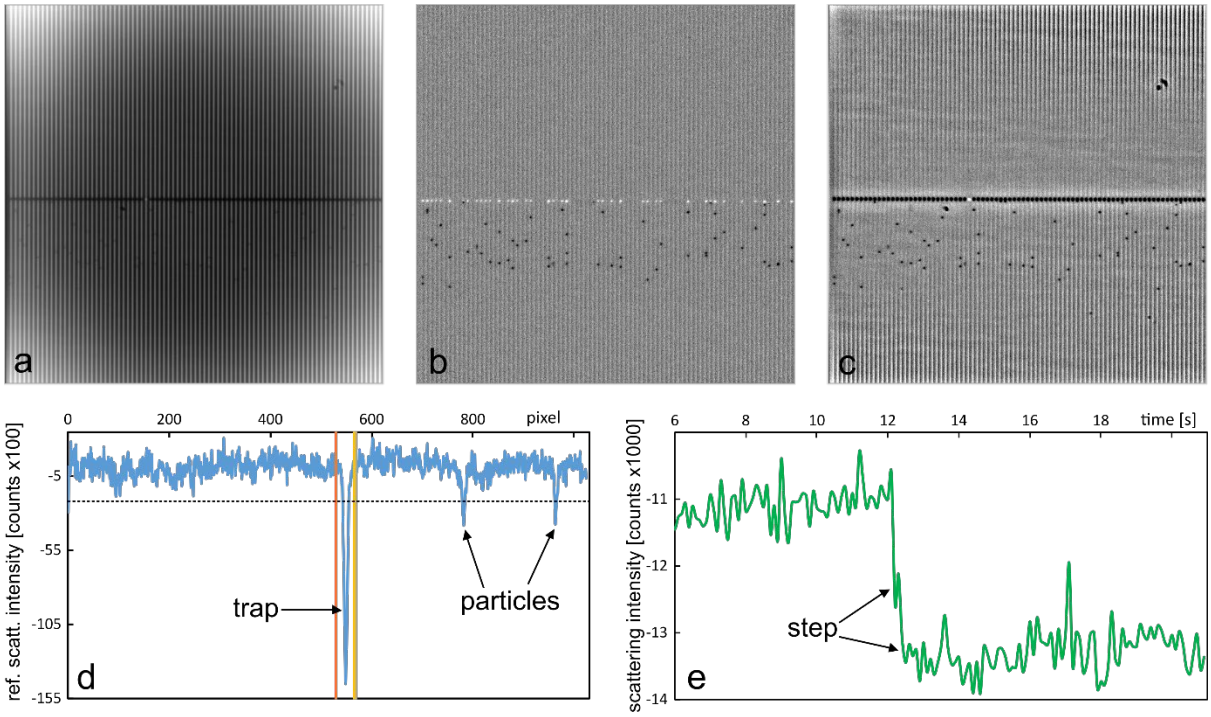

***Figure 28**. Single Pt colloidal particle detection and counting. a) Raw dark-field micrograph of an empty nanofluidic system. The dark line in the middle stems from the traps and the radial intensity gradient is the consequence of uneven illumination of the sample. b) Differential image obtained by subtracting an image of empty channels when the particles were pressed towards the trap by convective flow through the channel from an image where Pt particles are randomly diffusing inside the channel in absence of flow. This procedure reveals the particles as dark spots. Note that the white spots at the traps mark positions at which the particles were localized in the reference image. c) FFT version of the same image as in b). FFT reveals the particles since they are not part of the regular nanochannel pattern. d) Counting of freely diffusing particles by detecting their (negative) scattering signal along the nanochannel. e) Counting of nanoparticles at the trap by monitoring the change of the scattering intensity at the trap area over time. The arrival of a particle at the trap causes a steplike decrease in the scattering intensity.*

3.3 Summary of the appended manuscript

Equipped with the tools summarized above, I set out to study the catalytic decomposition of H_2O_2 on single trapped Pt colloidal particles and investigate the impact of two different types of ligands. This is the essence of the work described in the manuscript attached to this thesis. In summary, in this work I introduce the nanofluidic design that combines microchannels with nanochannels that feature a constriction to trap colloidal nanoparticles for nanofluidic scattering microscopy, NSM, of catalytic reactions. After discussing the theoretical background of Mie-scattering as the underlying principle for the scattering-based detection in nanochannels, a linear relation between H_2O_2 concentration in a single nanochannel and the scattered light intensity is established experimentally and verified theoretically. To subsequently demonstrate the potential of concentration measurements in nanochannels based on NSM, we quantitatively assess molecular diffusion of H_2O_2 and demonstrate that the bulk diffusion coefficient can be extracted from NSM measurements. As the next step, we demonstrate the trapping of 70 nm colloidal Pt nanoparticles in the nanochannels, and their counting based of differential imaging. As the final step, we then set out to investigate the H_2O_2 decomposition reaction on single trapped particles. For this purpose, we combine nanochannel scattering readout that informs about H_2O_2 concentration inside the channel, adjacent to the Pt particle during reaction, and the growth rate of O_2 bubbles formed in the channel from the reaction product. In this way, we can derive single particle turnover frequencies at kinetically controlled reaction conditions, as verified by the lack of gradient formation in H_2O_2 concentration in the nanochannel. We find a significant distribution of activity for individual particles which can be traced back to their broad size distribution. Applying this concept to identical Pt particles covered by two different types of ligands, i.e., citrate and Polyvinylpyrrolidone (PVP), we reveal that PVP coated single Pt nanoparticles exhibit a factor 2 lower reaction rate than citrate covered ones, likely due to a combination of larger steric hindrance by the long PVP molecules and their stronger bonding to both Pt terraces and edges. This highlights the impact of surfactant molecules on catalytic reactions and the potential of NSM to unravel them.

4 Summary and Conclusions

In the course of this thesis, I have developed a technique for the investigation of the catalytic activity of single nanoparticles that is based on the scattering of light from nanochannels that contain those particles and confine their reaction products – Nanofluidic Scattering Microscopy, NSM. The underlying physical principle is Mie-scattering from sub-wavelength objects, which connects the scattered intensity of light from a nanochannel to the difference in refractive index (RI) between the fluid in the channel and the surrounding material.

The introduction of a H_2O_2 solution into the nanochannels revealed a decrease in scattering intensity proportional to the refractive index of the solution. This first key result corroborated my theoretical findings that I had derived from Mie theory. Furthermore, I was able to show that compounds that exhibit a specific absorption spectrum in the visible regime, like the dyes Allura Red or Brilliant Blue, give rise to a characteristic scattering spectrum when introduced into the nanochannels that can be described by the Kramers-Kronig relation. This implies that NSM has the potential to be used to (i) identify the concentration of reactants in nanoscale systems via the intensity of the scattered light since it scales approximately linearly with the concentration, and (ii) identify the type of compound in the channel if the scattered light is resolved spectrally in a variant of NSM that we named nanochannels scattering spectroscopy (NSS).

By using catalytic nanoparticles localized inside a nanochannel, I was able to demonstrate the possibility of NSM and NSS to monitor reactions on these nanoparticles by measuring scattered light only. This was done for the degradation of Allura Red over Au nanoparticles by recording the scattering spectra before and after the particle in the direction of flow and identifying the decrease of characteristic peaks in the spectra that signaled the chemical conversion. In addition, I demonstrated that comparing scattered light intensity before and after a particle can be used to monitor its reactivity even when optically transparent reactants are involved. Here, I used the decomposition of H_2O_2 over colloidal Pt particles to show that the nanochannels can confine the reaction product and thereby make it measurable calculate ToFs for single nanoparticles. Furthermore, the application of NSM as method to monitor concentration changes over time inside a nanochannel enabled me to confirm that the reaction was taking place in the kinetically controlled regime since the reactant concentration at the particle position in the channel remained constant over time without developing any gradients. This demonstrates clearly how NSM can be used to assesses the reactivity of single particles directly by measuring the composition of the reactants and products via the intensity of the light scattered from the nanochannel.

Another key achievement was the possibility to detect and count optically dark colloidal nanoparticles via NSM as they were trapped in a nanochannel. This has the potential to pave the way for catalysis on single particles that are smaller than 10 nm and thus invisible in traditional dark field microscopy.

Finally, the development of the experimental setup that I have used for my experiments showed that special nanofluidic designs can help to increase NSM and NSS signal quality and long-term stability by providing an online reference in the form of isolated reference nanochannels.

In addition, the design of parallel nanochannels combined with the possibility of automated measurements enables a high throughput in the characterization of single particle catalysis.

In summary, the overarching and ultimate goal of my project, the assessment of the catalytic activity of single particles below 10 nm in size on the basis of optical microscopy and without the use of fluorescence markers or complex instrumentation, is now within reach and I have the knowledge and understanding that is necessary to make further progress towards this goal on my way to the PhD.

5 Outlook

The development of NSM and NSS for single particle catalysis has sparked a multitude of ideas that could be implemented to improve or extend its functionality. Among those are obviously the unfinished paths of the development where I consider the use of the spectral information to identify the type and concentration of reactants in a nanochannel as the maybe most important and interesting example. Here, studies of the degradation of dyes like Allura Red or Brilliant Blue that I have started but was unable to finish due to the debris problem seem very interesting. For their implementation, new chips that combine on-chip optical referencing with inlet holes etched from the silicon side need to be designed and nanofabricated.

As a second future direction, further developing the method towards studying colorless reactions, but without bubble formation, is very interesting. This will make NSM for single particle catalysis truly versatile by solely relying on the nanochannel scattering intensity approach that enables reactant concentration measurements in the channel. To further boost this approach, the spontaneous batch reactors described in the appended manuscript hint at a very interesting concept, namely, to develop ways to transiently open and close the nanochannels to create batch reactors with trapped single particles inside. The temporal evolution of changes in reactant concentration in this isolated volume can then be tracked via NSM or NSS to determine reactivity of the particle. As the key point, this batch approach would increase the resolution of the method since even slow reactions would with time create a measurable RI contrast. Following the same line, it likely would enable the study of smaller single particles, down to the sub-10 nm size regime, which is the one that is truly technically relevant.

From the perspective of setup modifications, I would like to revisit the reference channel concept, since it clearly improved signal quality and long-term stability by a good margin in my initial proof-of principle measurements. At the same time, the automatization program could be adapted to new measurement schemes to allow a more well-defined, reproducible, and facile acquisition of data.

In terms of the catalyst particle types studied it would be interesting to understand the difference between nanofabricated and colloidal particles in terms of their activity and structure since it is fundamentally interesting, despite having caused a change of direction during the development of this technique so far. One specifically interesting idea could be the colloidal overgrowth of nanoparticles onto nanofabricated seeds that have been placed in the nanochannels. This has been demonstrated on open surfaces[89] and would combine the best of two worlds, i.e., colloidal synthesis and nanofabrication. In this way, it could open new avenues for the investigation of structure-function correlations in catalysis at the single nanoparticle level.

As the final aspect, I want to highlight that it to date is not possible for us to structurally characterize the nanoparticles that are either nanofabricated or trapped inside a nanochannel. In other words, we know only from analogues investigated on open surfaces how they are expected to look like. While this is good enough for proof-of-principle experiments, if true single-particle structure function correlations are to be investigated with NSM and NSS, it is

critical that the particles in the channel can be structurally characterized before and after reaction. I predict that this could be possible by further developing the removable lid approach based on PSQ bonding (**cf. Figure 25**) in combination with SEM. If higher and ideally atomic resolution is targeted, TEM is the method of choice, which means that electron transparent membranes need to be integrated with the nanochannels. This appears to be within reach as nanochannel like devices are already in use in the field of in situ TEM to study materials in the liquid and gas phase[38,90,91].

6 Acknowledgements

I would like to acknowledge the funding provided by the Swedish Research Council and also thank the Knut and Alice Wallenberg Foundation for their support of the infrastructure in the MC2 nanofabrication laboratory at Chalmers.

There are many people that deserve my gratitude and that have provided the necessary assistance that I needed to stay on track but also to stay happy and healthy.

Of all people, it is my main supervisor Christoph that I need to thank, as I would not be in this fortunate situation that I am in now, since you accepted me into your group and gave me the opportunity to develop my ideas and myself as a person. Being now at the end of this licentiate thesis, thank you very much for helping me reach this point.

A big thanks goes out to Joachim, as he provided me with the necessary (fluidic) platform to conduct my research. I would like to see our conversations and regular exchange of chips to be continued.

Thanks to my examiner Henrik who gave me feedback on this thesis and keeping the Chemical Physics division together.

Thanks also to my office mate David for the fruitful discussions about everything and for letting me take care of his plant.

Thank you, Henrik KM for making sure that I returned from that place they call New York.

Thanks to Carl for providing the electron microscopy skills that gave this work an extra touch.

A big thanks in general to the whole Langhammer group and everyone at Chemical Physics for the private and professional discussions at the lunch table and the help provided.

A special thanks to Björn W who inspired me to take on a very interesting and wholesome hobby.

In the end, a big thanks to my family, I am forever in debt to your priceless advice. Thank you for supporting me in my career choices and making it possible to have a place of my own.

7 References

1. Plauck, A., Stangland, E. E., Dumesic, J. A. & Mavrikakis, M. Active sites and mechanisms for H2 O2 decomposition over Pd catalysts. *Proc. Natl. Acad. Sci. U. S. A.* **113**, E1973–E1982 (2016).

2. Serra-Maia, R. *et al.* Mechanism and Kinetics of Hydrogen Peroxide Decomposition on Platinum Nanocatalysts. *ACS Appl. Mater. Interfaces* **10**, 21224–21234 (2018).

3. Gao, W., Hood, Z. D. & Chi, M. Interfaces in Heterogeneous Catalysts: Advancing Mechanistic Understanding through Atomic-Scale Measurements. *Acc. Chem. Res.* **50**, 787–795 (2017).

4. Sambur, J. B. & Chen, P. Approaches to single-nanoparticle catalysis. *Annu. Rev. Phys. Chem.* **65**, 395–422 (2014).

5. Xu, W., Zhang, Y. & Chen, T. *Single particle nanocatalysis: Fundamentals and applications*. *Single Particle Nanocatalysis: Fundamentals and Applications* (2019). doi:10.1002/9783527809721.

6. Zhou, X., Choudhary, E., Andoy, N. M., Zou, N. & Chen, P. Scalable Parallel Screening of Catalyst Activity at the Single-Particle Level and Subdiffraction Resolution. *ACS Catal.* **3**, 1448–1453 (2013).

7. Hansen, T. W. & Wagner, J. B. Catalysts under Controlled Atmospheres in the Transmission Electron Microscope. *ACS Catal.* **4**, 1673–1685 (2014).

8. Hartman, T., Geitenbeek, R. G., Wondergem, C. S., van der Stam, W. & Weckhuysen, B. M. Operando Nanoscale Sensors in Catalysis: All Eyes on Catalyst Particles. *ACS Nano* **14**, 3725–3735 (2020).

9. Hartman, T., Wondergem, C. S., Kumar, N., van den Berg, A. & Weckhuysen, B. M. Surface- and Tip-Enhanced Raman Spectroscopy in Catalysis. *J. Phys. Chem. Lett.* **7**, 1570–1584 (2016).

10. Fam, Y. *et al.* A versatile nanoreactor for complementary in situ X-ray and electron microscopy studies in catalysis and materials science. *J. Synchrotron Radiat.* **26**, 1769–1781 (2019).

11. Hartman, T., Geitenbeek, R. G., Wondergem, C. S., Van Der Stam, W. & Weckhuysen, B. M. Operando Nanoscale Sensors in Catalysis: All Eyes on Catalyst Particles. *ACS Nano* (2020) doi:10.1021/acsnano.9b09834.

12. Meirer, F. & Weckhuysen, B. M. Spatial and temporal exploration of heterogeneous catalysts with synchrotron radiation. *Nat. Rev. Mater.* **3**, 324–340 (2018).

13. Cordes, T. & Blum, S. A. Opportunities and challenges in single-molecule and single-particle fluorescence microscopy for mechanistic studies of chemical reactions. *Nat. Chem.* **5**, 993–999 (2013).

14. Zhou, X. *et al.* Quantitative super-resolution imaging uncovers reactivity patterns on single nanocatalysts. *Nat. Nanotechnol.* **7**, 237–241 (2012).

15. Chen, P. *et al.* Spatiotemporal catalytic dynamics within single nanocatalysts revealed by single-molecule microscopy. *Chem. Soc. Rev.* **43**, 1107–1117 (2014).

16. Andoy, N. M. *et al.* Single-Molecule Catalysis Mapping Quantifies Site-Specific Activity and Uncovers Radial Activity Gradient on Single 2D Nanocrystals. *J. Am. Chem. Soc.* **135**, 1845–1852 (2013).

17. Alekseeva, S., Nedrygailov, I. I. & Langhammer, C. Single Particle Plasmonics for Materials Science and Single Particle Catalysis. *ACS Photonics* **6**, 1319–1330 (2019).

18. Albinsson, D. *et al.* Copper catalysis at operando conditions—bridging the gap between single nanoparticle probing and catalyst-bed-averaging. *Nat. Commun.* **11**, 4832 (2020).

19. Liu, S. *et al.* In Situ Plasmonic Nanospectroscopy of the CO Oxidation Reaction over Single Pt Nanoparticles. *ACS Nano* **13**, 6090–6100 (2019).

20. Albinsson, D. *et al. Operando* detection of single nanoparticle activity dynamics inside a model pore catalyst material. *Sci. Adv.* **6**, eaba7678 (2020).

21. Albinsson, D. *et al.* Shedding Light on CO Oxidation Surface Chemistry on Single Pt Catalyst Nanoparticles Inside a Nanofluidic Model Pore. *ACS Catal.* **11**, 2021–2033 (2021).

22. Larsson, E. M., Langhammer, C., Zorić, I. & Kasemo, B. Nanoplasmonic Probes of Catalytic Reactions. *Science (80-.).* **326**, 1091–1094 (2009).

23. Dahlin, A. B., Tegenfeldt, J. O. & Höök, F. Improving the Instrumental Resolution of Sensors Based on Localized Surface Plasmon Resonance. *Anal. Chem.* **78**, 4416–4423 (2006).

24. Taylor, A. B. & Zijlstra, P. Single-Molecule Plasmon Sensing: Current Status and Future Prospects. *ACS Sensors* **2**, 1103–1122 (2017).

25. Etchegoin, P. G. & Le Ru, E. C. A perspective on single molecule SERS: Current status and future challenges. *Phys. Chem. Chem. Phys.* **10**, 6079–6089 (2008).

26. Ding, S. Y., You, E. M., Tian, Z. Q. & Moskovits, M. Electromagnetic theories of surface-enhanced Raman spectroscopy. *Chem. Soc. Rev.* **46**, 4042–4076 (2017).

27. van Schrojenstein Lantman, E. M., Deckert-Gaudig, T., Mank, A. J. G., Deckert, V. & Weckhuysen, B. M. Catalytic processes monitored at the nanoscale with tip-enhanced Raman spectroscopy. *Nat. Nanotechnol.* **7**, 583–586 (2012).

28. Langhammer, C., Larsson, E. M., Kasemo, B. & Zorić, I. Indirect Nanoplasmonic Sensing: Ultrasensitive Experimental Platform for Nanomaterials Science and Optical Nanocalorimetry. *Nano Lett.* **10**, 3529–3538 (2010).

29. Dong, J.-C. *et al.* Direct In Situ Raman Spectroscopic Evidence of Oxygen Reduction Reaction Intermediates at High-Index Pt(hkl) Surfaces. *J. Am. Chem. Soc.* **142**, 715–719 (2020).

30. Swearer, D. F. *et al.* Heterometallic antenna-reactor complexes for photocatalysis. *Proc. Natl. Acad. Sci. U. S. A.* **113**, 8916–8920 (2016).

31. Antosiewicz, T. J., Wadell, C. & Langhammer, C. Plasmon-Assisted Indirect Light Absorption Engineering in Small Transition Metal Catalyst Nanoparticles. *Adv. Opt. Mater.* **3**, 1591–1599 (2015).

32. Zhou, L. *et al.* Light-driven methane dry reforming with single atomic site antenna-reactor plasmonic photocatalysts. *Nat. Energy* **5**, 61–70 (2020).

33. Vadai, M., Angell, D. K., Hayee, F., Sytwu, K. & Dionne, J. A. In-situ observation of plasmon-controlled photocatalytic dehydrogenation of individual palladium nanoparticles. *Nat. Commun.* **9**, 1–8 (2018).

34. Dunn, G. *et al.* Graphene-Sealed Flow Cells for in Situ Transmission Electron Microscopy of Liquid Samples. *ACS Nano* **14**, 9637–9643 (2020).

35. van der Wal, L. I., Turner, S. J. & Zečević, J. Developments and advances inin situtransmission electron microscopy for catalysis research. *Catal. Sci. Technol.* **11**, 3634–3658 (2021).

36. Yokosawa, T., Alan, T., Pandraud, G., Dam, B. & Zandbergen, H. In-situ TEM on (de)hydrogenation of Pd at 0.5-4.5bar hydrogen pressure and 20-400°C. *Ultramicroscopy* **112**, 47–52 (2012).

37. Giorgio, S. *et al.* Environmental electron microscopy (ETEM) for catalysts with a closed E-cell with carbon windows. *Ultramicroscopy* **106**, 503–507 (2006).

38. Creemer, J. F. *et al.* Atomic-scale electron microscopy at ambient pressure. *Ultramicroscopy* **108**, 993–998 (2008).

39. Williamson, M. J., Tromp, R. M., Vereecken, P. M., Hull, R. & Ross, F. M. Dynamic microscopy of nanoscale cluster growth at the solid-liquid interface. *Nat. Mater.* **2**, 532–536 (2003).

40. Kraus, T. & de Jonge, N. Dendritic Gold Nanowire Growth Observed in Liquid with Transmission Electron Microscopy. *Langmuir* **29**, 8427–8432 (2013).

41. Vendelbo, S. B. *et al.* Visualization of oscillatory behaviour of Pt nanoparticles catalysing CO oxidation. *Nat. Mater.* **13**, 884–890 (2014).

42. Ghosh, T. *et al.* Periodic structural changes in shape-controlled Pd nanoparticles during oscillatory CO oxidation. *Submitted* 1–10 (2022) doi:10.1038/s41467-022-33304-x.

43. Boyes, E. D., Lagrow, A. P., Ward, M. R., Mitchell, R. W. & Gai, P. L. Single Atom Dynamics in Chemical Reactions. *Acc. Chem. Res.* (2020) doi:10.1021/acs.accounts.9b00500.

44. Bacsa, W., Bacsa, R. & Myers, T. Microscopic Origin of the Index of Refraction. in *Optics Near Surfaces and at the Nanometer Scale* 65–83 (Springer International Publishing, 2020). doi:10.1007/978-3-030-58983-7_5.

45. Levin, S. *et al.* A nanofluidic device for parallel single nanoparticle catalysis in solution. *Nat. Commun.* **10**, (2019).

46. Levin, S. *et al.* Nanofluidic Trapping of Faceted Colloidal Nanocrystals for Parallel Single-Particle Catalysis. *ACS Nano* **16**, 15206–15214 (2022).

47. Špačková, B. *et al.* Label-free nanofluidic scattering microscopy of size and mass of single diffusing molecules and nanoparticles. *Nat. Methods* **19**, 751–758 (2022).

48. Swapnasrita, S. *et al.* Unravelling CO oxidation reaction kinetics on single Pd nanoparticles in nanoconfinement using a nanofluidic reactor and DSMC simulations. *Chem. Eng. Sci. X* **9**, 100088 (2021).

49. Sliney, D. H. What is light? the visible spectrum and beyond. *Eye* **30**, 222–229 (2016).

50. Bohren, C. F. & Huffman, D. R. Rayleigh-Gans Theory. *Absorpt. Scatt. Light by Small Part.* 158–165 (2007) doi:10.1002/9783527618156.ch6.

51. Sai, T., Saba, M., Dufresne, E. R., Steiner, U. & Wilts, B. D. Designing Refractive Index Fluids using the Kramers – Kronig Relations – Supplementary Information. *Faraday Discuss.* 1–4 (2020).

52. Kramers-Kronig Relations and Sum Rules in Linear Optics. in *Kramers-Kronig Relations in Optical Materials Research* 27–48 (Springer Berlin Heidelberg, 2005). doi:10.1007/3-540-27316-6_4.

53. Albinsson, D. *Combining nanoplasmonics and nanofluidics for single particle catalysis*. *Licentiate Thesis* (2018).

54. Thoms, L., Girwidz, R. & Munich, L. M. U. Experimenting from a Distance : Optical Spectrometry via the Internet. *MPTL18 – B. Proc.* 59–63 (2013).

55. Pope, R. M. & Fry, E. S. Absorption spectrum (380–700 nm) of pure water II Integrating cavity measurements. *Appl. Opt.* **36**, 8710 (1997).

56. Molina, L. T., Schinke, S. D. & Molina, M. J. Sist I of of and of. **4**, 80–82 (1977).

57. Malitson, I. H. Interspecimen Comparison of the Refractive Index of Fused Silica. *J. Opt. Soc. Am.* **55**, 1205–1209 (1965).

58. Bashkatov, A. N. & Genina, E. A. Water refractive index in dependence on temperature and wavelength: A simple approximation. *Proc. SPIE* 393–395 (2003) doi:10.1117/12.518857.

59. Giguère, P. A. & Geoffrion, P. REFRACTIVE INDEX OF HYDROGEN PEROXIDE SOLUTIONS. A REVISION. *Can. J. Res.* **27b**, 168–173 (1949).

60. Sai, T., Saba, M., Dufresne, E. R., Steiner, U. & Wilts, B. D. Designing refractive index fluids using the Kramers-Kronig relations. *Faraday Discuss.* **223**, 136–144 (2020).

61. Esmaeili, S. *et al.* Degradation products of the artificial azo dye, Allura red, inhibit esterase activity of carbonic anhydrase II: A basic in vitro study on the food safety of the colorant in terms of enzyme inhibition. *Food Chem.* **213**, 494–504 (2016).

62. Salem, M. A., Al-Ghonemiy, A. F. & Zaki, A. B. Photocatalytic degradation of Allura red and Quinoline yellow with Polyaniline/TiO2 nanocomposite. *Appl. Catal. B Environ.* **91**, 59–66 (2009).

63. Lin, C., Tao, K., Hua, D., Ma, Z. & Zhou, S. Size effect of gold nanoparticles in catalytic reduction of p-nitrophenol with NaBH4. *Molecules* **18**, 12609–12620 (2013).

64. Salem, M. A., Abdel-Halim, S. T., El-Sawy, A. E. H. M. & Zaki, A. B. Kinetics of degradation of allura red, ponceau 4R and carmosine dyes with potassium ferrioxalate complex in the presence of H2O2. *Chemosphere* **76**, 1088–1093 (2009).

65. Torres-Pérez, J., Medellín-Castillo, N. & Reyes-López, S. Y. α and γ Alumina Spheres for Azo Dye (Allura Red) Removal from Aqueous Media. *Adsorpt. Sci. Technol.* **2022**, (2022).

66. Ansar, S. M. *et al.* Removal of Molecular Adsorbates on Gold Nanoparticles Using Sodium Borohydride in Water. *Nano Lett.* **13**, 1226–1229 (2013).

67. Neal, R. D., Inoue, Y., Hughes, R. A. & Neretina, S. Catalytic Reduction of 4-Nitrophenol by Gold Catalysts: The Influence of Borohydride Concentration on the Induction Time. *J. Phys. Chem. C* **123**, 12894–12901 (2019).

68. Gungor, T., Gungor, E. & Saka, B. Fast and interference fringe independent optical characterization of zinc oxide nano thin films using model-based genetic algorithm for optoelectronic applications. *Nanomater. Nanotechnol.* **6**, 1–7 (2016).

69. Aspnes, D. E. & Studna, A. A. Dielectric functions and optical parameters of Si, Ge, GaP, GaAs, GaSb, InP, InAs, and InSb from 1.5 to 6.0 eV. *Phys. Rev. B* **27**, 985–1009 (1983).

70. Zhou, Y., Ma, Z., Tayebi, M. & Ai, Y. Submicron Particle Focusing and Exosome Sorting by Wavy Microchannel Structures within Viscoelastic Fluids. *Anal. Chem.* **91**, 4577–4584 (2019).

71. Bhagat, A. A. S., Kuntaegowdanahalli, S. S. & Papautsky, I. Continuous particle separation in spiral microchannels using dean flows and differential migration. *R. Soc. Chem.* **8**, 1906–1914 (2008).

72. Chiu, Y. Y., Huang, C. K. & Lu, Y. W. Enhancement of microfluidic particle separation using cross-flow filters with hydrodynamic focusing. *Biomicrofluidics* **10**, (2016).

73. Cruz, F. J. & Hjort, K. High pressure inertial focusing for separation and concentration of bacteria at high throughput. *J. Phys. Conf. Ser.* **922**, (2017).

74. Fouet, M. *et al.* Filter-less submicron hydrodynamic size sorting. *R. Soc. Chem.* **16**, 720–733 (2016).

75. Gou, Y., Jia, Y., Wang, P. & Sun, C. Progress of inertial microfluidics in principle and application. *Sensors (Switzerland)* **18**, (2018).

76. Ahmed, T., Shimizu, T. S. & Stocker, R. Microfluidics for bacterial chemotaxis. *Integr. Biol.* **2**, 604–629 (2010).

77. Gosetti, F. *et al.* Identification of photodegradation products of Allura Red AC (E129) in a beverage by ultra high performance liquid chromatography-quadrupole-time-of-flight mass spectrometry. *Anal. Chim. Acta* **746**, 84–89 (2012).

78. Hart, A. B. & Ross, R. A. Catalytic Decomposition of Hydrogen Peroxide Vapour by Equimolar Mixed Oxides. *Nature* **193**, 1175–1177 (1962).

79. Robbins, J. P. *et al.* Dependence of Hydrogen Peroxide Decomposition on the Size of Catalytic Gold Nanoparticles. 2 (2016).

80. Aeta, E. Peroxide Solutions on Platinum , Iridium , Palladium and Gold Surfaces *. *Solutions* **7**, 457–473 (1962).

81. Bianchi, G., Mazza, F. & Mussini, T. Catalytic decomposition of acid hydrogen peroxide solutions on platinum, iridium, palladium and gold surfaces. *Electrochim. Acta* **7**, 457–473 (1962).

82. Liu, J., Wei, X., Wang, X. & Liu, X. W. High-yield synthesis of ultrathin silica-based nanosheets and their superior catalytic activity in H2O2 decomposition. *Chem. Commun.* **47**, 6135–6137 (2011).

83. Menegazzo, F., Signoretto, M., Ghedini, E. & Strukul, G. Looking for the "dream catalyst" for hydrogen peroxide production from hydrogen and oxygen. *Catalysts* **9**, (2019).

84. Disselkamp, R. S. Energy Storage using Aqueous Hydrogen Peroxide. *Energy & Fuels* **22**, 2771–2774 (2008).

85. McDonnell-Worth, C. J. & MacFarlane, D. R. Progress towards direct hydrogen peroxide fuel cells (DHPFCs) as an energy storage concept. *Aust. J. Chem.* **71**, 781–788 (2018).

86. Chen, W. & Qu, B. Investigation of a platinum catalyst supported on a hydrogen peroxide-treated carbon black. *Int. J. Hydrogen Energy* **35**, 10102–10108 (2010).

87. Yi, L. *et al.* Carbon-Supported Bimetallic Platinum–Iron Nanocatalysts: Application in Direct Borohydride/Hydrogen Peroxide Fuel Cell. *ACS Sustain. Chem. Eng.* **6**, 8142–8149 (2018).

88. Langhammer, C., Kasemo, B. & Zorić, I. Absorption and scattering of light by Pt, Pd, Ag, and Au nanodisks: Absolute cross sections and branching ratios. *J. Chem. Phys.* **126**, (2007).

89. Preston, A. S., Hughes, R. A., Demille, T. B., Rey Davila, V. M. & Neretina, S. Dewetted nanostructures of gold, silver, copper, and palladium with enhanced faceting. *Acta Mater.* **165**, 15–25 (2019).

90. Van Omme, J. T. *et al.* Liquid phase transmission electron microscopy with flow and temperature control. *J. Mater. Chem. C* **8**, 10781–10790 (2020).

91. Pu, S., Gong, C. & Robertson, A. W. Liquid cell transmission electron microscopy and its applications. *R. Soc. Open Sci.* **7**, (2020).

Paper I

Nanofluidic Scattering Microscopy of Single Colloidal Platinum Nanoparticle H_2O_2 Decomposition Catalysis

Björn Altenburger, Carl Andersson, Sune Levin, Fredrik Westerlund, Joachim Fritzsche, and Christoph Langhammer

In Manuscript

Nanofluidic Scattering Microscopy of Single Colloidal Platinum Nanoparticle H_2O_2 Decomposition Catalysis

Björn Altenburger[1], Carl Andersson[1], Sune Levin[2], Fredrik Westerlund[2], Joachim Fritzsche[1] and Christoph Langhammer[1]*

[1]Department of Physics, Chalmers University of Technology; SE-412 96 Gothenburg, Sweden

[2]Department of Biology and Biological Engineering, Chalmers University of Technology; SE-412 96 Gothenburg, Sweden

*Corresponding author: clangham@chalmers.se

Abstract

Single particle catalysis aims at determining structural factors of nanoparticles that dictate their activity and selectivity, which may be lost in a particle ensemble averaged experiment. Existing experimental methods in this field have enabled fascinating insights into the role of specific sites but are typically executed using fluorescent reactions that technically are not highly relevant, take place at low reactant concentrations or pressures, or must rely on plasmonic enhancement effects. Hence, an experimental approach that enables the fluorescence-free investigation of catalytic reactions on single nanoparticles at technically relevant conditions and that at the same time facilitates quantitative determination of single nanoparticle turnover frequencies is still lacking. Here we introduce nanofluidic scattering microscopy of single colloidal Pt nanoparticles trapped inside nanofluidic channels to address this challenge. By relying on its ability to detect minuscule refractive index changes in a liquid flushed trough a nanochannel, we demonstrate that local H_2O_2 reactant concentrations adjacent to a single catalytically active Pt nanoparticle can be accurately measured during the H_2O_2 decomposition reaction, together with the same particles' turnover frequency derived from the growth rate of an O_2 gas bubble that forms in the channel from the O_2 reaction product. Applying this approach, we also identify a distinct dependence of single particle activity on the type of ligand on the catalyst, which highlights the potential of our method to investigate the role of surfactants in catalysis and to thereby enable the optimization of catalyst formulations by tailored ligands.

KEYWORDS: Single nanoparticle catalysis, Nanofluidics, Dark field microscopy, Colloidal particles, Platinum, Hydrogen Peroxide decomposition, Particle trapping, label-free methods

Introduction

The vision of single particle catalysis is to gain the ability to directly correlate the activity of a single nanoparticle obtained at practically relevant conditions with structural descriptors of that same particle. This is driven by the prospect of unprecedented fundamental insights beyond the current research frontier since catalytic properties of nanoparticles traditionally are evaluated at the ensemble level, that is, by averaging the response from a large number of them. From an atomistic perspective, however, this is problematic because nanoparticles are individuals in terms of their atomic arrangement and defects, and because they are dynamic entities at reaction conditions. Therefore, ensemble averaging brings along the inherent risk of erroneous structure-function correlations and that, for example, the most selective or most active "champion" nanoparticle types are hidden in the average.

To date, several experimental approaches for the study of catalytic processes on single nanoparticles exist[1–11]. In brief, the reported methods rely on the sensitive detection of photon or electron signals that report on either the catalyst particle itself, on the product molecules formed, on reactant molecules consumed, or on temperature changes that the reaction evokes in the particle surrounding. However, none of these methods can provide direct single particle activity information without (i) either using fluorescence-based readout that often limits the reaction conditions to ultralow concentrations and that cannot be applied to technically relevant reactions or (ii) using plasmonic enhancement effects when surface enhanced Raman spectroscopy (SERS), tip-enhance Raman spectroscopy (TERS), shell-isolated nanoparticle-enhanced Raman spectroscopy (SHINERS) is used.

To contribute to the quest of experimental method development that enables the efficient and quantitative scrutiny of catalytic reactions on single nanoparticles, we have recently introduced the concept of nanofluidic reactors and used them in combination with plasmonic nanoimaging

and spectroscopy and mass spectrometry in the gas phase[12–15], and with fluorescence microscopy in the liquid phase, using both nanofabricated particles[12–15] and individually trapped colloidal nanocrystals as the catalyst[16,17]. One of the key traits of this nanofluidic reactor platform is that it ensures identical reaction conditions for the individual particles during an experiment by isolating each of them in its own nanochannel. Thereby, it enables highly parallelized studies of tens of single nanoparticles in the same experiment, whereby it eliminates errors and uncertainties inherent to subsequent experiments traditionally used. In our first studies, this approach has made it possible to identify a distinct structure-sensitivity of fluorescein reduction by sodium borohydride on both nanofabricated and colloidal Au catalyst nanoparticles[16,17]. A second important trait of the nanoreactor approach that is of key interest here is the confinement of reaction product molecules formed on a single catalyst nanoparticle inside a nanofluidic channel since it prevents the rapid product dilution that otherwise is inevitable in an open reactor system, even if it is a microreactor[18,19]. Nevertheless, despite these traits, also the nanofluidic reactor based single particle catalysis studies we have presented to date, fall short on the demand to not use a fluorescent reaction or plasmonic effects to determine single catalyst nanoparticle activity and/or chemical and structural state.

Inspired by similar challenges in a different field of science, that is, optical single biomolecule detection, where fluorescent labels[20] or localized surface resonance-based sensors[21] are widely used, we have recently introduced Nanofluidic Scattering Microscopy (NSM) for the label-free weight and size determination of individual biomolecules freely diffusing in solution[22]. This was enabled by the intrinsically large optical scattering cross-section of nanofluidic channels and sub-wavelength interference between light scattered from a nanochannel and a biomolecule inside it. This interference significantly enhances the optical contrast of the molecule in a dark-field scattering microscopy setting and therefore makes the molecule directly visible without

fluorescent labels or immobilization on a surface, as required, for example, in interferometric scattering microscopy (iSCAT)[23,24] or plasmonic single molecule sensing[21].

Here, we have taken inspiration from the NSM methods' successful application in single molecule biophysics and apply it to single particle catalysis. Specifically, we demonstrate how NSM can be used to directly image and simultaneously quantify concentration gradients inside up to 85 parallel nanofluidic channels, based on the corresponding refractive index contrast. Furthermore, we show how individual optically dark Pt colloidal nanocrystals can be trapped inside the nanofluidic channels and visualized and counted. Finally, we demonstrate on the example of the fluorescence-free H_2O_2 decomposition reaction on single trapped Pt nanocrystals, how the local reactant concentration evolution can be measured *in situ* inside individual nanochannels, and how single-particle specific turn-over frequencies can be derived for citrate and polyvinylpyrrolidone (PVP) covered colloidal Pt nanocrystals by quantitatively analysing the light scattering of O_2 bubbles formed inside the nanochannels during reaction.

Results and discussion

The nanofluidic chip design we employ in this work is the same as in our previous work and the corresponding micro- and nanofabrication was carried out using the exact same recipe we have published earlier[17]. The chips comprise U-shaped microchannels on either side of the nanofluidic system they are connected to and are used to transport liquid to and from that system (**Figure 1a**). The nanochannels that constitute the system are arranged in a set of 100 parallel channels, where each channel is 340 µm long and has a quadratic 150 nm x 150 nm cross-section (**Figure 1b**). To enable the trapping of colloidal nanocrystals according to the recipe we have recently established[17], each nanochannel is equipped with a 120 nm high and 1 µm long constriction ("trap") in the center. When flushed through the nanochannel and arriving

at that trap, particles with a dimeter larger than the 30 nm gap between trap and nanochannel wall are captured, while substantial liquid flow through the channel is still enabled. The entire fluidic system of the chip, including the particle trap, is etched into the 2 µm thick thermal oxide layer of a silicon wafer and sealed by the bonding of a 175 µm thick glass lid (see Methods for details). A dark-field scattering microscope image of such a chip reveals the nanochannels as bright lines due to their large light scattering cross section in the visible spectral range[22] (**Figure 1c,d**). The dark regions in the center of each channel correspond to the traps as they reduce the scattering cross section of the channels by locally reducing the channel dimensions[22].

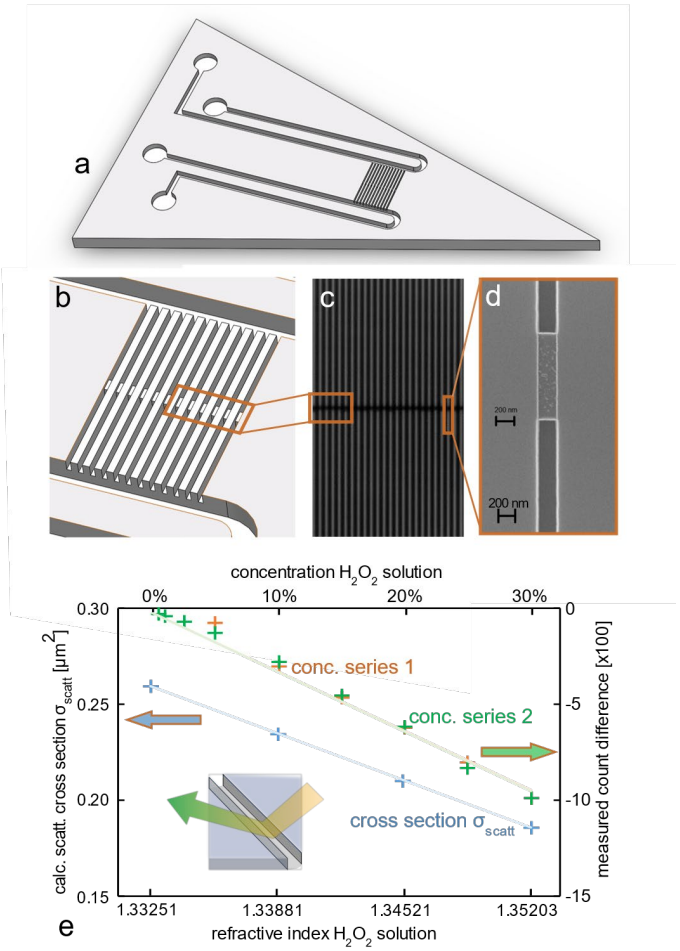

Figure 1. Nanofluidic chip design and scattering intensity dependence on liquid refractive index. *a) Artists' rendition of the nanofluidic chip used in experiments.*

Two inlet reservoirs are connected to two microchannels that connect to either side of a set of parallel nanochannels. They enable liquid flow through the nanochannels by applying pressure to the reservoirs on one side. b) Artists' rendition of the array of parallel nanochannels that is functionalized by a constriction ("trap") in the center region to enable the trapping of colloidal nanoparticles flushed through the system, provided the particles are larger than the trap in one dimension[17]*. c) Dark-field optical microscopy image of an array of nanochannels with a 150 nm x 150 nm cross section. The trap region that is 120 μm long and 120 nm high appears as a darker area due to the smaller scattering cross section of the nanochannel in this region*[22]*. d) SEM-picture of a single trap. e) Comparison of the theoretically calculated (equation 1) dependence of the nanochannel light scattering cross section on H_2O_2 concentration in water inside a nanochannel with the experimentally measured dependence of nanochannel scattering intensity on H_2O_2 concentration. The found linear dependence is the direct consequence of the linear dependence of the refractive index of the H_2O_2 solution on concentration.*[25]

Concentration gradient measurements in single nanochannels

To establish the measurement principle used in the experiments reported in this work, we first used a nanofluidic chip of the type describe above with empty channels, that is, without trapped nanoparticles. We then flushed aqueous H_2O_2 solutions with concentrations ranging from 0% to 30% through the system and measured the difference in light scattering intensity from a single channel compared to the same channel being filled with pure H_2O. This revealed a linear correlation in two independent measurements in good agreement with each other (**Figure 1e**). To rationalize this experimentally identified linear dependence, we employ Mie theory and approximate the nanochannels with square cross-sections used in the experiments by an infinitely long cylinder with a diameter of 150 nm. Following the formalism described by

Bohren and Huffmann[26] and detailed in the Supplementary Information Section SI II we arrive at an expression for the light scattering cross section of the nanochannel, $\sigma_{sca,u}$, upon irradiation by unpolarized light

$$\sigma_{sca,u} = \frac{A_{\emptyset}^2 k^3 L}{4}(m^2-1)^2\left(\frac{1}{2}+\frac{1}{(m^2+1)^2}\right). \qquad \textit{Equation 1}$$

Here, m is the ratio of the refractive indices (RI) of the liquid in the channel, n_l, and of the SiO_2 medium the channel is etched into, $n_{SiO2} = 1.459$,[27] that is, $m = n_l/n_{SiO2}$, $k = 2\pi/\lambda$ is the wavenumber, $A_{\emptyset}$ the geometrical nanochannel cross section and L the length of the illuminated channel section. To plot and compare the theoretically calculated scattering cross section with corresponding experimental scattering intensity measurements, we assume for pure water $n_w = 1.333$,[28] and for aqueous H_2O_2 solutions with 10%, 20% and 30% H_2O_2 concentration $n_{H2O2} = 1.3394; 1.3460;\ 1.353$, respectivly[29]. This corresponds to good first approximation to a linear dependence of the RI of water – H_2O_2 solutions, as reported by Hart and Ross[25]. Consequently, the value of m ranges between $m_w = 0.914$ for a water-filled channel and $m_{H2O2} = 0.928$ if a 30% H_2O_2 solution is introduced into the channel. This yields a linear dependence of the calculated nanochannel scattering cross section $\sigma_{sca,u}$, which is in excellent agreement with experimentally measured linear dependence of the scattering intensity (**Figure 1e**). As the key consequence, this result means that if appropriately calibrated, NSM enables absolute measurements of concentration changes in liquids inside a nanochannel.

Having established this direct proportionality between the light scattering intensity from a nanochannel and the H_2O_2 concentration inside it both theoretically and experimentally, we will now use it to measure dynamic changes of liquid composition inside a single nanochannel in real time and at the absolute level. This is of high relevance in the specific context of this work, where we aim at investigating the formation of concentration gradients due to chemical

conversion on a single nanoparticle, as well as in more general terms, to scrutinize fluid flow and diffusion in nanoconfined systems. In the first example to demonstrate this, we filled the two microfluidic systems contacting the set of nanofluidic channels with pure MilliQ water and a 30% aqueous H_2O_2 solution, respectively, and monitored the diffusion of the H_2O_2 solution into five initially water filled and 340 μm long parallel nanochannels (170 μm in the field of view). A corresponding time-series of selected scattering images reveals the approaching H_2O_2 diffusion front as a "darkening" of the channels from the righthand side (**Figure 2a**). This is the consequence of the lower RI of the H_2O_2 solution compared to pure water, which means that it is closer to the RI of the nanochannel walls and thus reduces the scattering intensity of the system (*cf.* Equation 1). Extracting the reduction of the scattering intensity along a single nanochannel at the same time intervals enables the establishing of a close to linear concentration profile after 10 s (**Figure 2b**). This is in good agreement with other works[30,31] that investigated the time evolution of concentration profiles between to solution reservoirs, as well as with the original diffusion laws established by Fick[32].

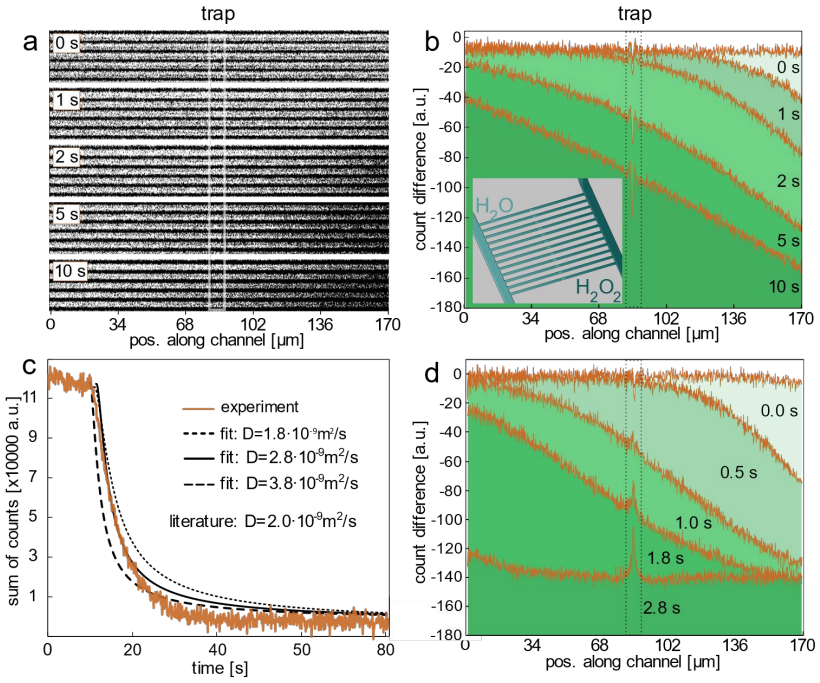

Figure 2. Assessment of H_2O_2 diffusion inside nanochannels. *a) Dark-field scattering microscope image of a set of five parallel nanochannels taken at different times after the onset of the diffusion of a 30 % H_2O_2 solution into the initially water filled channels. Note the approaching H_2O_2 diffusion front as a "darkening" of the channels from the righthand side, as a consequence of the reduced RI difference between channel and liquid inside it. b) Light scattering intensity difference between a nanochannel filled with pure MilliQ water at t=0 s and the same channel upon diffusion of a 30 % H_2O_2 solution into the channel from the right. The green shaded areas under the curves indicated the corresponding integrated areas, whose time evolution is plotted in c) together with corresponding evolutions calculated using equation 2 for three different D. The best agreement between experiment and calculation is found for for $D = 2.8 \cdot 10^{-9}\, m^2/s$, which is in very good agreement the literature value[33] of $D = 2 \cdot 10^{-9}\, m^2/s$. d) Similar scenario as for d), but with convective flow due to applied pressure at the microchannel inlets.*

To further quantify the measured time evolution of the concentration profile along the nanochannel, we used it to estimate the bulk diffusion constant, D, of H_2O_2 in water (**Figure 2c**). The concentration profile can be theoretically described over time with Equation 2, which we derived from Fick's second law for a nanochannel of length L, when a concentration of c_0 is present at one end at t=0.

$$c(x,t) = c_0\left(Erf\left(\frac{x}{2\sqrt{Dt}}\right)/Erf\left(\frac{L}{2\sqrt{Dt}}\right)\right) \qquad \textit{Equation 2}$$

To quantitively evaluate the changing concentration profile shown in Figure 2b, we integrated the area under the profiles at each time point and plot the time-dependent change of this integrated area in **Figure 2c**. This reveals the rapid establishing of the almost linear profile within the first two seconds followed by an asymptotic development towards the ideal perfectly linear profile. To extract *D* from these data, we analytically modeled the concentration profile in the channel using Equation 2, and applied the same evaluation scheme, that is, integration of the area under the profile curves, as done for the experimental data (cf. **Figure 2b** and **Figure S8**). Subsequently plotting the theoretically obtained curves for $D = 1.8 \cdot 10^{-9}\, m^2/s$, $D = 2.8 \cdot 10^{-9}\, m^2/s$ and $D = 3.8 \cdot 10^{-9}\, m^2/s$, we find the best agreement for $D = 2.8 \cdot 10^{-9}\, m^2/s$, which indeed is very close to the literature value[33] of $D = 2 \cdot 10^{-9}\, m^2/s$. This result is important from two perspectives: (i) it corroborates the ability of NSM to not only measure concentration changes inside nanofluidic systems but also enable the quantitative experimental determination of diffusion constants; (ii) it confirms that despite significant nanoconfinement, the macroscopic description of molecular diffusion is still valid. In a wider perspective, it also hints at the possibility to apply NSM in experimental studies of diffusion in more extremely confined systems where molecular interactions with the nanochannel walls become sizable and the eventually dominant contribution to diffusive molecular transport[34,35].

To investigate a second mass transport scenario through the nanochannels, we measured the development of the H_2O_2 concentration inside a nanochannel over time when in addition to diffusion also a convective flow was established from the 30 % H_2O_2 solution side to the pure water side, by applying a pressure difference of 1 bar between the two microfluidic systems on the chip at t = 0 s (**Figure 2d**). The corresponding scattering profiles measured at t = 1.0 s and 1.8 s resemble now an error function, in good agreement with corresponding theoretical

analysis by Fanchi[36]. Hence, these data visualize nicely how diffusion of H_2O_2 superimposed onto the convective flow changes the concentration front that is moving through the nanochannel.

As a final aspect to we focus on the evolution of the scattering intensity in the trap area in **Figure 2c,d**, which is indicated by the dashed lines. We find that in this region both small positive and negative peaks evolve, which likely are the consequence of the significantly reduced scattering intensity in the trap region and the consequent negative impact on S/N.

Platinum nanoparticle trapping and imaging

To prepare the nanofluidic chips for measurements of the catalytic decomposition of H_2O_2 over single nanoparticles, we functionalized the channels by trapping citrate-stabilized spherical colloidal Pt nanoparticles comprised of small 2 – 5 nm crystallites (see **Figure 3a)** and with a mean diameter of 69.6 nm, as evident from a size distribution histogram obtained from scanning electron microscope images (**Figure 3b**). For the particle trapping, we filled the inlet reservoir of the microfluidic system on the inlet side of an already water-filled chip with a diluted aqueous suspension of the Pt particles (10^9 particles/mL). Subsequently, we applied 2 bar pressure to the inlet side of the chip to establish a flow through the microchannels that transported the particles into the nanochannels, where they will get trapped at the position of the constriction.

To monitor this process, we imaged the 84 parallel nanochannels in the field of view of the CCD camera at a frame rate of 10 fps and subtracted a reference image of the empty channels from each frame (**Figure 3c**). This reference image was the first image of the series of 1000 images acquired during the particle trapping and shows therefore the nanochannels before any particles were flushed in. This procedure results in a time series of differential images in which

the Pt particles become visible as distinct dark spots (**Figure 3d,e**). This is an important result because optically lossy metal nanoparticles, such as Pt or Pd, are invisible in conventional dark-field scattering microscopy in the sub 100 nm particle size range due to their localized surface plasmon resonance (LSPR) excitations predominantly decaying via absorption, rather than scattering[37] Here, however, we propose that they become visible because of two potential mechanisms. According to the first one, since also Pt particles scatter light, even though very little, this light may interfere with the light scattered from the nanochannel, thereby reducing the overall intensity scattered from the combined system (that is, particle plus channel) in analogy to the NSM enhancement mechanism in single molecule detection[22]. According to the second and more likely dominating mechanism, a sizable fraction of the light scattered from the nanochannel is absorbed by the Pt particle and thus the reason for the observed scattering intensity reduction at the position of the particle in the channel in the differential image.

Irrespective of the mechanism, our method offers a complement to traditional dark-field scattering microscopy of metal/plasmonic nanoparticles in the sub ≈ 50 nm particle size range and/or for lossy metals where absorption is the dominant LSPR decay channel and thus renders them "invisible" in a traditional scattering experiment[37]. Consequently, it also enables the tracking of the motion of such single nanoparticles inside the nanofluidic channels, as illustrated in **Figure 3e** that depicts snapshots of five channels over the course of 15 s. The starting point of this experiment is that particles have been trapped at the constriction by the flow applied through the nanochannels. This flow was then stopped at t = 0 s when the first image was taken. Interestingly, already after 0.1 s, the particles have started to drift away from the trap. This motion is a combination of Brownian diffusive motion and a minuscule convective flow that has its likely origin in a small difference in the static pressure induced by the liquid in the reservoirs of the microfluidic system. Consequently, the particles continued to exhibit a net motion in the direction away from the trap during the subsequent 15 s until we

again established a distinct convective flow towards the trap that pushed the particles back towards it (**Figure 3e)**.

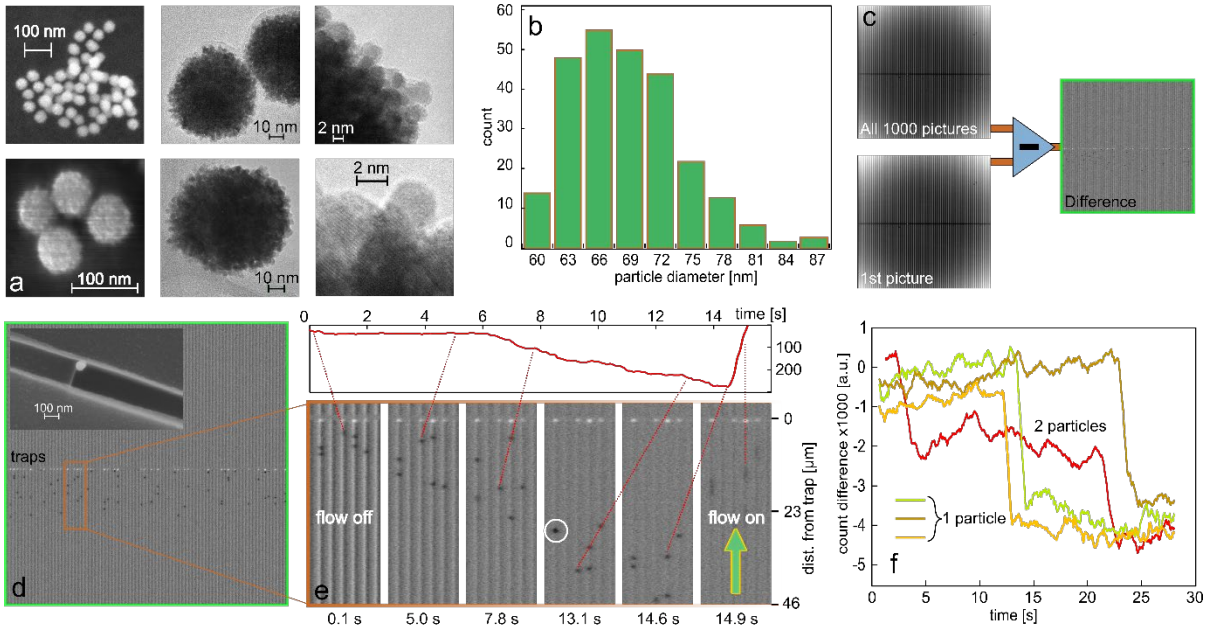

Figure 3. Pt nanoparticle characterization, trapping, optical detection and counting. *a) SEM and HRTEM images of the citrate-stabilized Pt nanoparticles used in this work. They reveal that the particles are comprised of small 2 – 5 nm crystallites. b) Particle diameter histogram obtained from SEM image analysis, yielding a wide size distribution with a mean particle diameter of 69,6 nm. c) Scheme depicting the generation of differential images by subtracting the first image of a measurement series, obtained when no particles had yet entered the channels, from subsequently taken images. d) Differential scattering image revealing the Pt nanoparticles as dark spots in the channels. The inset shows a SEM image of one 70 nm Pt particle in front of a constriction. e) Time series of differential images focused on 5 parallel nanochannels that reveals the net motion of nanoparticles away from the trap (bright area on top of the images) in a combination of Brownian motion and slow convective flow before reverting the flow direction in the last image at 14.9 s to push the particles back towards the trap. We also note the transient localization of two particles within a diffraction limited spot, which is reflected as a significantly darker spot in the leftmost channel at 13.1 seconds (white circle). The inset depicts the position of a single particle along the channel over time. g) Differential scattering intensity time traces of the trap region where distinct steps signal the arrival of a single Pt nanoparticle at the trap. In the red trace, the subsequent arrival of two single particles is observed.*

To discuss a further interesting aspect of **Figure 3e**, we focus on leftmost nanochannel. We notice that two distinct single particles are in this channel at t = 0.1 s and that they form a "dimer" at 13.1 s where they appear as a single spot that is significantly darker compared to the images where the two particles are seen individually (white circle in **Figure 3e**) . This is the consequence of the particles being transiently localized close to each other at a distance smaller than the diffraction limit of the irradiated light. Analyzing quantitatively the scattering intensity of the system at the position of the two individual particles at 5 s, where they are distinctly visible, and at the position of the particle "dimer" at 13.1 s, reveals a 40% lower scattering intensity of the dimer compared to the single particles, which hints at a $\sqrt{N}$ dependence of scattering intensity with particle number localized inside a diffraction limited spot (**Figure S7**).

As the final step, we demonstrate that this distinct reduction in scattering intensity induced by single nanoparticles inside a nanochannel enables their counting also at the position of the trap. Specifically, their arrival at the constriction is manifested as a distinct step in the time trace of the scattering intensity measured at the trap, which enables the detection of the arrival of single and multiple individual nanoparticles inside a single nanochannel in analogy to our previous work[17] (**Figure 3f**). This is important to ensure that the desired number of particles inside each nanochannel can be verified prior to the catalysis experiments we discuss below, where we target a situation with as many channels being functionalized with a single nanoparticle only.

H_2O_2 decomposition over single Pt nanoparticles

Having established the trapping and imaging of the single Pt nanoparticles, as well as the measurement of concentration changes in the solution inside the nanochannel, we now apply the developed system to investigate a catalytic reaction. For this purpose, we have chosen the

catalytic decomposition of H_2O_2 on Pt, which takes place according to a two-step cyclic mechanism[38]. In the first and rate limiting step a H_2O_2 molecule reacts with the Pt surface and forms a chemisorbed oxygen on the Pt surface, Pt(O), and a water molecule, H_2O, that desorbs from the surface. In the second step, a second H_2O_2 molecule reduces the Pt(O) back to metallic Pt by forming O_2 and H_2O, which both desorb from the catalyst and thereby close the cycle. This yields an overall reaction that can be written as

$$2H_2O_2 \overset{Pt}{\rightarrow} 2H_2O + O_2. \qquad \textit{Equation 3}$$

Focusing on the Pt nanoparticles, due to their structure that features relatively small crystallites at the surface, they are characterized by a large surface area that features both edges and terraces at relatively high abundance. Hence, they are expected to be highly active due to the interplay between high (terraces) and low (edges) coordination sites, which in combination keeps binding energies of reactants and intermediates at a moderate level and thus sees to that the activation energy of the rate determining step and the reactant surface coverage is relatively low[38]. Furthermore, the highly structured surface facilitates the effective detachment of oxygen bubbles from the particles. Such bubbles are expected to form on the surface during reaction if the reaction rate is high enough to produce more O_2 than what can be dissolved in water.[39]

Projecting the potential of the H_2O_2 decomposition reaction to form O_2 bubbles onto our nanofluidic reactor system at hand (**Figure 4a**), after the detachment of O_2 from the surface of a trapped Pt nanoparticle inside a nanochannel, there are two possible scenarios according to which it can condense into a larger bubble when the O_2 solubility limit (1.22 mol/m^3 in water[33]) is reached. *Scenario I:* following the direction of the convective flow through the channel, a bubble is formed downstream of the particle and across the trap constriction (**Figure 4b**).

Scenario II: growing against the direction of the convective flow through the channel, a bubble is formed upstream of the constriction, either between trap and particle or upstream of the particle (**Figure 4c**).

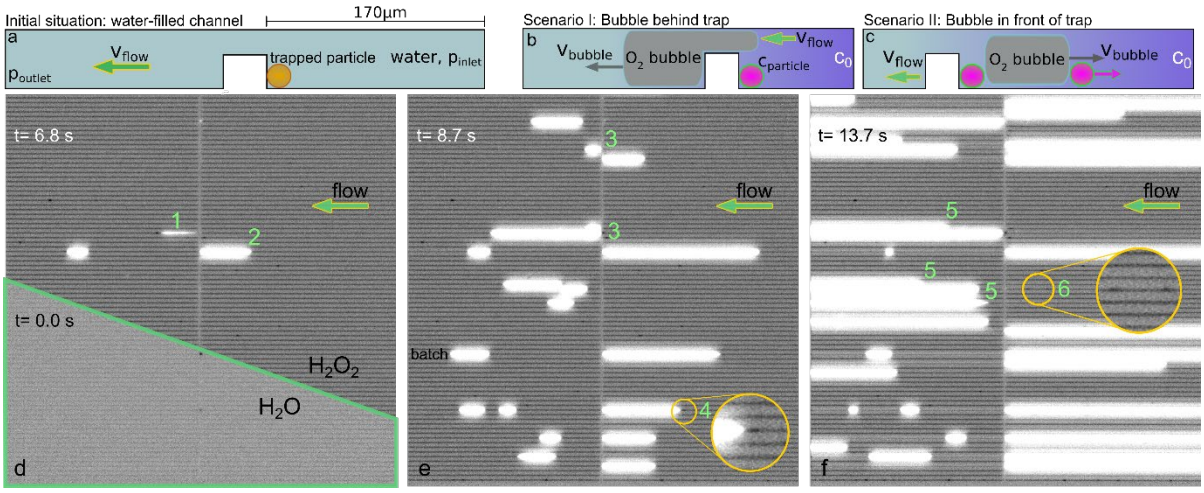

Figure 4. H_2O_2 decomposition reaction on Pt nanoparticles and O_2 bubble formation. *a) Schematic of the initial situation with a trapped Pt particle and the entire nanochannel filled with water. b) Scenario I: upon convective inflow of H_2O_2 into the nanochannel from the righthand side a bubble of O_2 gas forms downstream of the particle due to the catalytic decomposition of the H_2O_2 on the particle surface. c) Scenario II: the O_2 bubble either forms between trap and particle or upstream of the particle. In both cases it grows upstream against the convective inflow of H_2O_2. d) Darkfield scattering images of the completely water-filled nanochannel system after trapping of Pt nanoparticles (green frame) and the system after complete liquid exchange to 30 % H_2O_2 manifested by the darker appearance of the channels at t=6.8 s. We also note the onset of O_2 bubble formation on two particles (highlighted by label 1 and 2 – see main text for details) manifested as areas of intense light scattering. e) Darkfield scattering image of the nanochannel system at* t=8.7 s *when multiple additional bubbles have formed. The labels highlight specific scenarios discussed in detail in the main text. f) Darkfield scattering image of the nanochannel system at* t=13.7 s. *The labels highlight specific scenarios discussed in detail in the main text. For all images we note that dark spots not positioned close to the traps are artefacts caused by structural defects of the nanochannels generated during their fabrication (that is, they are no Pt particles). The field of view corresponds to 170 µm x 170 µm.*

To investigate these two possible scenarios, we trapped Pt nanoparticles in the nanochannels and monitored the trapping process using the concept outlined above (cf. **Figure 3f**). Subsequently, we exposed the trapped particles to a flow of 30 % H_2O_2 in the direction towards the trap. This resulted in 14 parallel nanochannels exhibiting Scenario I, whereof one channel was occupied by a single Pt nanoparticle, ten channels were occupied by 2 nanoparticles and three channels were hosting 3 or more particles (**Figure S9**). Furthermore, twelve nanochannels exhibited Scenario II. Finally, some particles also attached to the nanochannel wall before reaching the trap (see **Figure S5** for an example).

After the functionalization of the chip with the Pt particles, we investigated the bubble evolution via a series of dark-field scattering images taken from the parallel nanochannels (**Figure 4d-f**). For this experiment, with the Pt particles at the trap, we started out with water in one microfluidic channel and in the nanochannels, and with 30 % H_2O_2 in water in the second microchannel. Subsequently, we established convective flow from the H_2O_2 side through the nanofluidic system by applying 2 bar pressure on the H_2O_2 inlet reservoirs. At start, the particles were still fully immersed in water, as one can see from the overall relatively bright image which turns distinctly darker as all channels are filled with 30 % H_2O_2 (**Figure 4d**). Subsequently, when H_2O_2 had been flushed in, O_2 bubbles started to form as the H_2O_2 decomposition reaction was initiated. In general, the appearance of an O_2 bubble is manifested as a dramatic increase in scattering intensity since it locally expels the liquid from the nanochannel and thereby changes the refractive index contrast of the system significantly. From here forward, we will discuss in detail several particularly interesting events specifically labeled in green in **Figure 4d-f**.

Label 1 highlights an event occurring when the reaction starts on the first particles in the system, where an initial O_2 bubble is formed at a Pt particle caught at the trap but then detaches

from that particle and is moved through the nanochannel by the flow (**Figure 4d**). Label 2 highlights the formation of an O_2 bubble according to scenario II in a neighboring channel. After 8.7 s more bubbles have started to form at an increasing number of Pt particles (**Figure 4d**), and we can see examples for scenario I and II (Label 3 in **Figure 4e**). Interestingly and marked by label 4, a Pt particle seen as the dark spot in in the zoom-in, is being pushed out by the bubble that in this case grows between the particle and the trap. **Figure 4f** shows the later stages of the measurement series, with several bubbles having reached the end of the field of view and with many channels exhibiting Scenarios I and II. Label 5 marks large bubbles in Scenario I that have detached from the trap and are on the way to being flushed out of their channel. Label 6 highlights two particles (dark spots in the zoom-in) that have drifted away from the trap since the convective flow through the channel is significantly reduced by the O_2 bubble downstream in the same channel.

To further analyze the made observations, it is interesting to discuss them from the perspective of the two scenarios depicted in **Figure 4b,c**. In the first scenario, where the O_2 bubble grows in the direction of the applied H_2O_2 flow and downstream of the particle trap, the situation is rather straightforward (**Figure 4b**) since H_2O_2 has unrestricted access to the particle via convective flow and diffusion, and since the particle remains in position at the trap during the entire experiment while the bubble extends on the other side of the trap towards the outlet microchannel. However, we also note that the bubble growing downstream of the trap will reduce the convective flow through the channel gradually as it grows, since it increases the flow resistance of the system (**Figure S 1**). At the same time, it will not completely block the flow through the channel due to the hydrophilicity of the channel inner walls, which ensures that a thin layer of liquid is sustained between the O_2 bubble and the nanochannel wall.

Scenario II (**Figure 4c**) is more complicated because: (i) if the bubble nucleates between trap and particle the bubble may expel the particle from the channel during growth by pushing it ahead (cf. label 4 in **Figure 4e**); (ii) if the bubble nucleates and grows away from the particle against the convective flow, it effectively blocks a large fraction of the H_2O_2 inflow by occupying a large fraction of the channel cross-section. However, since it does not block the inflow completely due to the liquid layer between wall and bubble mentioned above, a continuous, yet reduced, supply of H_2O_2 that ensures the continued O_2 formation and bubble growth that we observe in the experiment. However, at a decreasing rate as the bubble expands due to the correspondingly increasing flow resistance (**Figure S 1**).

Finally, it is also interesting to estimate to what extent the O_2 bubbles fill out the channel cross section and thereby get an indication for the dimensions of the liquid layer between bubble and channel wall. To do this, we compared the light scattering intensities of completely air-filled channels with channels filled with an O_2 bubble formed by the H_2O_2 decomposition reaction. This analysis yields a filling factor of 75.5 % of the total nanochannel cross section by the O_2 bubbles (**Figure S3**), which translates into an estimated liquid layer thickness of 9 nm between the nanochannel wall and a bubble inside it.

The immediate conclusions from the above analysis are that we for further quantitative study of the catalytic reaction exclusively focus on scenario I, where bubble growth occurs on the downstream side of the particle and the trap, and where tracing the spatial extension of an O_2 bubble along the nanochannel over time provides insight into the amount of O_2 produced in the H_2O_2 decomposition reaction on a single Pt nanoparticle surface. In fact, since the filling factor of the bubble and the exact geometry of the nanochannel are known, the absolute amount of gas phase O_2 produced over time can be accurately calculated. Consequently, we can define a bubble extension speed (BES), which is the change of bubble length in pixels per second, multiplied with the scale of 0.166 µm per pixel. This BES is then directly proportional to the

current reaction rate of the particle. The influence of the solubility of the formed O_2 in water is shortly discussed in SI section II. An example of a single Pt nanoparticle BES time trace is shown in **Figure 5a**, together with the scattering intensity integrated along 85 µm of the channel up- and downstream of the trap, respectively. We note that a BES trace automatically ends when the moving front of the bubble reaches the edge of the field of view or detaches from the trap, that is, when the whole bubble and not only its leading edge is moving through the nanochannel.

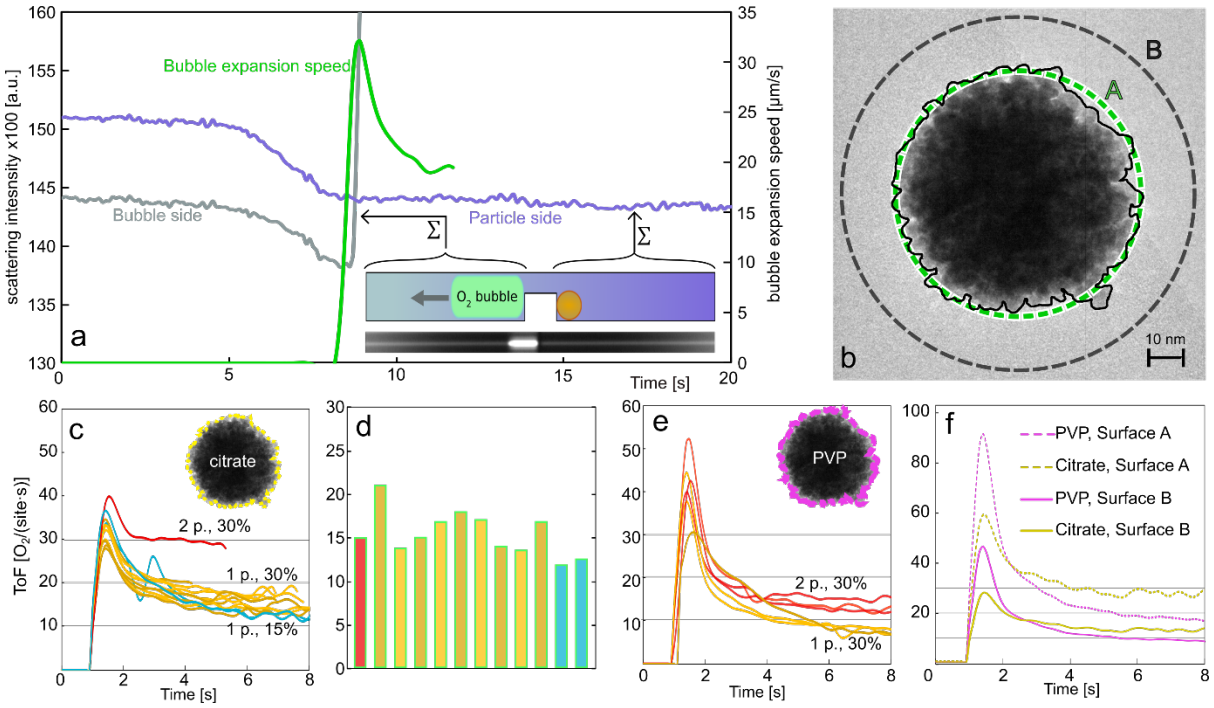

Figure 5. Single particle reaction turnover frequencies (ToF) and local reactant concentrations in the nanochannel. *a) Time traces of nanochannel scattering intensity integrated along 85 µm of the channel up- (purple) and downstream (grey) of the trap (see inset) plotted together with the bubble expansion speed (BES, green) for a bubble forming downstream of a single Pt nanoparticle trapped at the constriction (see second inset for corresponding dark field scattering image snapshot). The time traces start at t= 0 s when the channel is entirely filled with water and subsequently flushed with 30 % H_2O_2. Note the initial reduction of the scattering intensity signals prior to the onset and steep increase of the BES, as well as the ca. 1 s time delay in the scattering intensity decrease between the up- and*

downstream signals that is the consequence of the convective transport of H_2O_2 trough the channel to replace the water (see also see

It is now interesting to in detail discuss the time evolution of the BES and the integrated channel scattering intensities extracted both up- and downstream of the trap with the Pt particle (**Figure 5a**). Focusing first on the scattering intensity traces, from t = 0 s they initially remain constant up- and downstream of the trap since the channel in this state is entirely filled with water and no O_2 bubble is present. We note that the small difference in integrated scattering intensity between the up- and downstream trace at t = 0 s is the consequence of a slightly inhomogeneous illumination across the field of view (**cf. Figure 3c**). Subsequently, after ca. 5 s the scattering intensity starts to decrease and signals the arrival of the 30% H_2O_2 solution in the respective channel sections. Interestingly, we can resolve a small delay of 1 s (

Figure S*6*) between the up- and downstream side, in agreement with the convective flow of the H_2O_2 through the nanochannel. Furthermore, focusing on the BES trace, we notice that its onset nicely coincides with the 30% H_2O_2 concentration being fully established at the particle position, which confirms that the bubble nucleates and grows once the catalyst particle is fully immersed in the reactant solution. At the same time, we find that the single particles that exhibit this early onset of bubble formation often are those who subsequently exhibit the highest BES, once the 30% H_2O_2 concentration is reached in the channel (**Figure S9b**). This indicates a correlation between single particle activity and onset of bubble formation since a lower H_2O_2 concentration appears to be sufficient for the most active particles (or an agglomeration of several particles) to generate enough O_2 to nucleate a bubble.

As a second aspect, it is interesting to analyze how the H_2O_2 concentration in the nanochannel evolves while the decomposition reaction is running on the particle because it sheds light on whether concentration gradients are being formed due to reactant conversion and if the catalyst is operated in a mass-transport or kinetically controlled regime. Accordingly monitoring the

scattering intensity time trace upstream of the particle, that is, in the direction of reactant supply, reveals that it essentially remains constant at the same level as at the onset of bubble formation (**Figure 5a**). Since we, based on the earlier calibration of the scattering intensity towards H_2O_2 concentration (**cf. Figure 1**), know that the measured signal corresponds to the nominal 30% H_2O_2 in water in the inlet, we can conclude that the concentration upstream of the particle remains constant and is not depleted over time. This is an important result, because it is the experimental proof that the combination of convective flow and rapid H_2O_2 diffusion towards the catalyst nanoparticle is fast enough to prevent the formation of a gradient. Hence, it confirms that we are operating the catalyst particle in the kinetically limited regime and at a well-defined concentration. This, in turn, means that the particle-specific reaction rates we determine and discuss below are a direct consequence of single particle structure and activity.

As additional key points, we note that once the bubble has formed the scattering intensity on the downstream side raises rapidly, meaning that we no longer can trace H_2O_2 concentration. Secondly, during the initial phase of bubble formation and growth, we observe a distinct maximum in the BES before it first slows down significantly and rapidly and then converges towards a seemingly steady state. While we discuss the origin of the distinct peak in BES further below, we already here note that the slight continuous decrease of the BES in the quasi steady state regime may have its cause either in a slow degradation of the particle or is the consequence of, at the level of the chip, many nanochannels with many active particles being connected to the same H_2O_2 reservoir, thereby slowly reducing the total H_2O_2 concentration in the system.

As the next step of our analysis, we now attempt to convert the measured single nanoparticle BES into a turnover frequency (ToF) per site and second. To do that, beyond knowing the amount of O_2 formed per unit time, we need to determine the surface area of the Pt particles at hand to derive an estimate of the number of active sites. We resort to a high-resolution TEM

image of a single Pt nanoparticle, which reveals that the surface is rough due to the particle being comprised of small crystallites (**Figure 5b**). This in turn means that the real surface area is much larger than the one corresponding to a smooth sphere with 70 nm diameter (green dashed line in **Figure 5b**). To estimate a more realistic surface area, we thus draw the outline of the 2D projection of the rough particle surface seen in the TEM image (solid black line in **Figure 5b**) and convert it into a smooth circle with corresponding circumference (dashed black line in **Figure 5b**). This analysis reveals that the realistic surface area of our particles with nominal ≈70 nm diameter (surface area 15394 nm^2 for a smooth sphere) rather corresponds to a smooth spherical particle with ≈100 nm diameter and 31416 nm^2 surface area.

At this point, it is necessary to discuss the reaction mechanism of H_2O_2 decomposition and the possible influence of the surface structure, as there are multiple pathways that lead to the production of O_2 and water[38]. As reported by Serra-Maia et. al.[38], the rate limiting step is the dissociation of an H_2O_2 molecule into a surface bound oxygen and H_2O. This happens preferentially on the highly coordinated (111) and (100) terrace sites because the corresponding binding energies for oxygen are significantly higher than on edge/corner sites, which thereby lowers the activation of the rate limiting step on the terraces. Given the size of the crystallites in the few nanometer range that the particles in our experiments are composed of, as a rough estimate, we assume that half of their surface is comprised of terrace sites and that the other half corresponds to edge/corners. For our estimation of the ToF below, we therefore assume that 50% of the total number of surface atoms are active sites for the H_2O_2 decomposition reaction[40]

Based on the above assumptions, we now use the experimentally determined BES (in m/s) and the geometric cross section area of the nanochannel, A = 150 nm x 150 nm, to arrive at the

following expression for the ToF per site per second of a Pt nanoparticle inside a nanochannel (a more detailed derivation is given in **SI Section II**)

$$ToF = \frac{0.755 * A * BES * N_A}{V_{O2}^{mol} N} \qquad \textit{Equation 3}$$

where, V_{O2}^{mol} = 22.39 mol/l is the molar volume of O_2 at atmospheric pressure, N_A is Avogadro's constant, N is the estimated number of active sites for the nanoparticle of interest. To determine it, we use the particle analyzed in **Figure 5b**, for which we calculated at the lower end a surface area for a sphere of 70 nm diameter to 15394 nm^2 and for a sphere of 100 nm diameter at the high end a surface area of 31416 nm^2. Assuming an atomic surface density of $1.53 \cdot 10^{19}$ atoms per m^2 for Pt, calculated from the interatomic distance[41], this results in a total of 235525 surface atoms for the lower and 480664 surface atoms for the upper surface area limit, respectively. Finally, applying the estimation that only 50 % of these atoms are located in the terrace sites that are important for the rate-limiting step of oxygen adsorption[38], we arrive at an estimated range of 117763 to 240332 active sites on our particles. We also note that the 0.775 prefactor has its origin in the 75.5% filling factor for the bubble in the channel that we estimated in **Figure S3**.

By applying these numbers and using the upper particle surface area limit (surface B in **Figure 5b**), we can now calculate ToFs for 9 citrate capped single Pt nanoparticles trapped in individual nanochannels and plot their ToF time evolution for a 30% H_2O_2 concentration in the reactant solution together with two single particles measured in 15% H_2O_2 and with two particles trapped in a single channel measured in a 30% H_2O_2 (**Figure 5c**).

All these ToF time traces have in common that they exhibit an initial rapid rise of the reaction rate (which is the consequence of the correspondingly observed rapid rise of the BES mentioned above, cf. **Figure 5a**), which subsequently drops and converges to a reasonably constant value after approximately 5 s. Focusing on this relatively stable regime, we can extract

the corresponding ToF values for each single particle (**Figure 5d**) and the mean value for each condition, that is, for the single particles in 30% H_2O_2 we find ToF = 16 ± 2.3 $site^{-1} \bullet s^{-1}$, for the single particles in 15% H_2O_2 we find ToF = 12 ± 0.3 $site^{-1} \bullet s^{-1}$ and for the two particles in 30% H_2O_2 we find ToF = 14.7 $site^{-1} \bullet s^{-1}$. In combination with the fact that we from the channel scattering intensity measurements know that no concentration gradients are formed in the channel during reaction, and we thus do not expect mass transport limitations, the values imply that the lower ToF found for 15% H_2O_2 is the consequence of a strongly concentration dependent H_2O_2 coverage on the particle surface as the reason for the reduced reaction rate at lower concentration. It is also understandable that we see a higher BES when two particles are in one channel, but when we consider the ToF for this scenario, it is slightly lower than the mean single particle value but still within the standard deviation. We also note the significant spread in ToF between individual nanoparticles (**Figure 5c,d, Figure S9c**). It can be attributed to their individual structure mostly in terms of size (cf. **Figure 3a and b**) and nicely demonstrates one of the key motivations for developing single particle techniques for the investigation of structure-function correlations.

As the final aspect it is relevant to discuss the observed distinct peak in BES (and consequently the derived ToF) after onset of the reaction (**Figure 5c,e**). We propose that this BES peak has its origin in the initial phase of bubble nucleation, coalescence, and growth on the nanoparticle surface. Specifically, as the reaction is initiated and O_2 starts to be produced, a multitude of small O_2 bubbles form on the particle surface and start to grow. Eventually, when they have reached a critical size, they detach from the particle surface[39] and coalesce into a single large bubble that starts to occupy the nanochannel and is monitored in the experiment. In this initial stage of formation and growth of this large bubble in the channel, its growth rate is not directly determined by the O_2 production rate of catalyst surface but instead dictated by the number and volume of already available small O_2 bubbles that the catalyst already has produced. In other

words, in this phase the BSE reflects the rate of coalescence of small O_2 bubbles into a large one, rather than the O_2 formation rate on the surface. Since this rate is determined by the amount of O_2 already produced, it transiently exceeds the O_2 formation rate of the catalyst until a new steady state is reached, where the O_2 formation rate on the particle surface is proportional to the BES.

As a next step we attempt to compare the obtained single nanoparticle ToF values to the literature. This, however, proves difficult since a wide range of both catalyst materials and reaction conditions are reported. Serra-Maia et. al.[38] investigate Pt nanoparticles ranging from 22 nm to 3 nm in size in but only at very low H_2O_2 concentrations of 0.001 mol/l H_2O_2, which is is almost four orders lower than our 30 % H_2O_2 that translates into 9,7 mol/l. As a second example, Liu et. al.[42] reported the amount of O_2 produced by a silica-based nanosheet with supported sub-2 nm Pt nanoparticle catalyst in 3 % H_2O_2 in water and found an O_2 production rate of 343 ml/(min • g) by using the weight of the used catalyst as reference. Correspondingly calculating the volume of O_2 produced by a single nanopartice (weight $3.85 \cdot 10^{-15}$ g) in our experiment, we find a rate of 1153 ml/(min • g). While different by a factor 10, this results rationalizes our single particle ToFs in a reasonable way, in particular since the Pt loading in Liu et al. was only 0.4 wt. %.

PVP vs. citrate coated Pt nanoparticle activity

To further explore our experimental concept and, in a proof of principle fashion, demonstrate its ability to assess the impact of ligands on the surface of the Pt nanoparticles on catalytic activity, we modified our initially citrate covered Pt particles by exchanging the citrate ligands to polyvinylpyrrolidone (PVP, 10 kDa), as described in the methods section, and trapped them in the nanochannels (

Figure S*4*). PVP binds strongly to Pt[43], with a distinct preference for (100) terraces and edge sites[44]. Consequently, we expect a PVP coated particle to exhibit lower activity towards H_2O_2 decomposition than a citrate coated particle since more active sites are effectively blocked by the strongly bonded and geometrically larger ligands[45]. Evaluating the ToF derived from the BES measured upon exposure of three single and three dimers of PVP coated Pt particles to a 30% H_2O_2 solution reveals indeed a reduced ToF in the steady state regime (**Figure 5e**) by roughly a factor 2, that is, from 16 ± 2.3 site^{-1} • s^{-1} to 7.9 ± 0.5 site^{-1} • s^{-1} in mean ToF for the single nanoparticles (**Figure 5f**). The also observed difference in BES and ToF peak height for the PVP and citrate covered particles during the onset of the reaction is likely the consequence of different initial bubble growth, detachment and coalescence on these two surfaces. Taken all together these results corroborate the significant impact of ligands on catalytic properties of nanoparticles[46].

Spontaneous batch reactor formation

At rare occasions, we have observed a scenario in the nanofluidic system where an O_2 bubble that has formed according to scenario I detaches from the trap and is swept downstream by the convective flow until it gets stuck at a defect in the nanochannel wall. Simultaneously, a new O_2 bubble is formed on the Pt particle(s) still localized at the trap, but this time according to scenario II, where the bubble grows upstream of the particles against the flow (**Figure 6a**). This creates the interesting scenario where the two bubbles effectively enclose a segment of the channel with the catalyst trapped inside. Since the H_2O_2 enclosed in this segment is on one hand rapidly consumed by the reaction on the catalyst and on the other hand only slowly resupplied via the narrow layer at the bubble-channel wall interface, this scenario essentially creates a “batch reactor”. Using the scattering intensity signal measured from such a batch

reactor segment, we can therefore directly follow the consumption of H_2O_2 by the catalyst over time, while simultaneously assessing the BES of the bubble that grows upstream. **Figure 6b** displays corresponding experimental time traces measured for a batch reactor that featured several citrate-covered Pt nanoparticles in the trap and occurred during the same experiment as discussed above (cf. **Figure 4**). Specifically, the figure displays the time evolution of the O_2 production rate derived from the BES (red line) together with the H_2O_2 concentration evolution downstream of the trap (yellow line), as well as during the initial phase of the experiment upstream from it (orange line). The concentration traces exhibit the expected course of rapid initial increase when the H_2O_2 is flushed into the channel. Also as before, the onset of the upstream bubble growth indicated by a measurable BES, occurs when the H_2O_2 reaches its maximum 30 % value and shows the typical initial peak (**cf. Figure 5**).

As the first key difference compared to the experiments above with the "flow reactors", we notice a transient disturbance of the H_2O_2 concentration curve over the course of 5 frames that signals the rapid formation and detachment of the downstream bubble which is terminated when the upstream bubble starts to form. Accordingly, the time trace of the H_2O_2 concentration measured upstream of the bubble is terminated at the onset of the upstream bubble formation (since it cannot be measured anymore due to the brightness of the bubble), which nicely coincides with the detachment of the downstream bubble. As the key observation from here forward, and in distinct contrast to the scenarios discussed above, the H_2O_2 concentration we measure inside the batch reactor does not remain constant at the set level of 30 % but reduces with time to reach almost zero after ca. 18 seconds of reaction. At the same time, the rate of O_2 evolution keeps dropping as the concentration decreases. This is the consequence of the catalyst particle(s) rapidly consuming the H_2O_2 inside the batch reactor and of the limited inflow of reactant along the upstream bubble – channel wall interface not being sufficient to resupply the H_2O_2 consumed by the catalyst. This is a remarkable result because it (i) is the first direct and

label free measurement of reactant conversion from only few nanoparticles in real time at realistic reaction conditions and because it (ii) demonstrates the potential of NSM when used in a batch reactor configuration to enable single particle reactivity measurements for arbitrary reactions at technically relevant reaction conditions, provided that batch reactors can be created in a controlled fashion.

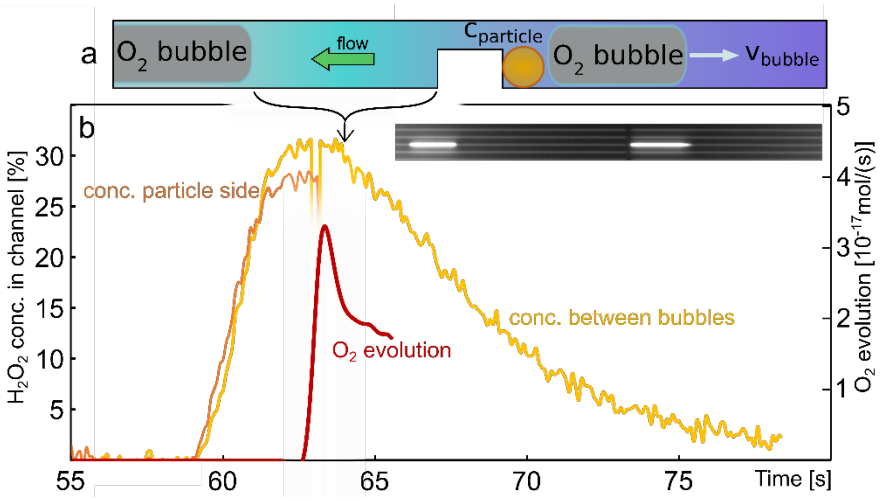

Figure 6. **Spontaneous batch reactor formation.** a) Schematic *depiction of* a *spontaneous* batch reactor form*ing* in the nanochannels, when *a particle is trapped* between two O_2 bubbles. b) *Time evolution of the* H_2O_2 concentration *derived from scattering intensity of* a spontaneous batch reactor *measured between the bubbles (yellow) and upstream of the particle (orange) plotted* together with the O_2 *evolution* rate *(red) derived from the BES of the upstream bubble. Note the transient disturbance of the* H_2O_2 *concentration curve at ca. t = 63 s over the course of 5 frames that signals the rapid formation and detachment of the downstream bubble.*

Conclusions

We have demonstrated the use of nanofluidic scattering microscopy, NSM, to measure concentration changes inside nanofluidic systems based on the methods' high sensitivity to RI changes that are reflected in a reduced light scattering intensity from a nanochannel if the RI difference between liquid and channel wall material is reduced. Applying this concept to the scrutiny of H_2O_2 diffusion into a water filled nanochannel, we have verified the validity of the macroscopic description of molecular diffusion despite significant nanoconfinement imposed by a nanochannel, by extracting a bulk H_2O_2 diffusion coefficient in water that is in excellent agreement with the literature value[33] of $D = 2 \cdot 10^{-9}\, m^2/s$. These results thus advertise NSM for experimental studies of diffusion in nanoconfined systems where molecular interactions with the nanochannel walls become sizable and the dominant contribution to diffusive molecular transport.

As a second key result, we have demonstrated that NSM enables the visualization, tracking and counting of optically dark metal nanoparticles, such as Pt that is highly "lossy" in the visible spectral range due to widely abundant interband transitions. This is a significant step beyond the state of the art since investigations of strongly absorbing metal nanoparticles, as well as plasmonic systems like Au in the sub-50 nm particle size regime, to date are not possible by traditional dark-field scattering microscopy. Hence, NSM has the potential to significantly expand the nanoparticle size and composition range accessible with this type of optical microscopy widely used for single nanoparticle studies.

As the third key result, on the example of H_2O_2 decomposition over Pt, we have introduced NSM as a tool for single particle catalysis that enables *in situ* measurements of absolute reactant concentrations adjacent to an active colloidal catalyst nanoparticle and along the nanochannel that hosts the particle. Therefore, NSM has the potential to resolve concentration gradients

induced by reactant conversion over single nanoparticles and thereby shed light on the interplay between mass transport and surface reaction governed catalyst activity in nanoconfined reaction environments. Furthermore, by simultaneously tracking the rate of O_2 bubble growth in the nanochannel, we have derived single nanoparticle ToFs that exhibited a significant distribution that reflected the wide size distribution of the Pt nanoparticles.

Finally, by comparing single particle ToFs for the H_2O_2 decomposition reaction obtained from citrate and PVP coated structurally identical colloidal Pt nanoparticles trapped in nanochannels, we revealed a distinct reduction of catalytic activity for the PVP coated system, due to PVPs strong interaction with both terrace and edge sites on Pt, and its more pronounced steric hindrance for reactants to reach the catalyst surface.

In a wider perspective, our results advertise NSM as a versatile optical microscopy method that, once fully developed, has the potential to enable single particle reactivity measurements for arbitrary reactions without fluorescent labels or other enhancement mechanisms at technically relevant reaction conditions.

Methods

Instruments: The dark-field nanochannel scattering microscopy (NSM) experiments were carried out on a Zeiss Axio Observer Z1 microscope equipped with a Thorlabs Solis-3C LED light source. A Zeiss 50x dark-field objective together with a dark-field reflector cube was used. The scattered light was recorded with an Andor iXon Ultra 888 EMCCD camera, set to take kinetic series of 1000 pictures each with an exposure time of 0.1 s. The transmission electron microscopy (TEM) images were taken with a FEI Tecnai T20 that was operated at 200 kV and had a LaB6 filament, as well as a Orius CCD camera installed. The SEM imaging of the platinum particles and the open nanochannels was carried out on a Zeiss Supra 60 VP with a secondary in-lens electron detector operated at 15 kV. Working distance was set to 2.5 mm.

Data Evaluation: The images from the camera were recorded using the Andor Solis Software and saved as full-scale tiff-images. A custom LabView program was used to read in the images and separate the channels, which were then evaluated individually. The two main functions of the program are the counting of pixels whose count values surpass a certain threshold (bubble extension) and averaging the scattering from each side of the nanochannel (concentration determination), both of which were recorded as function of time. The bubble-extension-over-time data was smoothed by fitting a cubic spline fit in LabView evaluation program, and a derivative was taken to determine the bubble extension speed. The measurement of the particle diameter was done in ImageJ after calibrating the size of the SEM picture with the provided scale bar.

Reagents and Nanoparticles: All solutions where prepared using ultrapure water (Milli-Q IQ 7000 water purification, Merck). The same water was used when flushing and cleaning the nano/microfluidic system. Hydrogen peroxide was bought from Sigma-Aldrich (H2O2, 35% w/w in H2O). Platinum nanoparticles from nanoComposix (PTCB70-10M, BioPure Platinum

Nanoparticles – Bare (Citrate), 70 nm) were acquired. The ligand exchange was done by first preparing a 100 mM solution of PVP in ultrapure MilliQ water before adding 2 ml of this solution to 2 ml of the nanoparticle solution. The mixture was then stirred gently for 24 h at room temperature to ensure to complete exchange from citrate to PVP ligands.

Fluidic chip fabrication: The nanofluidic systems were fabricated by etching all fluidic structures (nanochannels, microchannels, and vias) into thermally oxidized silicon substrates and bonding thin glass lids to the structured substrates for sealing, as described by Levin et al.[16,1716]. The nanofabrication can be summarized as follows: First 4" (100) silicon wafers were cleaned with Standard Clean 1, 2% HF Dip and Standard Clean 2. The cleaned wafers were wet oxidized at 1050° C to an oxide layer thickness of 2000 nm. Nanochannels were etched into the thermally grown oxide with fluorine-based reactive ion etching (RIE) using a Cr hard mask patterned with e-beam lithography and chlorine-based RIE. To create vertical constrictions within the nanochannels, they were first etched to the nominal constriction depth, then photoresist lines were patterned using laser lithography on the hardmasks across the nanochannels at the constriction positions, and then the nanochannels were etched to their final depth. Subsequently, all microfluidic structures were etched into the surface by RIE using photoresist etch masks, typically patterned by direct laser lithography, and vias were fabricated with deep reactive ion etching. Finally, the substrates were cleaned with Standard Clean 1 along with 175 µm thick 4" Borofloat33 glass wafers, and the surfaces of both the substrates and the glass wafers were plasma treated with O2 plasma (50W, 250mTorr) to allow the glass lids to be pre-bond to the substrates prior to fusion bonding them (550 °C , 5 hours). The bonded wafers were then cut into individual fluidic chips.

Supporting Information

This material is available free of charge via the Internet at http://pubs.acs.org.

Corresponding Author

clangham@chalmers.se

Author Contributions

The manuscript was written through contributions of all authors. All authors have given approval to the final version of the manuscript.

Acknowledgements

This research has received funding from the Swedish Research Council (VR) Consolidator Grant project 2018-00329 and the European Research Council (ERC) under the European Union's Horizon Europe research and innovation programme (101043480/NACAREI). Part of this work was carried out at the Chalmers MC2 cleanroom facility and at the Chalmers Materials Analysis Laboratory.

TOC Figure

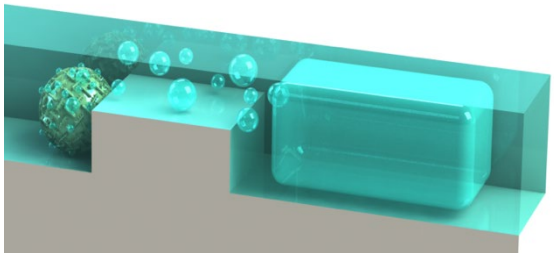

References

1. Sambur, J. B. & Chen, P. Approaches to single-nanoparticle catalysis. *Annu. Rev. Phys. Chem.* **65**, 395–422 (2014).

2. Xu, W., Zhang, Y. & Chen, T. *Single particle nanocatalysis: Fundamentals and applications*. *Single Particle Nanocatalysis: Fundamentals and Applications* (2019). doi:10.1002/9783527809721.

3. Zhou, X., Choudhary, E., Andoy, N. M., Zou, N. & Chen, P. Scalable Parallel Screening of Catalyst Activity at the Single-Particle Level and Subdiffraction Resolution. *ACS Catal.* **3**, 1448–1453 (2013).

4. Hansen, T. W. & Wagner, J. B. Catalysts under Controlled Atmospheres in the Transmission Electron Microscope. *ACS Catal.* **4**, 1673–1685 (2014).

5. Hartman, T., Geitenbeek, R. G., Wondergem, C. S., Van Der Stam, W. & Weckhuysen, B. M. Operando Nanoscale Sensors in Catalysis: All Eyes on Catalyst Particles. *ACS Nano* (2020) doi:10.1021/acsnano.9b09834.

6. Hartman, T., Wondergem, C. S., Kumar, N., van den Berg, A. & Weckhuysen, B. M. Surface- and Tip-Enhanced Raman Spectroscopy in Catalysis. *J. Phys. Chem. Lett.* **7**, 1570–1584 (2016).

7. Wang, W. & Tao, N. Detection, counting, and imaging of single nanoparticles. *Anal. Chem.* **86**, 2–14 (2014).

8. van Schrojenstein Lantman, E. M., Deckert-Gaudig, T., Mank, A. J. G., Deckert, V. & Weckhuysen, B. M. Catalytic processes monitored at the nanoscale with tip-enhanced Raman spectroscopy. *Nat. Nanotechnol.* **7**, 583–586 (2012).

9. Alekseeva, S., Nedrygailov, I. I. & Langhammer, C. Single Particle Plasmonics for Materials Science and Single Particle Catalysis. *ACS Photonics* **6**, 1319–1330 (2019).

10. Chen, P., Xu, W., Zhou, X., Panda, D. & Kalininskiy, A. Single-nanoparticle catalysis at single-turnover resolution. *Chem. Phys. Lett.* **470**, 151–157 (2009).

11. Zhou, X. *et al.* Quantitative super-resolution imaging uncovers reactivity patterns on single nanocatalysts. *Nat. Nanotechnol.* **7**, 237–241 (2012).

12. Albinsson, D. *et al. Operando* detection of single nanoparticle activity dynamics inside a model pore catalyst material. *Sci. Adv.* **6**, eaba7678 (2020).

13. Albinsson, D. *et al.* Copper catalysis at operando conditions—bridging the gap between single nanoparticle probing and catalyst-bed-averaging. *Nat. Commun.* **11**, 4832 (2020).

14. Albinsson, D. *et al.* Shedding Light on CO Oxidation Surface Chemistry on Single Pt Catalyst Nanoparticles Inside a Nanofluidic Model Pore. *ACS Catal.* **11**, 2021–2033 (2021).

15. Swapnasrita, S. *et al.* Unravelling CO oxidation reaction kinetics on single Pd nanoparticles in nanoconfinement using a nanofluidic reactor and DSMC simulations. *Chem. Eng. Sci. X* **9**, 100088 (2021).

16. Levin, S. *et al.* A nanofluidic device for parallel single nanoparticle catalysis in solution. *Nat. Commun.* **10**, (2019).

17. Levin, S. *et al.* Nanofluidic Trapping of Faceted Colloidal Nanocrystals for Parallel Single-Particle Catalysis. *ACS Nano* **16**, 15206–15214 (2022).

18. Solsona, M. *et al.* Microfluidics and catalyst particles. *Lab Chip* **19**, 3575–3601 (2019).

19. Tanimu, A., Jaenicke, S. & Alhooshani, K. Heterogeneous catalysis in continuous flow microreactors: A review of methods and applications. *Chem. Eng. J.* **327**, 792–821 (2017).

20. Shashkova, S. & Leake, M. C. Single-molecule fluorescence microscopy review: shedding new light on old problems. *Biosci. Rep.* **37**, (2017).

21. Taylor, A. B. & Zijlstra, P. Single-Molecule Plasmon Sensing: Current Status and Future Prospects. *ACS Sensors* **2**, 1103–1122 (2017).

22. Špačková, B. *et al.* Label-free nanofluidic scattering microscopy of size and mass of single diffusing molecules and nanoparticles. *Nat. Methods* **19**, 751–758 (2022).

23. Piliarik, M. & Sandoghdar, V. Direct optical sensing of single unlabelled proteins and super-resolution imaging of their binding sites. *Nat. Commun.* **5**, 4495 (2014).

24. Taylor, R. W. & Sandoghdar, V. Interferometric Scattering Microscopy: Seeing Single Nanoparticles and Molecules via Rayleigh Scattering. *Nano Lett.* **19**, 4827–4835 (2019).

25. Hart, A. B. & Ross, R. A. Catalytic Decomposition of Hydrogen Peroxide Vapour by Equimolar Mixed Oxides. *Nature* **193**, 1175–1177 (1962).

26. Bohren, C. F. & Huffman, D. R. Rayleigh-Gans Theory. *Absorpt. Scatt. Light by Small Part.* 158–165 (2007) doi:10.1002/9783527618156.ch6.

27. Malitson, I. H. Interspecimen Comparison of the Refractive Index of Fused Silica. *J. Opt. Soc. Am.* **55**, 1205–1209 (1965).

28. Hale, G. M. & Querry, M. R. Optical Constants of Water in the 200-nm to 200-$µ$m Wavelength Region. *Appl. Opt.* **12**, 555–563 (1973).

29. Giguère, P. A. & Geoffrion, P. REFRACTIVE INDEX OF HYDROGEN PEROXIDE SOLUTIONS. A REVISION. *Can. J. Res.* **27b**, 168–173 (1949).

30. Ahmed, T., Shimizu, T. S. & Stocker, R. Microfluidics for bacterial chemotaxis. *Integr. Biol.* **2**, 604–629 (2010).

31. Karimi, M. Diffusion in Polymer Solids and Solutions. *Mass Transf. Chem. Eng. Process.* (2011) doi:10.5772/23436.

32. Fick, A. Ueber Diffusion. *Ann. Phys.* **170**, 59–86 (1855).

33. Xing, W. *et al. Oxygen Solubility, Diffusion Coefficient, and Solution Viscosity*. *Rotating Electrode Methods and Oxygen Reduction Electrocatalysts* (Elsevier B.V., 2014). doi:10.1016/B978-0-444-63278-4.00001-X.

34. Pappaert, K., Biesemans, J., Clicq, D., Vankrunkelsven, S. & Desmet, G. Measurements of diffusion coefficients in 1-D micro- and nanochannels using shear-driven flows. *Lab Chip* **5**, 1104–1110 (2005).

35. Wang, J., Zhang, L., Xue, J. & Hu, G. Ion diffusion coefficient measurements in nanochannels at various concentrations. *Biomicrofluidics* **8**, 1 (2014).

36. Fanchi, J. R. Chapter 9 - Fluid Flow Equations. in *Shared Earth Modeling* (ed. Fanchi, J. R.) 150–169 (Butterworth-Heinemann, 2002). doi:https://doi.org/10.1016/B978-075067522-2/50009-4.

37. Langhammer, C., Kasemo, B. & Zorić, I. Absorption and scattering of light by Pt, Pd, Ag, and Au nanodisks: Absolute cross sections and branching ratios. *J. Chem. Phys.* **126**, (2007).

38. Serra-Maia, R. *et al.* Mechanism and Kinetics of Hydrogen Peroxide Decomposition on Platinum Nanocatalysts. *ACS Appl. Mater. Interfaces* **10**, 21224–21234 (2018).

39. Olszok, V., Rivas-botero, J., Wollmann, A., Benker, B. & Weber, A. P. Particle-induced nanobubble generation for material-selective nanoparticle fl otation. *Colloids Surfaces A* **592**, 124576 (2020).

40. Bianchi, G., Mazza, F. & Mussini, T. Catalytic decomposition of acid hydrogen peroxide solutions on platinum, iridium, palladium and gold surfaces. *Electrochim. Acta* **7**, 457–473 (1962).

41. Krupski, K., Moors, M., Jóźwik, P., Kobiela, T. & Krupski, A. Structure determination of Au on Pt(111) surface: LEED, STM and DFT study. *Materials (Basel).* **8**, 2935–2952 (2015).

42. Liu, J., Wei, X., Wang, X. & Liu, X. W. High-yield synthesis of ultrathin silica-based nanosheets and their superior catalytic activity in H2O2 decomposition. *Chem. Commun.* **47**, 6135–6137 (2011).

43. Borodko, Y. *et al.* Probing the Interaction of Poly(vinylpyrrolidone) with Platinum Nanocrystals by UV−Raman and FTIR. *J. Phys. Chem. B* **110**, 23052–23059 (2006).

44. Ye, J. Y. *et al.* Explicit Detection of the Mechanism of Platinum Nanoparticle Shape Control by Polyvinylpyrrolidone. *J. Phys. Chem. C* **120**, 7532–7542 (2016).

45. Stolaś, A., Darmadi, I., Nugroho, F. A. A., Moth-Poulsen, K. & Langhammer, C. Impact of Surfactants and Stabilizers on Palladium Nanoparticle–Hydrogen Interaction Kinetics: Implications for Hydrogen Sensors. *ACS Appl. Nano Mater.* **3**, 2647–2653 (2020).

46. Lu, L., Zou, S. & Fang, B. The Critical Impacts of Ligands on Heterogeneous Nanocatalysis: A Review. *ACS Catal.* **11**, 6020–6058 (2021).

Supplementary Material

for

Nanofluidic Scattering Microscopy of Single Colloidal Platinum Nanoparticle H_2O_2 Decomposition Catalysis

Björn Altenburger[1], Carl Andersson[1], Sune Levin[2], Fredrik Westerlund[2], Joachim Fritzsche[1] and Christoph Langhammer[1]*

[1]Department of Physics, Chalmers University of Technology; SE-412 96 Gothenburg, Sweden

[2]Department of Biology and Biological Engineering, Chalmers University of Technology; SE-412 96 Gothenburg, Sweden

*Corresponding author: clangham@chalmers.se

Section I: Supplementary figures

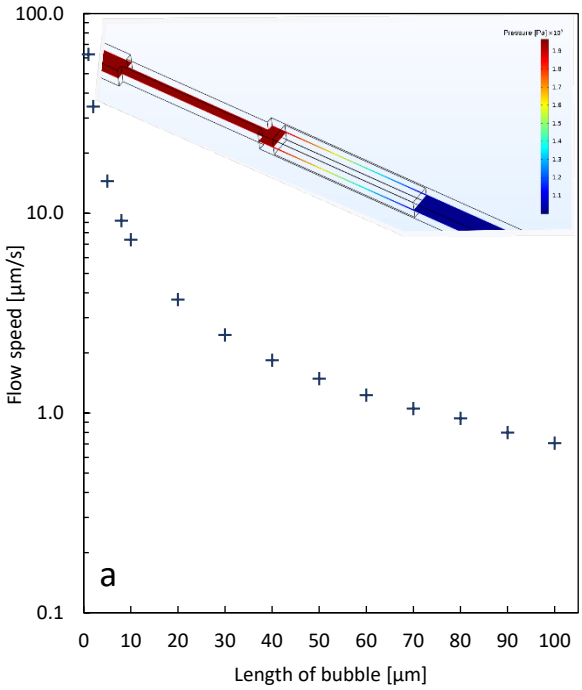

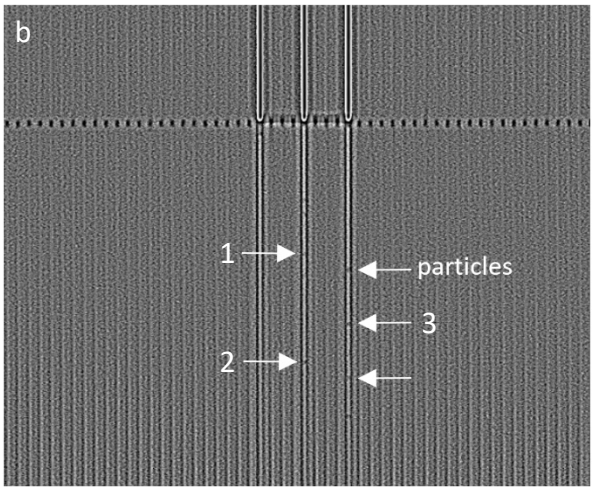

particle	Δt [s]	Δs [µm]	v [µm/s]
1	5	38.24	7.65
2	4	21.00	5.25
3	1.3	10.34	7.95

Figure S2. Flow speed in the nanochannel for 2 bar inlet pressure. a) Simulated liquid flow speed inside a 150 nm x 150 nm nanochannel as a function of the length of a bubble that is growing inside that channel. The maximum length of the bubble is 170 µm (length of the nanochannel after the constriction). The inset shows the Comsol-simulated pressure drop along a bubble of 1 µm length. b) Measurement of the flow speed inside nanochannels via tracking the movement of Pt nanoparticles (arrows) induced by the flow. The differential dark-field image shows how particles can be seen moving out of the channels when the pressure at the inlets of the chip is inverted. The three channels that stand out are filled with a bubble on the other side of the trap. Tracking several particles while the same pressure is applied as during bubble formation allows an estimation of the flow speed when a bubble is filling the channels. The table lists the results for three particles.

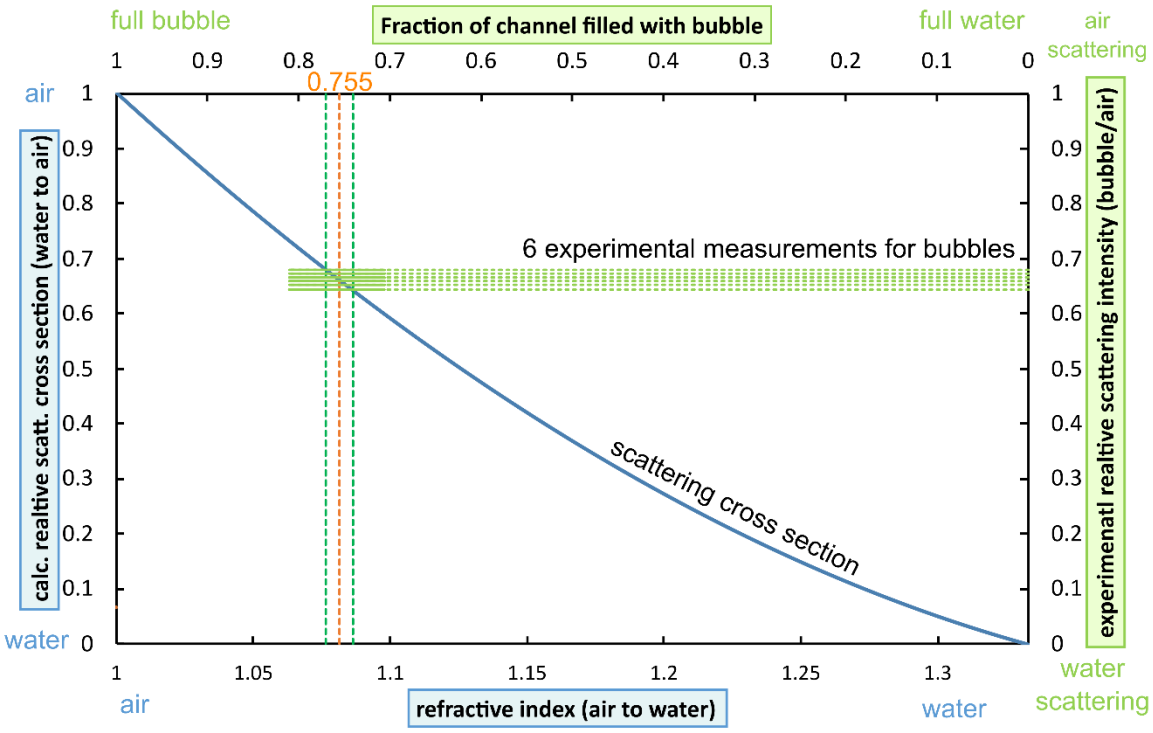

Figure S3. Scheme to estimate the fraction of the nanochannel that is filled with gas when a bubble is filling the channel. Blue axis: Calculated relative scattering in dependence of the refractive index (blue curve). The scattering of a completely gas filled channel has been set to 1, for a completely water filled channel it is set to 0. Green axis: Experimental scattering intensities, where the scattering from a water-filled channel has been set to zero and the scattering from a air-filled channel set to 1. The horizontal green lines represents the scattering measured from 6 bubble-filled channels relative to the scattering of the same channels filled with air. Translating the experimental scattering ratio via the curve for the scattering cross section leads to the estimation that the gas bubble fills the channels to around 75.5%.

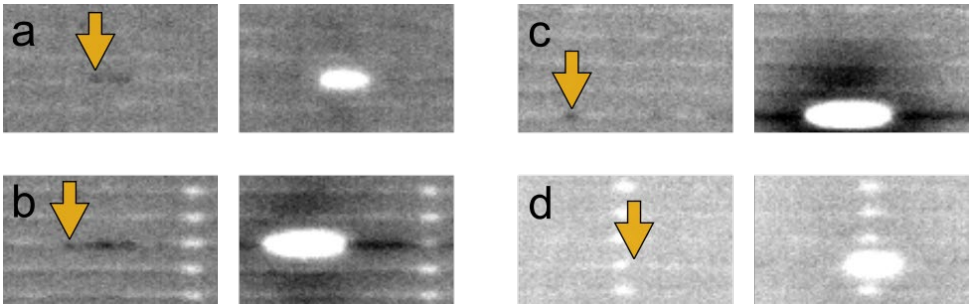

Figure S4. Detection of PVP particles. The darkfield images here were FFT filtered to remove the regular pattern of the nanochannels and to reveal the particles. The particles initializing the bubbles are marked with arrows. In a and b, many particles leave position as H_2O_2 is flowing in (dark spots to the right side of the arrows). In c and d, we assume that only a single particle remains. This assumption was corroborated by the bubble extension speeds.

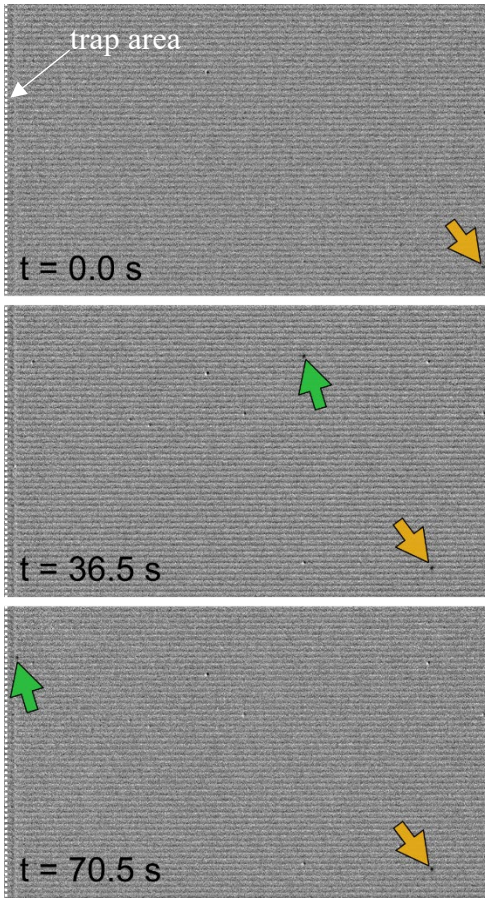

Figure S5. Citrate coated Pt particles getting stuck in nanochannels before the trap. The particle marked with orange arrow enters the field of view at t = 0s as it is pushed through the channel but gets stuck due to electrostatic interaction with the wall at t = 36.5 s and remains in the same position at t = 70. 5 s. The particle marked with a green arrow gets transiently stuck at 36.5 s before eventually reaching the trap at 70.5 s.

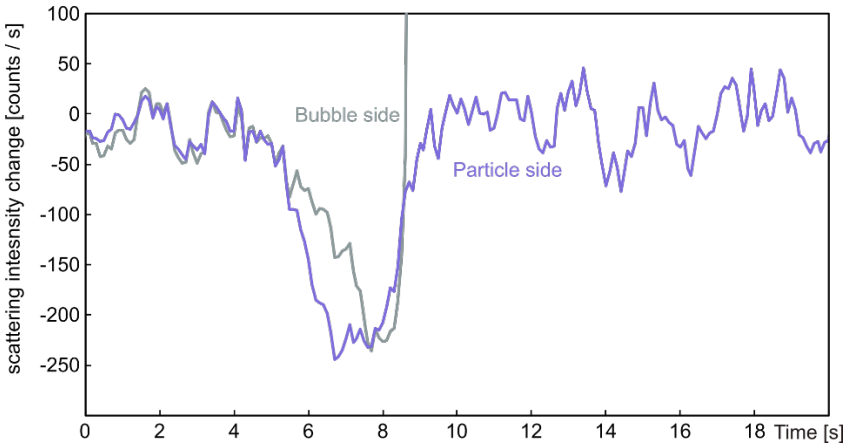

Figure S6. Derivative of the channel scattering intensity traces shown in Figure 5a in the main text. The peak of the derivative is shifted by about 1 s between the two channel sections and thus indicates a time delay of about 1 seconds for the H_2O_2 front reaching these two channel sections.

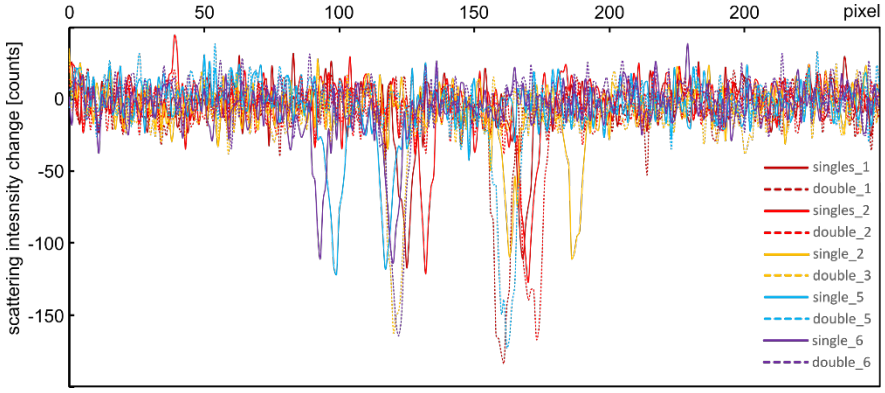

Figure S7. Nanochannel scattering intensities for channels containing two particles that meet in a diffraction limited spot during their movement. *The curves show the scattering for separated and combined particles for each channel. When together, the scattering at the particle spot decreases by about 40% compared to the single particles.*

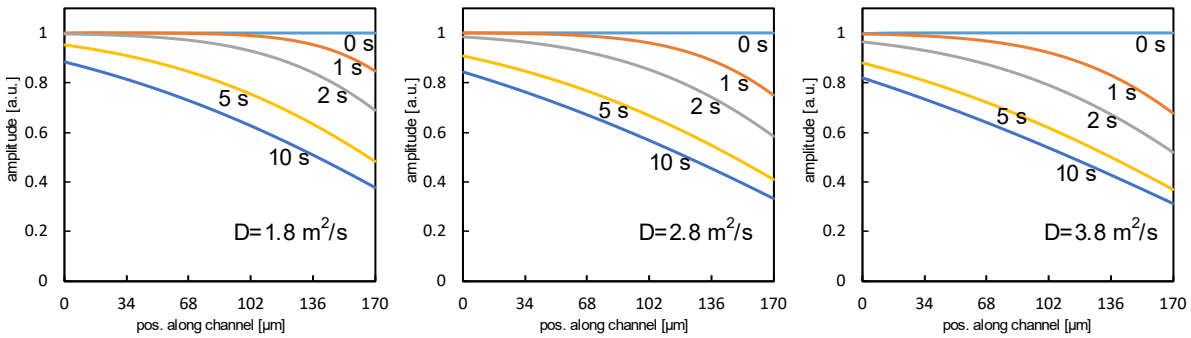

Figure S8. *Calculated* time evolution of H_2O_2 *concentration p*rofiles in a nanochannels for bulk diffusion constants D = 1.8 m^2/s, D = 2.8 m^2/s and D = 3.8 m^2/s.

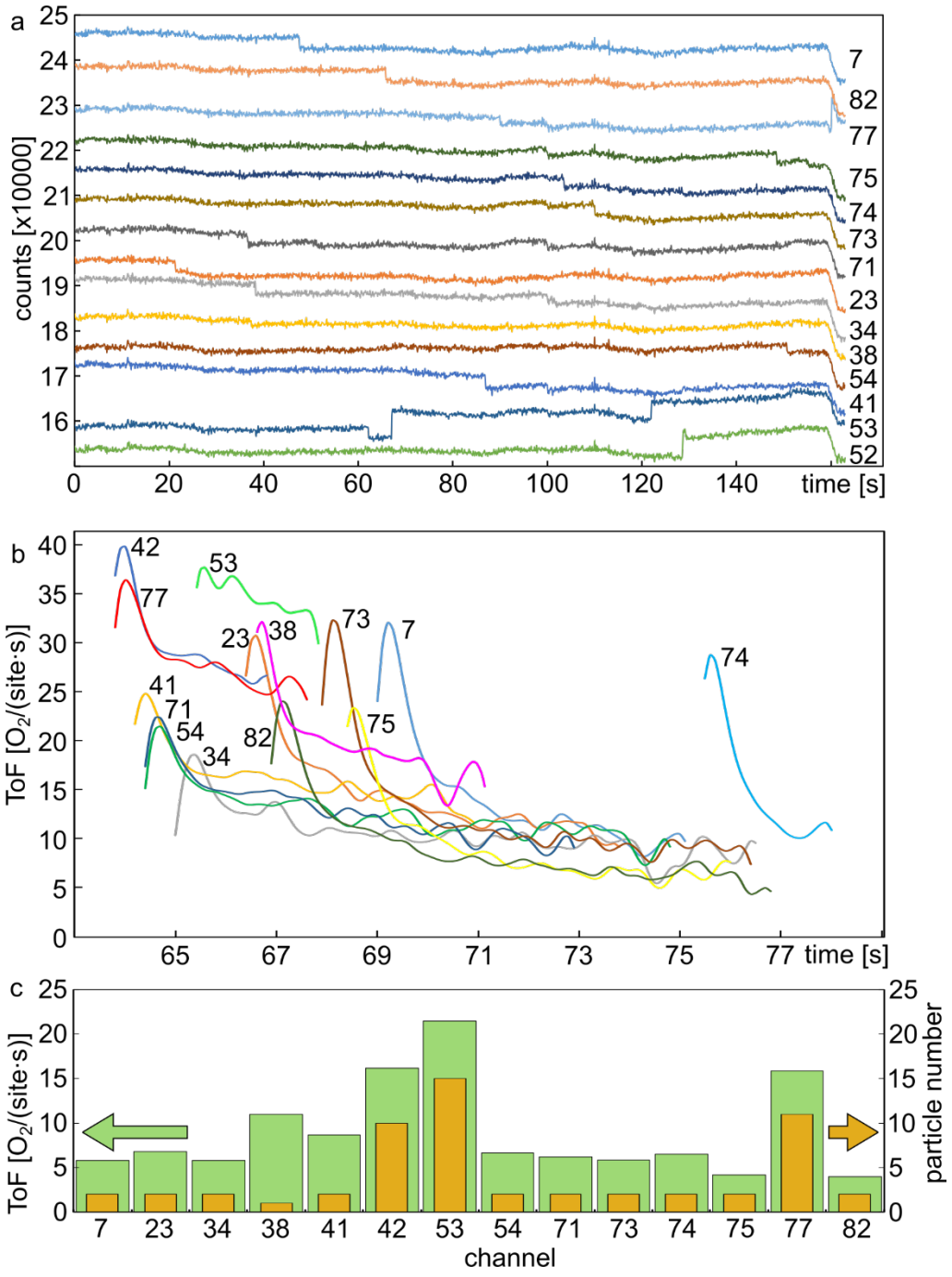

Figure S9. Pt particle counting. a) Integrated scattering intensity of the trap area for the measurement shown in **Figure 4** in the main text for all channels that show bubble formation according to Scenario I. The arrival of particles can be seen as steps in the intensity. When many many particles accumulate, the scattering from the trap becomes higher than the reference (channels 42, 53 and 77). b) ToF traces for the channels shown in a) for a H_2O_2 concentration of 30%. c) Comparison of the counted (for large numbers estimated) particle number and final ToF.

Section II: Supplementary Derivations

1. Theoretical calculation of nanochannel scattering cross sections

The derivation of the scattering cross section formula for a nanochannel, Equation 1 in the main text, is described in detail in chapter 8 of the book by Bohren and Huffman[26]. For convenience, I summarize the key steps below.

To mathematically describe the rectangular channels from the experiment, we use a cylinder of infinite length, whose diameter corresponds to the cross section of the experimental nanochannel. Accordingly, the derivation uses cylindrical coordinates as given in **Fiure S** .

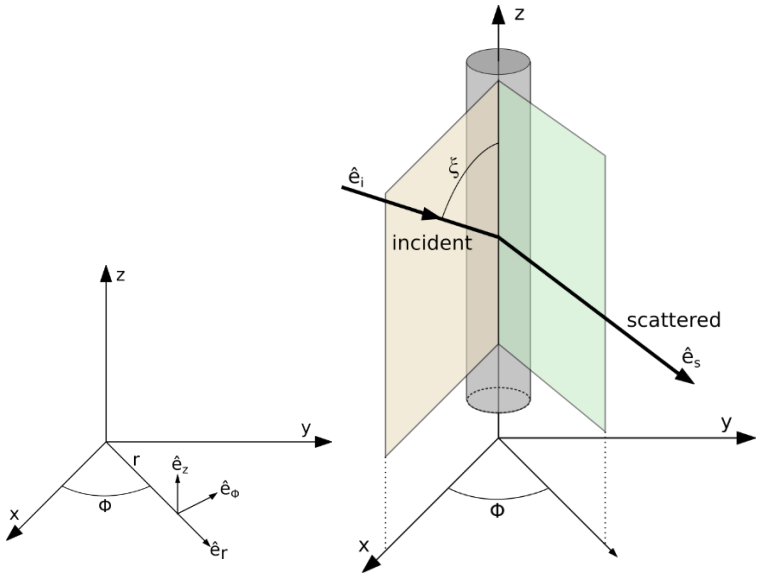

Figure S 11. Cylindric coordinate system and a section of the infinite cylinder with the Poynting vector of the incident and scattered light.

The function that solves the wave equation in cylindrical coordinates can be written in a form that separates into a radial, angular and vertical part, where $h = -k\cos\zeta$ is the separation constant and $\rho = r\sqrt{k^2 - h^2}$ with k as wavenumber.

$$\psi_n(r, \phi, z) = Z_n(\rho)e^{in\phi}e^{ihz} \quad (n = 0, \pm 1, \dots)$$

Linearly independent solutions to Z_n are the Bessel functions of the first and second kind, J_n and Y_n respectively, where n denotes their integral order. The harmonic functions generated from the equation above,

$$M_n = \nabla \times (\hat{e}_z \psi_n), \qquad N_n = \frac{\nabla \times M_n}{k}$$

will be used to express the incident electric field of a plane wave $E_i = E_0 e^{ik\hat{e}_i x}$ that is incident onto a cylinder of radius a in the direction of $\hat{e}_i = -\sin\zeta \hat{e}_x - \cos\zeta \hat{e}_z$ with ζ being the angle between cylinder axis and the incident wave. For an incident electric wave that is parallel to the xz-plane, the expansion in cylinder harmonics is

$$E_i = \sum_{n=-\infty}^{\infty} [A_n M_n^I + B_n N_n^I].$$

The generating function for the cylinder harmonics in then $J_n(kr\sin\zeta)e^{in\phi}e^{-ikz\cos\zeta}$, as we need to exclude the Bessel functions of the second kind to avoid an infinite electric field at $r = 0$. Following Bohren and Huffman, the coefficients are given as

$$A_n = 0, \qquad B_n = \frac{E_0(-i)^n}{k\ \sin\zeta}$$

such that for the incident wave, when $E_n = E_0\ (-i)^n/k\sin\zeta$,

$$E_i = \sum_{n=-\infty}^{\infty} E_n N_n^I, \qquad H_i = \frac{-ik}{\omega\mu} \sum_{n=-\infty}^{\infty} E_n M_n^I$$

For the internal field, we define first the ration of refractive indexes

$$m = \frac{n_{cylinder}}{n_{surrounding}}.$$

to arrive at

$$E_I = \sum_{n=-\infty}^{\infty} E_n [g_n M_n^I + f_n N_n^I], \qquad H_I = \frac{-ik}{\omega\mu} \sum_{n=-\infty}^{\infty} E_n [g_n N_n^I + f_n M_n^I]$$

For the scattered field, we find

$$E_s = \sum_{n=-\infty}^{\infty} E_n [b_{n1} N_n^3 + i a_{n1} M_n^3], \qquad H_s = \frac{ik}{\omega\mu} \sum_{n=-\infty}^{\infty} E_n [b_{n1} M_n^3 + i f a_{n1} N_n^3]$$

Such that we now can describe the Poynting vector

$$S_s = \frac{1}{2}\,\mathrm{Re}(\boldsymbol{E}_s \times \boldsymbol{H}_s^*) \quad S_s = \frac{1}{2}\,\mathrm{Re}(\boldsymbol{E}_i \times \boldsymbol{H}_s^* + \boldsymbol{E}_s \times \boldsymbol{H})_i^*$$

and the absorption, scattering and extinction rates for the incoming light.

$$W_a = -\int_A \boldsymbol{S} \cdot \hat{\boldsymbol{n}}\ dA = W_{ext} - W_s = RL \int_0^{2\pi} (\boldsymbol{S}_{ext})_r\ d\phi - RL \int_0^{2\pi} (\boldsymbol{S}_s)_r\ d\phi$$

Comparing these rates with the projected cross section of the channel, we arrive at the scattering efficiency (for parallel incident light).

$$Q_{sca,p} = \frac{W_s}{2aLI_i} = \frac{2}{x}\left[|b_0|^2 + 2\sum_{n=1}^{\infty}(|b_n|^2 + |a_n|^2)\right]$$

The coefficients a_n and b_n can be found Bohren and Huffman[26], and we arrive at the scattering efficiencies for both parallel, and, in similar manner, orthogonally polarized incident light.

$$Q_{sca,p} = \frac{\pi^2 x^3}{8}(m^2-1)^2 = \frac{\pi^2 k^3 a^3}{8}(m^2-1)^2$$

$$Q_{sca,o} = \frac{\pi^2 x^3}{4}\left(\frac{m^2-1}{m^2+1}\right)^2 = \frac{\pi^2 k^3 a^3}{4}\left(\frac{m^2-1}{m^2+1}\right)^2$$

From those, we use $x = ka = 2\pi a/\lambda$ and as geometrical cross section $A_\emptyset = \pi a^2$ to arrive at the scattering cross sections for both polarization directions of incident light, as well as for unpolarized light, which corresponds to Equation 1 in the main text.

$$\sigma_{sca,p} = \frac{A_\emptyset^2 k^3 L}{4}(m^2-1)^2$$

$$\sigma_{sca,o} = \frac{A_\emptyset^2 k^3 L}{2}\left(\frac{m^2-1}{m^2+1}\right)^2$$

$$\sigma_{sca,u} = \frac{A_\emptyset^2 k^3 L}{4}(m^2-1)^2\left(\frac{1}{2} + \frac{1}{(m^2+1)^2}\right)$$

2. Influence of oxygen solubility

For the estimation of the influence of the O_2 solubility in water on the bubble formation in a nanochannel, we start at an average BES of 6.3 µm/s, which can be translated into an O_2 production rate of $2.5 \cdot 10^6\ O_2/s$ per particle when using Equation 3 in the main text.

From Figure 2d, we can estimate the flow speed of the liquid in the channel at an inlet pressure of 2 bar to be 40 µm/s. Multiplied with the channel cross section of 150 x 150 nm^2, we arrive at a volume flow of $7.84 \cdot 10^{-19}\, m^3/s$. Using now the solubility of 1.22 mol/m^3 and Avogadros constant, we see that about $0.6 \cdot 10^6\ O_2/s$ could be transported away by the flow in the channel, which is about a quarter of the above estimated O_2 production rate.

This will however be only the case at the very start of the reaction, because as soon as a bubble has formed, the flow speed will be drastically decreased (see also **Figure S2a**), thereby limiting the transport of dissolved oxygen and thus significantly reducing this effect.

3. Turnover frequency from bubble expansion speed

At the start, we need to derive the amount of O_2 produced per second. To do this, we assume that the bubble is rectangular as the channel and has a cross section that is the geometrical cross section of the channel times the filling factor determined in **Figure S3**.

$$A_{bub} = 0.755 A_{channel}$$

Multiplied by the BES, which has the unit of m/s, we arrive at the bubble volume expansion speed in m^3/s. Divided by the volume of 1 mol of O_2 gas, $V_{O2}^{mol} = 22.4\ l/mol$, we get the number of moles of molecular oxygen produced within 1 s.

$$R_{o2} = \frac{A_{bub}\ BES}{V_{O2}^{mol}}$$

Multiplying this with Avogadro's number, we get the absolute amount of O_2 molecules produced per second. Divided by the number of active sites N, we get the number of O_2 molecules produced per site and second, which corresponds to the turnover frequency.

$$ToF = \frac{0.755\ A_{channel}\ BES\ N_A}{V_{O2}^{mol} N}$$